Adsorption and Charge Transfer Dynamics of Photovoltaic and Photocatalytic Dye-Sensitizers

Matthew Weston, MSci. (Hons)

Thesis submitted to The University of Nottingham
for the degree of Doctor of Philosophy

July 2014

Abstract

In this thesis photovoltaic and photocatalytic water-splitting dye complexes have been studied adsorbed onto the rutile TiO_2(110) surface. The photovoltaic dye-sensitizer N3 (cis-bis(isothiocyanato)bis(2,2′-bipyridyl-4,4′-dicarboxylato)-ruthenium(II)) was studied along with Ru 455 (cis-bis(2,2′-bipyridyl)-(2,2′-bipyridyl-4,4′-dicarboxylic acid) ruthenium(II)) and Ru 470 (tris(2,2′-bipyridyl-4,4′-dicarboxylic acid) ruthenium(II)) which have very similar chemical structures. Dipyrrin-based dye complexes PY1 (bis(5-(4-carboxyphenyl)-4,6-dipyrrin)bis(dimethylsulfoxide)Ruthenium(II)) and PY2 (bis(5-(4-carboxyphenyl)-4,6-dipyrrin)(2,2′-bipyridine)Ruthenium(II)) were also studied which should have different bonding geometries on the TiO_2 surface. A single centre water-splitting dye complex (aqua(2,2′-bipyridyl-4,4′-dicarboxylic acid)-(2,2′:6′,6″-terpyridine) Ruthenium(II)) was studied along with a chloride containing analog ((2,2′-bipyridyl-4,4′-dicarboxylic acid)-(2,2′:6′,6″-terpyridine)chloride Ruthenium(II)). The molecules studied here would have been damaged using traditional UHV deposition techniques so electrospray deposition was used to deposit intact molecules *in situ* for experiments in UHV.

Adsorption geometries of the molecules on the TiO_2 surface were investigated using experimental photoemission data supported by density functional theory (DFT) calculations. Dipyrrin-based dye complexes were found to bond with both available carboxylic acid groups to the TiO_2 surface. Also the results suggest that Ru 470 is most likely to bond to the TiO_2 surface with a different bonding geometry to other bipyridine-based complexes with very similar chemical structures.

The molecular orbitals of the dye complexes were investigated using near-edge x-ray absorption fine structure spectroscopy (NEXAFS). DFT calculations provided possible spatial distributions of the molecular orbitals involved in charge transfer. Energetic alignments were performed using data from visible light spectroscopy to compare energetics for core and valence-hole excitation.

The core-hole clock implementation of resonant photoemission spectroscopy was used

to measure upper limits on the timescale of charge transfer from the excited adsorbate molecules to the TiO_2 surface. The results show charge transfer timescales mostly within the low-femtosecond timescale. The Ru 470 complex was found to be relatively slow at charge transfer possibly due to the different bonding geometry it appears to adopt on the TiO_2 surface.

Acknowledgments

I would like to thank Dr James O'Shea for the countless hours of support and encouragement that he has given me throughout the course of my PhD. Thanks to my fellow PhD students Andrew Britton and Karsten Handrup who made working very long shifts at a synchrotron actually bearable. Thanks also to Tom Reade our long-suffering chemist who often had to patiently explain why the rules of chemistry wouldn't allow us to make a particular chemical we wanted, he worked incredibly hard to make sure we got the chemicals we needed before our synchrotron visits.

Thanks also go to the beamline managers at Max-lab Alexei Preobrajenski, Karina Schulte, Annette Pietzsch and Achim Schnadt, who helped us out making sure that the equipment on their beamlines always worked in spite of the previous beam users. They were always very helpful and tried to make sure we always came away with as much usable data as possible. There are also supervisors at Nottingham who have always provided useful insights into their work and given me fresh perspectives on my own. Thanks to Prof. Peter Beton, Prof. Philip Moriarty, Prof Neil Champness, Dr. James Sharp and Dr. Ioan Notingher.

There was a fantastic support network in the Nottingham nanoscience department. It was great to hang out with them at conferences and to discuss our problems or just to make random small talk in the offices. So thanks to Andrew Pollard, Alex Saywell, Samuel Jarvis, James Bailey, Jason Garfitt, Kevin Langley, Mike Smith, James Russell, Andrew Stannard, Lucy Goff, Adam Sweetman, Peter Sharp, Subhashis Gangopadhyay, Marta Larraona Puy, Claire Sweetenham, Julian Stirling and Faris Sinjab.

I am also incredibly fortunate to have some fantastic friends who have constantly been there for me through the twin stresses of synchrotron visits and life in general. So thank you to Glyn Spencer, Darren Albutt, Katharine Bowker, Josef Granwehr, Alex Cousins, Len and Alan Parker, Burton Yan, Nigel Tate, Simon Bristow, Sarah and Colin Barker, Tom Stevens and Alex Roche. Finally I would like to thank my entire family and especially my parents for their constant love and support throughout my life.

Contents

CHAPTER 1

Introduction to dye-sensitized solar cells

1.1 Introduction

Energy consumption has increased dramatically in modern times, due to both the increase in human population and the increase in energy usage per capita.[1] Fossil fuels have been predominantly used to satisfy the massive demand for energy as they contain large amounts of chemical energy which can be released by simply burning the fuel. Unfortunately, the combustion of fossil fuels releases various chemicals into the atmosphere including carbon dioxide and other greenhouse gases, these chemicals absorb infra-red radiation emitted from the earth leading to an increase in the surface temperature of the planet.[2] If the concentration of greenhouse gases in the atmosphere continues to rise then there will be potentially severe changes to the environment on earth.[3]

Various projects have been proposed which could reduce the concentration or the impact of greenhouse gases in the atmosphere. There are techniques such as carbon capture and storage which removes carbon dioxide from the exhaust gases of power plants where the gas is more concentrated. Geoengineering projects have also been discussed such as fertilising the ocean with iron to encourage the development of phytoplankton which absorb carbon dioxide as they grow, once the plankton die they sink to the bottom of the ocean preventing the carbon dioxide from being released back into the atmosphere. Other projects such as injecting sulphur aerosols into the atmosphere or deploying mirrors in space have been suggested which would reduce the amount of energy reaching the earth's surface from the sun. However, large scale geoengineering projects are likely to face significant technical obstacles, have potentially serious conse-

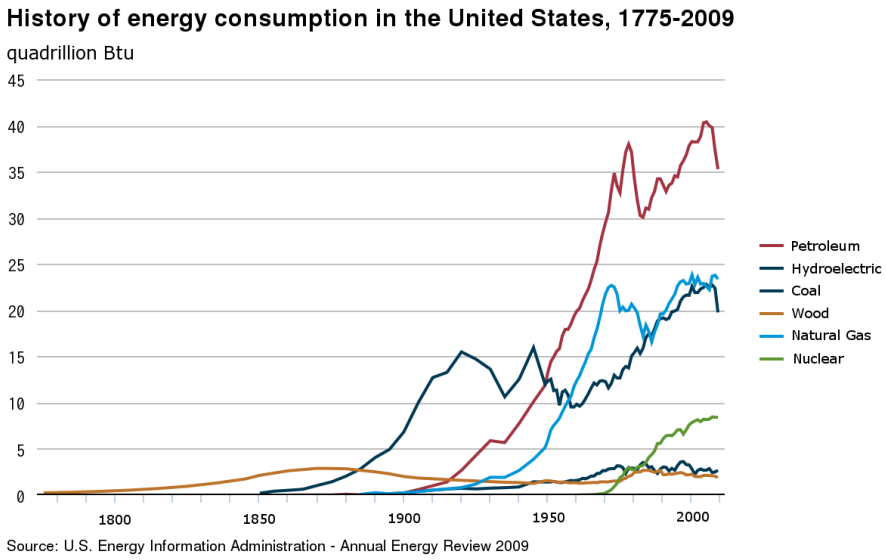

Figure 1.1: Graph showing historical energy production by fuel. Graph adapated from reference [1]

quences and will need a major level of international cooperation to achieve significant results.

Even if geoengineering or other projects are successful in lowering the environmental impact of burning fossil fuels, an alternative energy source will be required in the future as fossil fuels are a finite resource and prices are rising. Transportation is one of the key uses for fossil fuels due to the high energy density of the fuels, giving vehicles a large range with relatively little additional weight. Vehicles using batteries to power electric motors currently have a poor range due to the low energy density of the batteries, although future advances in battery technology may lead to these vehicles becoming more effective. The energy to charge the electric batteries will ideally need to come from a renewable or low-carbon source. Another option is to use hydrogen as a fuel as it has a relatively high energy density by weight, once a suitable storage medium has been found hydrogen could prove to be an efficient fuel.

Producing hydrogen fuel commonly relies on an external source of energy. If this energy is not produced from a renewable source then many of the environmental problems associated with burning fossil fuels will also apply to the production of hydrogen. A renewable external energy source could be used such as hydroelectric power. Although using separate systems associated with generating the energy and producing the hydrogen fuel could lead to energy loss when transferring energy between systems. Therefore a single system which can harvest its own energy and use it to produce hydrogen could prove to be more efficient.

This work is intended to give insights into hydrogen production using modifications to existing photovoltaic dye-sensitized solar cell (DSC) architecture, focusing in particular on the properties of different dye sensitizers. To do this experimental work has been performed on a variety of photovoltaic and photocatalytic dye complexes to help understand the underlying factors that affect the efficiency of DSCs.

In this chapter the basic theories behind dye-sensitized solar cells are explained to show how they work and what is needed to produce an efficient DSC. Chapter 2 describes how a synchrotron produces radiation that can be used to perform experiments on sample dye complexes. In chapters 3 and 4 the experimental and theoretical techniques used to study the dye complexes are described. These techniques allow us to calculate the bonding geometries of the molecules on the surface, the energy and spatial distribution of molecular orbitals important to the charge transfer process and to investigate charge transfer from the adsorbed molecules to the substrate. Chapter 5 explains the underlying principles behind electrospray deposition which is the technique used to deposit the fragile dye complexes onto a surface held under vacuum. Chapter 6 presents the experimental results for three dye complexes with bipyridine-based ligands adsorbed on TiO_2. Chapter 7 contains experimental results for two dye complexes with dipyrrin-based ligands adsorbed onto TiO_2. Chapter 8 has experimental results for a single-centre water-splitting dye complex adsorbed onto TiO_2.

1.2 Photovoltaic dye-sensitized solar cells

Solar energy currently contributes relatively little to global production of electricity. At the moment this is due to the higher cost of producing electricity from conventional silicon-based solar cells as high-grade silicon is relatively expensive.[4] Therefore research is being conducted into both improving the efficiency of these traditional solar cells and developing new types of solar cells which use cheaper materials.

Dye-sensitized solar cells (DSCs) have recently been developed which use a semiconductor as a substrate. Using a semiconductor with a wide band-gap helps to prevent photodegradation as it is more stable than the silicon used in traditional solar cells.[5] Titanium dioxide (TiO_2) is one of the more commonly used semiconductors in DSCs as it is relatively cheap and has a wide band gap. Dye molecules are adsorbed onto the surface of the semiconductor allowing the system to absorb photons of visible light. The dye molecules chemically bond with the surface of the semiconductor which keeps the molecules in close contact with the substrate and aids the transfer of electrons from the dye molecules to the substrate. Many of the experiments in this work are aimed at

studying the interactions between the adsorbed dye and the semiconductor substrate.

1.2.1 The Grätzel cell

One of the most efficient types of DSC uses TiO_2 nanoparticles as a substrate with an adsorbed layer of the molecule N3.[6] This is known as a Grätzel cell. Figure 1.2 is a schematic diagram of a Grätzel cell showing the steps involved in a typical photovoltaic cycle. The bottom section of the figure shows the architecture of the cell and the top section is a close up view of a dye molecule attached to the titanium dioxide semiconductor. The various steps involved are:

1. Incident visible light passes through the transparent conductive support and a photon is absorbed by the dye molecule.
2. The photon's energy is used to promote an electron from an occupied valence orbital to an unoccupied level. The molecule is now in its excited state.
3. If the excited electron's orbital overlaps energetically with the semiconductor conduction band the electron can potentially transfer into the substrate.
4. The electron will then pass through a network of TiO_2 nanoparticles until it reaches the anode of the circuit.
5. The electron travels through the circuit and its energy can be used to power an electrical item.
6. When it reaches the cathode the electron reduces the electrolyte solution, in this case three iodide ions form a triiodide molecule upon reduction.
7. The reduced electrolyte molecule can then be oxidised to replace the lost electron in the dye molecule. This allows for subsequent electron transfer cycles using this molecule.

1.2.2 Dye

One major advantage of DSC cells is that the properties of the sensitizing dye complex can be tuned to match the requirements of the solar cell device. The dye molecules should absorb as much light as possible in the visible region of the electromagnetic spectrum, this is the most intense region of the spectrum that passes through the Earth's

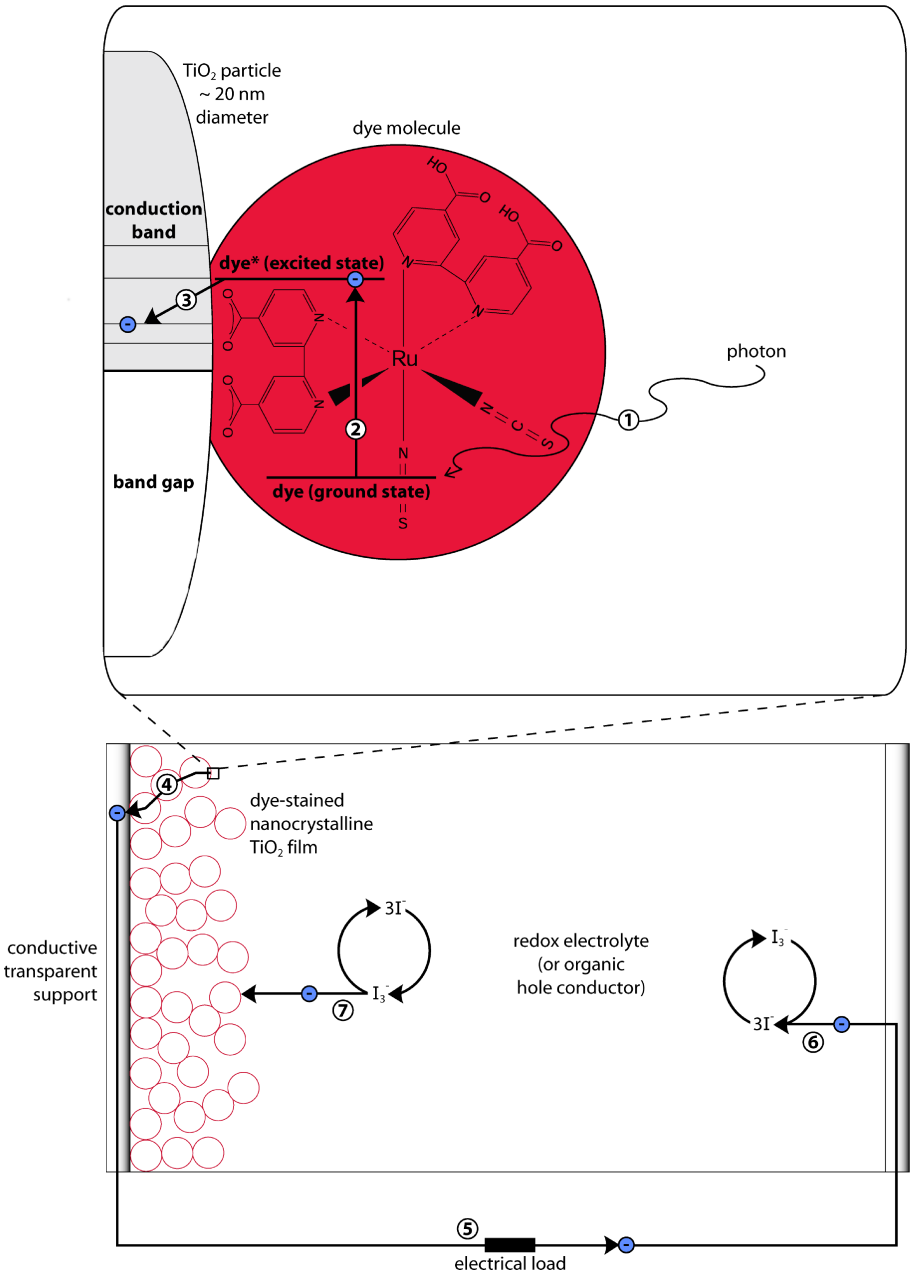

Figure 1.2: Diagram of the Grätzel cell structure showing the steps involved in absorbing a photon of light, electron transfer to the semiconductor and replacing the transferred electron from the electrolyte. These steps are described in the main text. Light enters the cell from the left through the transparent conductive support, in the top section of the diagram the light appears from the right so that it does not overlap with other elements of the diagram.

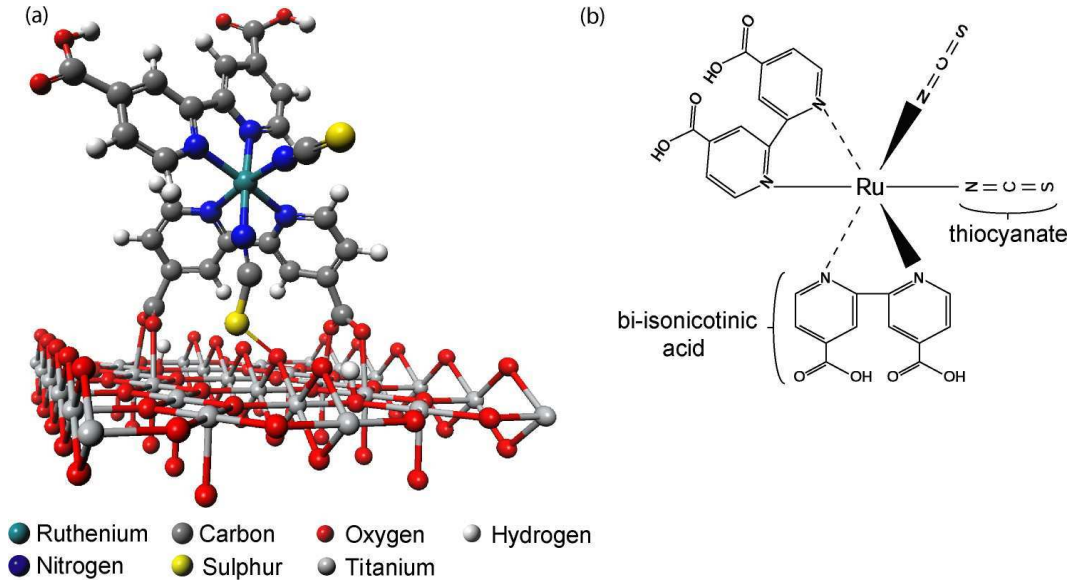

Figure 1.3: a) is a DFT optimised geometry of an N3 molecule attached to rutile TiO_2(110) and b) is the chemical structure of N3 with its ligands labeled. Figure adapted from Reference [7]

atmosphere and reaches the surface. The dye molecules should also cover a small proportion of the surface so that a larger number of molecules can adsorb directly onto the surface. The dye will also need to be stable enough to withstand repeated cycles during operation in a DSC device.

The excited states of the molecule must also overlap energetically with the conduction band of the substrate to allow excited electrons to transfer into the substrate. To increase the chances of charge transfer the lowest unoccupied molecular orbital (LUMO) of the molecule should be located close to the electron injection site and there should be a strong chemical coupling to the surface. The faster the dye molecule can transfer the excited electron to the substrate the more stable the molecule will be in a working DSC device, this is because excited electrons can potentially cause damage to the molecule. This means that the most efficient dye sensitizers are also likely to be more stable leading to longer effective lifetimes for the DSC device. The highest occupied molecular orbital (HOMO) of the dye molecule is best situated on the part of the dye molecule that is furthest away from the semiconductor surface, where it is easily accessible by the electrolyte solution so that electrons lost through charge transfer can be replenished.

The N3 dye complex (also known as Ru 535) is currently one of the most popular dye sensitizers used in DSCs due to its high efficiency, it was first discovered in 1993 by Nazeeruddin and co-workers.[8] The full chemical name of the N3 dye complex is (cis-bis(isothiocyanato)bis(2,2′-bipyridyl-4,4′-dicarboxylato)-ruthenium(II). N3 is a metal-

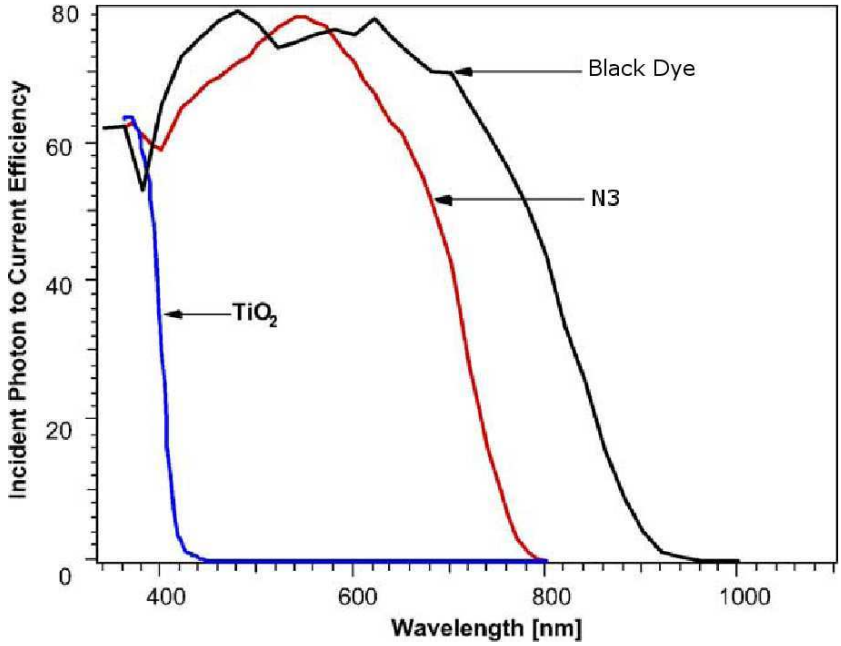

Figure 1.4: Diagram showing incident-photon-to-current efficiency against wavelength of incident photons for unsensitized TiO_2, N3 sensitized TiO_2 and Black dye-sensitized TiO_2. Figure adapted from Reference [9]

ligand complex comprised of a ruthenium metal centre with metal-ligand bonding to two bidentate ligands (2,2'-bipyridyl-4,4'-dicarboxylic acid, more commonly known as bi-isonicotinic acid) and two monodentate isothiocyanate ligands. The chemical structure of N3 and its adsorption geometry on the rutile TiO_2(110) surface can be seen in figure 1.3

A Grätzel DSC using N3 as the sensitizing dye and TiO_2 as the semiconductor can be used to produce a DSC with a cell efficiency of over 11%. This high efficiency has lead to a lot of interest in the dye itself and its interactions with the TiO_2 substrate. Figure 1.4 shows absorption curves for both clean TiO_2 and TiO_2 with adsorbed N3 molecules, the N3 sensitized surface shows a far broader absorption curve extending for most of the visible spectrum. The N3 molecule is also relatively small, chemically stable and the molecule has a relatively high absorption coefficient which are very useful properties for a DSC sensitizer.

The electronic energy levels of N3 are a good match to the TiO_2 substrate, the unoccupied levels of N3 are within the energetic boundaries of the TiO_2 conduction band making it possible for charge transfer of excited electrons from the N3 molecule. The N3 LUMO is located very close to the dye-semiconductor bonding site which provides spatial overlap with orbitals in the semiconductor helping the charge transfer process. The HOMO of the N3 molecule is located on the isothiocyanate ligands, these are exposed

to the electrolyte which allows for efficient replenishment of electrons after successful electron injection into the substrate. The combination of all of these characteristics in one molecule makes N3 a very popular and effective choice for DSC applications.

Another dye sensitizer described as the black dye was developed in 2001, its chemical name is triisothiocyanato-(2,2':6',6"-terpyridyl-4,4',4"tricarboxylato)ruthenium(II). As shown in Figure 1.4 the black dye has a greater absorption range than N3 extending further into the infrared range of the spectrum. The black dye can be used to produce a solar cell with an energy conversion efficiency (ECE) of 10.4% which is higher than the N3 ECE of 9%.[9, 10] By using a coadsorbent called guanidinium thiocyanate with N3 it is possible to create DSC devices with an ECE of over 11%. The coadsorbent works by facilitating self-assembly of the dye molecules on the surface.[9]

1.2.3 Semiconductor

In a DSC device the dye molecules are adsorbed onto the surface of a semiconductor. The interaction between the semiconductor and dye molecules can seriously affect the efficiency of the charge transfer process. The structure of the semiconductor is therefore an important consideration in DSC devices. On a flat semiconductor surface a monolayer of dye molecules absorbs only a few percent of incident visible light.[4] The optical absorption cross-section of each molecule is several orders of magnitude lower than the area that each molecule takes up on the semiconductor surface.[11] Also not all of these absorbed photons give rise to charge carriers. The ratio of incident photons absorbed to charge carriers produced is known as the quantum efficiency. Flat semiconductor DSC devices have low quantum efficiencies of $\leqslant 0.1\%$.[12] In 1976 Matsumura and Tsubomura worked out how to improve the quantum efficiency to 1% using a zinc oxide electrode made from sintered ZnO nanopowder.[12, 13] Sintering the nanocrystalline powder involves applying heat and pressure to the particles which causes them to join together into a solid mass, the temperature should be kept below the melting point of the material during sintering in order to maintain spacing between the particles. The material produced after sintering is mesoporous meaning that liquids can travel into the structure.

The mesoporous semiconductor is sensitized by soaking the semiconductor in a solution of the dye molecules. The mesoporous structure has approximately a thousand times more surface area than a flat surface.[5] The extra surface area allows for more dye molecules to be deposited in a specified surface area compared to a flat surface. The mesoporous layer is approximately 10 μm thick and has a porosity of approximately 50%. Visible light can travel through the mesoporous semiconductor to a depth

approximately equal to their wavelength ($\lambda = \sim 0.5\mu$m for visible light). Dye molecules adsorbed at the surface of the semiconductor can be excited by photons producing excited electrons which can be transferred into the mesoporous substrate. After the electron has entered the mesoporous semiconductor it travels through the semiconductor until it reaches the conducting back contact, once the electron has reached the contact it cannot recombine with either the dye molecules or the electrolyte. Excited residual dye molecules which are not bonded to the semiconductor are eventually destroyed by excited electrons causing dissociation.

TiO_2 is currently one of the most commonly used semiconductors used in DSCs. A mesoporous TiO_2 surface can be made by sintering TiO_2 nanoparticles, this produces a surface where the majority of the crystal facets are the anatase (101) surface. In the work presented in this thesis the dye molecules were studied absorbed onto a single crystal rutile TiO_2(110) substrate. An anatase nanocrystalline TiO_2 substrate would not have a well-defined periodic structure meaning that the molecules adsorbed onto the surface would not all be in the same adsorption state, this problem can be solved by using a single crystal substrate. The rutile TiO_2(110) surface was used instead of the anatase TiO_2(101) surface because the rutile crystals are cheaper and more practical for our experiments.

Bi-isonicotinic acid is the primary bonding ligand for many of the dye complexes studied in this thesis and the adsorption geometries of bi-isonicotinic acid on the anatase TiO_2(101) and rutile TiO_2(110) surfaces are practically the same.[14, 15] The optical band gaps of the anatase and rutile TiO_2 substrates are 3.20 and 3.05 eV respectively.[6, 16] Another reason for using the rutile TiO_2(110) crystal is that if an anatase TiO_2(101) crystals can undergo phase transition to rutile at high temperatures which could happen during annealing. A pure artificial anatase crystal also has a much smaller maximum area than a rutile crystal. For the measurements performed in this thesis a large area is necessary so that the sample can be swept for longer to prevent beam damage to the adsorbed molecules. By studying dye complexes adsorbed onto the rutile TiO_2(110) surface it is likely that we will obtain information that is also relevant to the nanostructured substrate used in actual DSCs.

1.2.4 Electrodes

Incident photons on a DSC device have to pass through the electrode to reach the dye molecules. This means that the electrode needs to absorb as little light as possible. In a photovoltaic DSC the cathode is responsible for reducing the electrolyte solution so that it can continue to replenish the electrons in the dye molecules after successful

charge transfer. In a water-splitting DSC device the cathode is responsible for reducing hydrogen ions to produce hydrogen molecules. The anode is in electrical contact with the semiconductor layer to remove the excited electrons which have transferred into the semiconductor. The electrodes are usually made of a glass or flexible plastic support coated with a conducting layer of tin-doped indium oxide or fluorine-doped tin oxide.[11]

1.2.5 Electrolyte

After successful charge transfer of an excited electron into the semiconductor layer, the dye molecule has a higher oxidation state which will hinder future charge transfer events. In the Grätzel solar cell an electron is donated from the oxidation of an iodide based electrolyte to fill the hole in the dye complex. The electrolyte is reduced at the cathode so that it can be continually reused to keep the dye molecules supplied with electrons. Using a liquid electrolyte such as the iodide solution means that the solution can be in constant contact with the cathode and the dye molecules within the mesoporous semiconductor. The main problem with using this solution is that it can cause leakages from the cell which decreases the effective lifetime of the DSC device. There is currently ongoing research in different technologies to develop a replacement for the electrolyte including ionic liquids,[17] polymer electrolytes[18] and hole conducting solids such as p-type semiconductors.[19–21] Using a hole-conducting solid means that the solid needs to be in close contact with the mesoporous semiconductor layer, when the hole-conducting material in its in liquid state it can be spin-coated onto the semiconductor.[22] The electrolyte needs to be suitable for the semiconductor, specifically the electronic energy levels of the components. The open circuit voltage of the cell is determined by the difference between the electron Fermi level of the semiconductor and the redox potential of the electrolyte.

1.3 Photocatalytic dye-sensitized solar cells

1.3.1 Hydrogen production and storage

Hydrogen is currently commercially produced using both chemical and biological methods. At present steam reforming of methane is one of the most popular techniques for producing hydrogen gas. Steam methane reforming involves heating a methane and steam mixture to high temperatures in the presence of a nickel catalyst producing carbon monoxide and hydrogen, additional hydrogen can be generated by oxidation of

carbon monoxide to carbon dioxide. This process has several major disadvantages compared to our proposed method using DSC technology, including the production of carbon dioxide during the reaction and the high energy required for the reaction. Similar disadvantages apply to partial oxidation of fossil fuels which produces hydrogen but also carbon monoxide.

Hydrogen can also be produced by electrolysis of water. An electric current is passed through the water leading to the production of hydrogen and oxygen molecules. This procedure uses a large amount of energy to create hydrogen and is currently uneconomical. There are some techniques that can improve the efficiency of electrolysis such as high temperature electrolysis using solid oxide electrolysis cells but this requires a large external source of heat such as a nuclear reactor. Proton exchange membrane electrolysis can be used to increase efficiency at lower temperatures by separating the hydrogen ions from the oxygen to prevent recombination.

The high energy requirement for these conventional production methods means that significant quantities of carbon dioxide will be released indirectly during the production process. By using sunlight to generate the energy needed to split water molecules into hydrogen and oxygen molecules we hope to create a method of hydrogen production that will not produce carbon dioxide or other atmospheric contaminants during operation. Dye-sensitized solar cells are relatively cheap and contain dye molecules that could be adapted to catalyse a chemical reaction. It is hoped that by experimenting with the chemical structure of the dye sensitizer we may be able to create an efficient and cheap source of hydrogen fuel with minimal environmental impact.

One issue with using hydrogen is that the fuel has a relatively high energy density by weight but a relatively low energy density by volume. Hydrogen can be compressed and cooled to improve its energy density but this requires energy and still does not have as high an energy density as in petroleum based fuels. Research is currently ongoing to determine whether another storage medium could be used to improve the energy density by volume of hydrogen. Various different molecules have been suggested to store the hydrogen molecules such as carbon nanotubes and metal-organic frameworks. Improvements to storage will make hydrogen fuel more viable.[23–28]

1.3.2 Water-splitting DSCs

Equation 1.3.1 shows a simple reaction scheme for the water-splitting reaction using energy from absorbed photons of visible light to split water molecules into hydrogen and oxygen molecules. Photons with wavelengths below approximately 750nm technically

have enough energy to perform the water-splitting reaction. Higher energy photons are likely to be needed due to inefficiencies in the solar cell.

$$2H_2O + 4hv \longrightarrow 2H_2 + O_2 \tag{1.3.1}$$

The water-splitting reaction has previously been performed using both single and multi-centre ruthenium-based dye complexes both on surfaces and in solution.[29–34] A water-splitting dye complex based on a DSC would absorb photons of light causing the promotion of an electron to a higher energy unoccupied molecular orbital within the molecule. If the unoccupied level overlaps energetically with the semiconductor conduction band this electron could then transfer into the substrate. The loss of an electron from the central ruthenium atom causes an increase in the oxidation state of the ruthenium atom. Initially the ruthenium atom is in the +2 oxidation state, each successful charge transfer event would increase the oxidation state by +1 to a maximum oxidation state of +5. H^+ ions are lost from the water molecule at the same time as the excited electrons are transferred into the substrate in a process called proton-coupled electron transport (PCET). As the oxidation state of the ruthenium ion increases the water molecule changes its bonding to the ruthenium ion to stabilise the complex. The H^+ ions and the electrons which transferred into the substrate can combine at the cathode to produce hydrogen molecules.

Initially the multi-centre dye complex is deposited on the surface with an intact water molecule, the system has to undergo an initiation step before progressing into the main catalytic cycle. A chemical equation for the initiation step adapted from Reference [31] is shown in Equation 1.3.2.

$$TiO_2|Ru^{II}|Ru^{II}OH_2 + hv \longrightarrow TiO_2|Ru^{II*}|Ru^{II}OH_2 \longrightarrow TiO_2|Ru^{II}|Ru^{III}OH + e^- + H^+ \tag{1.3.2}$$

The initiation step consists of photoexcitation of an electron in the ruthenium atom closest to the substrate (the charge transfer centre) and then the charge transfer of that excited electron from the dye molecule into the semiconductor layer of the cell. The removal of a valence electron from the dye molecule changes the oxidation state of the charge transfer centre's ruthenium atom from +2 to +3. The ruthenium atom attached to the water molecule (the reaction centre) then donates an electron to the charge transfer centre changing its own oxidation state from +2 to +3 and reducing the oxidation state of the charge transfer centre to +2. Electron transfer from the reaction centre's metal complex induces the loss of a H^+ ion from the water molecule through PCET

leaving behind a negatively charged hydroxyl group so that the total charge of the reaction centre remains +2.

After the initiation step has been completed the catalytic cycle can be started. The first stage of the cycle is shown in equation 1.3.3 adapted from [31].

$$\begin{aligned} TiO_2|Ru^{II}|Ru^{III}OH + 2hv &\longrightarrow TiO_2|Ru^{II}|Ru^{V}O + 2e^- + H^+ \\ TiO_2|Ru^{II}|Ru^{V}O + H_2O &\longrightarrow TiO_2|Ru^{II}|Ru^{III}OOH + H^+ \end{aligned} \quad (1.3.3)$$

The first major step begins with two successful charge transfer events leading to the removal of two electrons from the ruthenium atom in the reaction centre giving it an oxidation state of +5, also a H^+ ion from the hydroxyl group is removed leaving a doubly negatively charged oxygen atom attached to the ruthenium atom in the reaction centre with a double bond. The total charge of the reaction centre is increased from +2 to +3 due to the unbalanced removal of electrons and protons, the additional charge on the reaction centre allows for nucleophilic attack from another water molecule. The attacking water molecule loses two electrons to the ruthenium atom and another hydrogen ion leading to the formation of a OOH^- species attached to the ruthenium atom in the reaction centre. This leaves the ruthenium atom with an oxidation state of +3 with the overall charge of the reaction centre returning to +2.

The second stage of the catalytic cycle is similar to the first but the species attached to the reaction centre now has two oxygen atoms and an oxygen molecule is emitted from the complex. The chemical formula for the reaction is shown in equation 1.3.4 adapted from [31].

$$\begin{aligned} TiO_2|Ru^{II}|Ru^{III}OOH + 2hv &\longrightarrow TiO_2|Ru^{II}|Ru^{V}O_2 + 2e^- + H^+ \\ TiO_2|Ru^{II}|Ru^{V}O_2 + H_2O &\longrightarrow TiO_2|Ru^{II}|Ru^{III}OH + H^+ + O_2 \end{aligned} \quad (1.3.4)$$

The second major step of the catalytic cycle begins with two more successful charge transfer events, this leaves the reaction centre's ruthenium atom in the +5 oxidation state. Another H^+ ion is lost from the OOH^- species to form an O_2^{2-} species. The overall charge of the reaction centre then increases to +3, this leads to nucleophilic attack from another water molecule causing the loss of the oxygen molecule and a H^+ ion from the water molecule. This leaves the reaction centre in a state identical to its state after the intiation step, the catalytic cycle can then repeat. The main catalytic cycle splits two water molecules to produce an O_2 molecule, four electrons and four H^+ ions.

The protons can then recombine with the electrons initially transferred to the substrate at the cathode producing two H_2 molecules. The equation for the cathode reaction is shown below in equation 1.3.5

$$4H^+ + 4e^- \longrightarrow 2H_2 \tag{1.3.5}$$

A water-splitting DSC would use Grätzel cell architecture as described in Section 1.2. The main difference between the architectures of a standard photovoltaic Grätzel cell and a water-splitting cell would be the electrolyte component. With a water-splitting DSC there it would be detrimental to replace electrons lost from the charge transfer process as this would interfere with the water-splitting process. The electrolyte needs to be mostly composed of water molecules which may lead to enhanced lifetimes for the solar cells due to not needing the corrosive iodide based electrolyte using in photovoltaic devices.

The ruthenium metal ions in the complexes could be replaced by other transition metal ions, the main requirement is that the ion needs to be capable of multiple different oxidation states. So far other water-splitting dye complexes have been developed based on iron,[35] iridium,[36, 37] rhodium[38] and cobalt metal centres.[39] Studying different metal centres may lead to optimisation of the water-splitting process using organometallic dye molecules.

1.4 Future prospects for dye-sensitized solar cells

1.4.1 Photovoltaic dyes

Currently dye complexes used in photovoltaic DSC devices tend to use ruthenium metal ions as the core of the dye sensitizing molecules. Ruthenium based complexes are usually stable and provide very advantageous photophysical properties. Ruthenium is a relatively rare metal and may become increasingly expensive in the future, so alternative metal ions may be needed in the future to keep the cost of producing DSC devices low. Also using an alternative metal ion may lead to different photophysical properties of the complex such as greater charge transfer efficiency or stability. One possible alternative is to use copper ions as the central ion,[40, 41] copper is a very abundant metal and is relatively cheap. Other potential alternatives include platinum,[42] nickel[43] and iridium.[44]

It may also possible to produce an efficient dye sensitizer complex without using a central metal ion at all.[45, 46] These purely organic dyes could have their properties

precisely tuned by changing the molecular structure and could prove to be a lot cheaper than inorganic dye molecules. The organic dyes can be tuned to absorb a large proportion of incident light. Also the positioning of the HOMO and the LUMO orbitals on the molecule can be adjusted to maximise the efficiency of the dye sensitizer complex. The HOMO can be located on the furthest part of the molecule from the substrate so that the hole left after successful charge transfer can be more effectively replenished by electrons from the iodide solution in the Grätzel cell. The LUMO can be adjusted to have maximum overlap with the substrate orbitals to increase the efficiency of electron transfer from excited adsorbed molecules to the semiconductor substrate. Also by increasing the spatial overlap of the HOMO and LUMO orbitals the probability of electron excitation can be increased.

Alternative photovoltaic dye sensitizers could lead to different options for producing effective water-splitting dye catalysts. As further studies are conducted on these alternative types of dye complex more information will be available to help design better dye molecules for both photovoltaic and water-splitting applications.

1.4.2 Quantum dot solar cells

Solar cells have been developed based on quantum dots which are small particles with quantised electron energy levels. The band gap of the particles can be tuned by changing the size of the particles, the range of energies that the cell is sensitized to could also be increased by using a range of quantum dots sizes. Quantum dots also have other advantageous properties such as the potential for generating multiple excitons from one photon and hot carrier capture where the electron does not lose significant quantities of energy generating heat.[47] At the moment the efficiency is not as high as for DSC devices but multi-junction cells and the other advantages of quantum dot cells may lead to highly efficient solar cells.[48]

1.4.3 Perovskite cells

Recently a perovskite solar cell was produced which had a photon conversion efficiency of 14-15% making it one of the most efficient dye-based solar cells.[49] The perovskite has the chemical formula $CH_3NH_3PbI_3$. The solar cell is solid state meaning it does not need an electrolyte solution, this should mean that the cell will have a longer effective lifetime than DSC devices as the cells use corrosive iodide solution. Due to the solubility of perovskite materials this type of solar cell would be unsuitable for a water-splitting device.

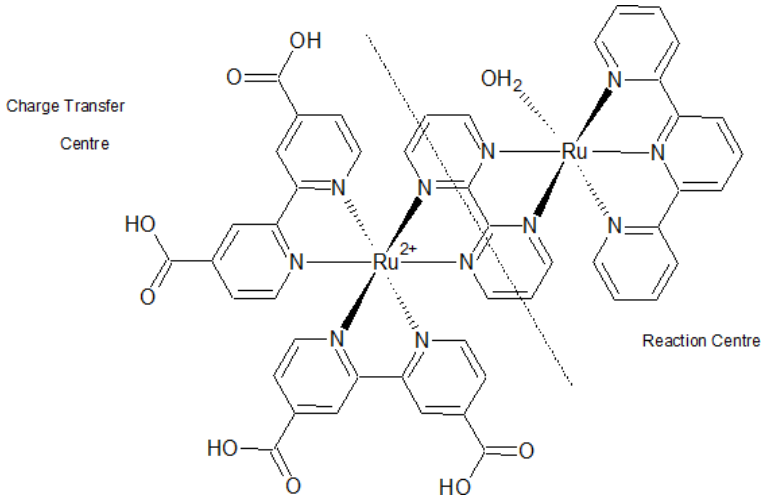

Figure 1.5: Diagram showing the initial design of a multi-centre water-splitting dye complex, the diagram also shows the two centres called the charge transfer centre and the reaction centre.

1.5 Topics researched in this thesis

The two types of metal centre in a multi-centre water-splitting dye complex have been labeled the charge transfer centre and the reaction centre, as shown in Figure 1.5.

By studying model molecules which represent each centre it should be possible to optimise the design of a multi-centre dye complex. To optimise the design of the charge transfer centre we studied several bi-isonicotinic acid based complexes and several dipyrrin-based complexes. By studying these molecules we hope to gain a deeper understanding of charge transfer from molecular adsorbates to substrates. This information can be used to design more efficient dye sensitizers for photovoltaic devices or to optimise a water-splitting complex so that the initial charge transfer process is as fast as possible. A single-centre water-splitting complex was also studied which could also be thought of as a model of the reaction centre. The information from these studies could be used to optimise designs of both single and multi-centre water-splitting dye complexes. In addition the information from these studies will aid the interpretation of data obtained from experiments on multi-centre dye complexes.

Chapters 2-5 are concerned with the techniques used in the experiments. In Chapter 6 experimental data is presented on bi-isonicotinic acid dye complexes adsorbed onto the surface of a rutile TiO_2(110) substrate, the dye complexes are models of the charge transfer centre of a multi-centre water-splitting dye complex. One of the dye complexes studied in this chapter is the N3 dye complex, which is currently one of the most efficient dye sensitizers in use in photovoltaic DSCs. N3's high efficiency could make the dye a good basis for the charge transfer centre of a water-splitting complex.

The charge transfer timescales, bonding geometries and orbital energetics of the molecules were studied to provide information on the efficiency of electron injection from the adsorbed molecules to the substrate. The molecules were deposited using the UHV electrospray deposition technique which is described in detail in Chapter 5, depositing the molecules under ultra-high vacuum reduces the impact of atmospheric contaminants. Experimental data on dipyrrin-based dye complexes adsorbed onto rutile TiO_2(110) is presented in Chapter 7, these molecules have significant structural differences from the bi-isonicotinic acid based complexes. The dipyrrin ligands have a larger conjugated π system than bi-isonicotinic acid ligands which should lead to more intense absorption of incident light. In Chapter 8 experimental data on a single centre water-splitting dye complex adsorbed onto rutile TiO_2(110) is presented which could also be used as the reaction centre of a multi-centre water-splitting dye complex. This work will be the first study of most of these molecules where the samples are both prepared and analysed under UHV conditions, the only exception is the N3 dye complex which has previously been studied using these techniques.[7]

CHAPTER 2

Synchrotron radiation

2.1 Introduction

In order to observe the electronic energy levels of the systems studied in this work we needed to excite electrons within the molecules and observe decay products from the excited states. Synchrotrons provide a source of intense electromagnetic radiation at a user-defined energy which allows us to excite electrons into previously unoccupied electronic levels. This allows us to study the sample's occupied and unoccupied electronic orbitals. One of the major advantages of using synchrotron radiation compared to femtosecond laser sources is that it is possible to isolate molecular orbitals present on specific elements, such as nitrogen. The techniques using the decay products of the excited states are described in detail in chapters 3 and 4. This chapter will deal with the generation of synchrotron light and how this type of radiation can be used to study samples.

When a charged particle travelling at relativistic speed changes momentum it emits synchrotron radiation. To emit photons of significant energy the particles have to move at very high speed. In order to achieve this the charged particles need to have a long mean free path which can only occur under vacuum conditions. This means that the synchrotron has to be kept under vacuum to produce radiation. Natural sources of synchrotron radiation occur in deep space where there is both a high vacuum and strong magnetic fields, as shown in Figure 2.1. By creating this radiation artificially and with specific characteristics such as wavelength it can be used to study electronic energy levels in a sample, this provides useful data to help with DSC design.

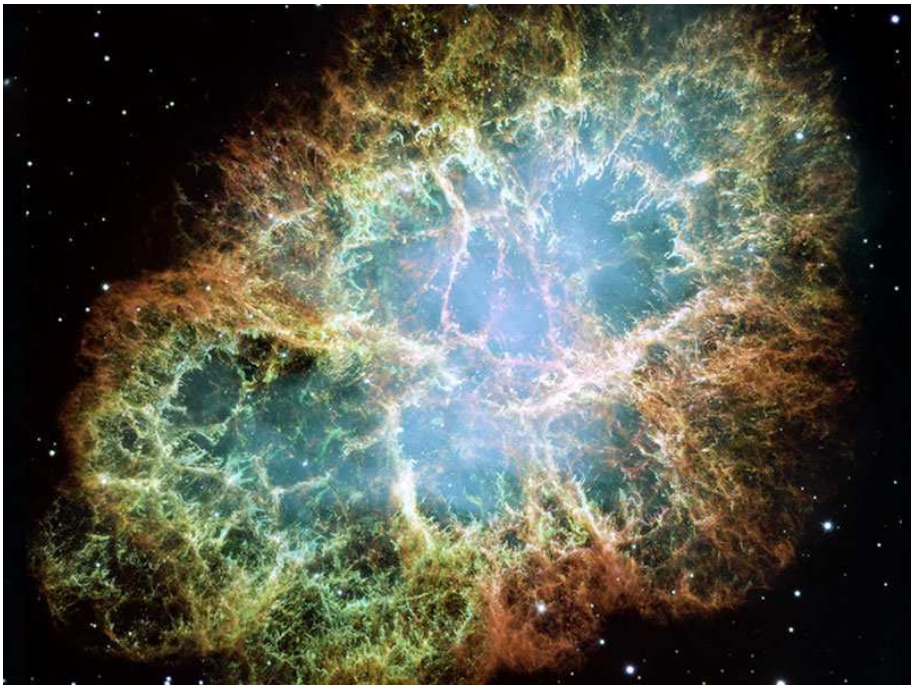

Figure 2.1: Hubble space telescope image of the crab nebula. Synchrotron radiation appears as a bluish glow in the central region of the photo. The synchrotron radiation is at gamma-ray energies and is probably due to electrons trapped in the strong magnetic field of a pulsar.[50, 51]

2.2 Synchrotron layout

The synchrotron has various different component stages which produce electrons, accelerate them up to relativistic speeds and then changes their momentum to produce synchrotron radiation. The radiation produced by a synchrotron is intense polarised light with a large energy range extending to hard X-rays. A schematic of a synchrotron is shown in Figure 2.2 with the main stages labelled 1-6.

An electron gun (1) produces electrons using a hot filament, these electrons are then accelerated to relativistic speeds by a linear accelerator (2) and a booster ring (3). The high-speed electrons are then transferred to the storage ring (4). The ring actually consists of a series of straight sections with curved sections where magnetic fields applied perpendicular to the electron's motion cause the electrons to change path. Bending magnets or insertion devices are used to make the electrons turn and are described in the next section. As the electrons change direction they emit synchrotron radiation at a tangent to the ring. This light then travels down a beamline (5) where it is focused so that it can be used in experiments at the end station (6). The end station typically contains equipment to measure the various particles emitted from samples which have been excited with synchrotron light.

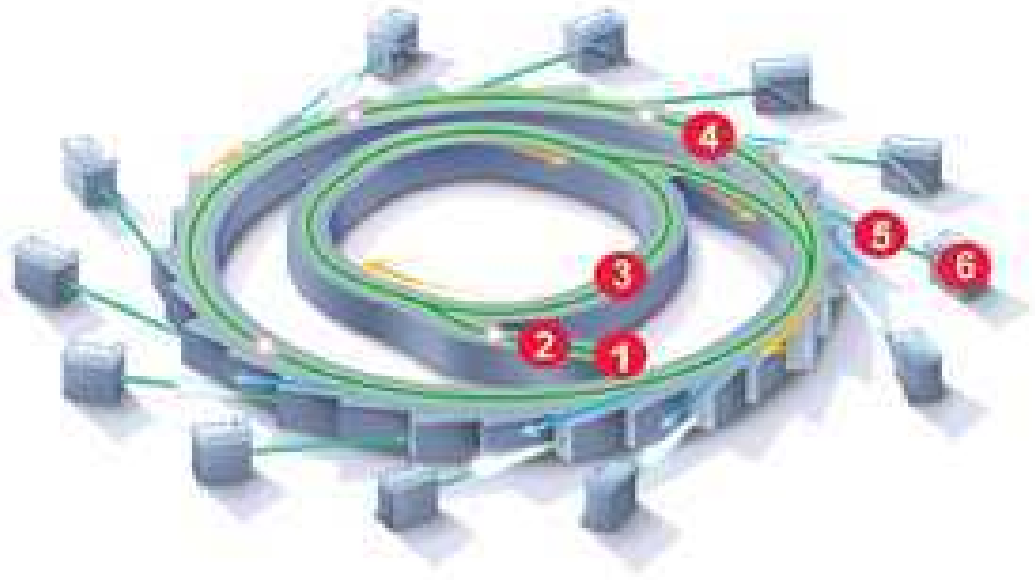

Figure 2.2: Schematic diagram of the Australian synchrotron.[52] The labels are (1) the electron gun, (2) linear accelerator, (3) booster ring, (4) storage ring, (5) beamline and (6) end station. The different stages are described in detail in the text

2.3 Wigglers and undulators

To generate synchrotron radiation bending magnets are used, using a single magnet as the electrons pass through the magnetic field they change direction and emit radiation with a broad energy range. The radiation is emitted along a tangent of the ring and sweeps across as the electrons move along the ring.

Different configurations of magnets can be used to increase the amount of radiation generated per electron cycle. This is achieved by causing the electrons to oscillate multiple times using a series of magnets with alternating poles. These types of electron deflectors are called wigglers and undulators.

The wiggler configuration of magnets causes the electrons to oscillate and emit radiation from side to side. The radiation will sweep back and forth across the entrance to the beamline producing usable light in short pulses. Undulator devices use weaker magnets to reduce the amplitude of the oscillations, this means the synchrotron radiation is produced in a more consistent direction and illuminates the beamline constantly.

The dimensionless magnetic deflection parameter K can be used to describe the difference between how an electron moves in an undulator or a wiggler device.

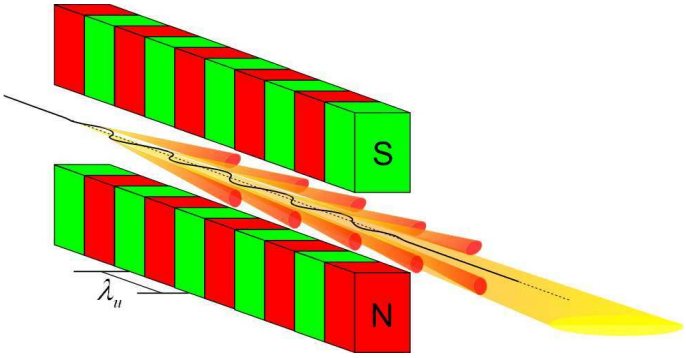

Figure 2.3: A series of magnets configured as an undulator device. The magnets cause the electron to undulate and emit radiation along the path of the ring.[53]

$$K = \frac{eB\lambda_u}{2\pi\beta m_e c} \tag{2.3.1}$$

In this equation e is the electronic charge, B is the magnetic field, λ_u is the wavelength of the undulation of the electron, β is the velocity of the electron relative to the speed of light, m_e is the mass of an electron at rest and c is the speed of light. The maximum excursion angle of the electrons is $\frac{K}{\gamma}$ and the maximum radiation emission angle is $\frac{1}{\gamma}$ where γ is the Lorentz contraction factor. The Lorentz contraction factor is needed as the electrons are travelling at relativistic speeds. In a strong magnetic field such as in the wiggler configuration $K \gg 1$ and the excursion angle is much larger than the emission angle of the radiation meaning that the radiation becomes spread out spatially over distance. In a weak magnetic field such as within an undulator device $K \leq 1$, the excursion angle is lower than the radiation emission angle. The radiation emitted from an undulator continues to overlap for a significant distance which can cause the radiation to undergo interference.

Electrons travelling through an undulator have a small excursion angle. This produces radiation with a relatively high photon flux within a small energy range. As there are multiple light cones emitted the beam can undergo constructive interference. The interference effect can be tuned to certain wavelengths by altering the magnet geometries. For instance, the gap between the magnet arrays can be changed. The magnet arrays can also be tilted with respect to each other to produce radiation with a broad energy range and roughly constant intensity.

The high intensity of the radiation emitted by the synchrotron can be used to measure spectra relatively quickly. It can however cause beam damage to the sample particularly if the sample is organic. The beam can cause chemical bonds to break in the sample which would not occur in normal operation. The damage can be seen in near-edge x-ray absorption fine structure (NEXAFS) spectra which provide information on

molecular orbitals. For each molecule it is necessary to determine how long the sample can be kept in the beam before significant damage occurs. The sample can be moved periodically or constantly during data acquisition to prevent beam damage from significantly affecting the results.

2.4 Beamline I311

A beamline's purpose is to produce radiation suitable for use in experiments on the end-station from the output of the synchrotron. The undulator beamline I311 at the MAX II synchrotron of the National Swedish Laboratory MAX-lab was used for most of the synchrotron based experiments in this thesis. All of the work presented in Chapter 6 on model charge transfer centres was performed at the I311 beamline as well as the near-edge x-ray absorption fine structure (NEXAFS) and resonant photoemission (RPES) spectra presented in Chapters 7 and 8. A schematic figure of beamline I311 is shown in Figure 2.4 and a photograph of the beamline is shown in Figure 2.5.

Light exiting the synchrotron is focused using a series of mirrors to ensure that the intensity of the photon beam is not diminished before reaching the sample. The photon energy of the light received at the end-station is selected using a monochromator consisting of either a crystal or a grating. The I311 beamline has a grating giving access to an energy range of 30-1500 eV.[54]

The end-station of a beamline usually consists of several connected ultra-high vacuum chambers. The major chambers are a preparation chamber where the samples are cleaned and then molecules can be deposited on the surface, and an analysis chamber where the synchrotron light can be used to perform experiments on the sample. The two chambers are separated by a UHV valve, this allows high pressure preparation techniques to be used whilst maintaining a low base pressure in the analysis chamber. A photograph of the I311 end station is shown in Figure 2.6.

The preparation chamber of end station I311 is equipped with a sputter gun. The gun accelerates argon ions towards the sample using an electric field. The ions are inert and clean the surface of the sample by ablating the top layers of the surface. The sample can be moved in x, y and z using a manipulator, which also allows for rotation of the sample. The manipulator also contains electrical connections allowing us to pass a current through a heater and anneal the sample at high temperatures. The heat energy provided by the heater allows atoms in the sample to move and repair defects caused by the sputtering process.

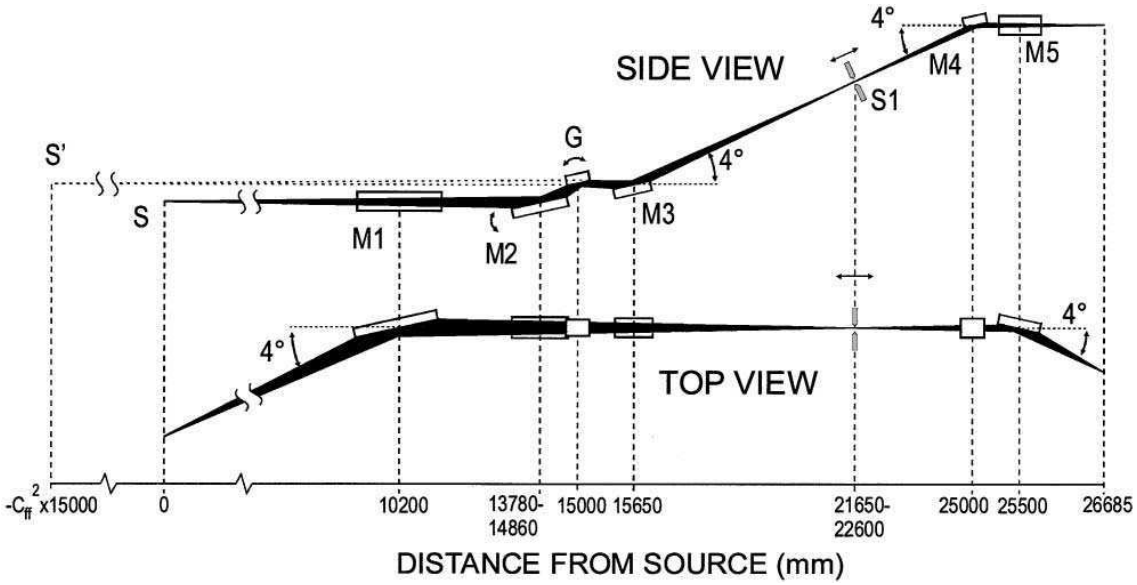

Figure 2.4: Schematic figure of the I311 beamline at the MAX-II synchrotron in MAX-lab, Sweden. The optical elements are: M1, horizontally focusing pre-mirror: M2, rotatable plane mirror; G, plane grating; M3, spherical focusing mirror; M4 and M5, spherical re-focusing mirrors. S1 is a movable exit slit. The real source is at S and the virtual monochromatic source at S'. The figure is adapted from reference [54].

The analysis chamber has an electron analyser which is capable of measuring the kinetic energy of electrons emitted from the sample. This equipment allows us to measure photoemission spectra which allows us to determine which elements are present in the sample and their chemical environments. The analyser can also be used as a NEXAFS detector measuring the number of electrons emitted as a function of photon energy, this can provide information on the molecular orbitals of the sample. RPES spectra can also be measured which allow us to measure charge transfer timescales on the low-femtosecond timescale. The principles behind the electron analyser and the techniques described above are described in Chapters 3 and 4.

Keeping the sample under ultra-high vacuum prevents the clean surface of the sample from being contaminated too extensively. As the contamination rate is proportional to the pressure of the chamber, at UHV pressures the surface will remain clean for long enough to deposit molecules onto the surface. To minimise the pressure in the chamber the system is baked to approximately 150 °C. The thermal energy evaporates molecules from the surfaces of the chamber which can then be removed by the vacuum pumps attached to the chamber. The chamber is heated using heating tapes wrapped around the chamber and covered with aluminium foil. The foil acts as an insulator, slowing the rate of heat escaping into the surrounding air during bake out and also slowing the

Figure 2.5: Photograph of the I311 beamline at the MAX-II synchrotron in MAX-lab, Sweden.

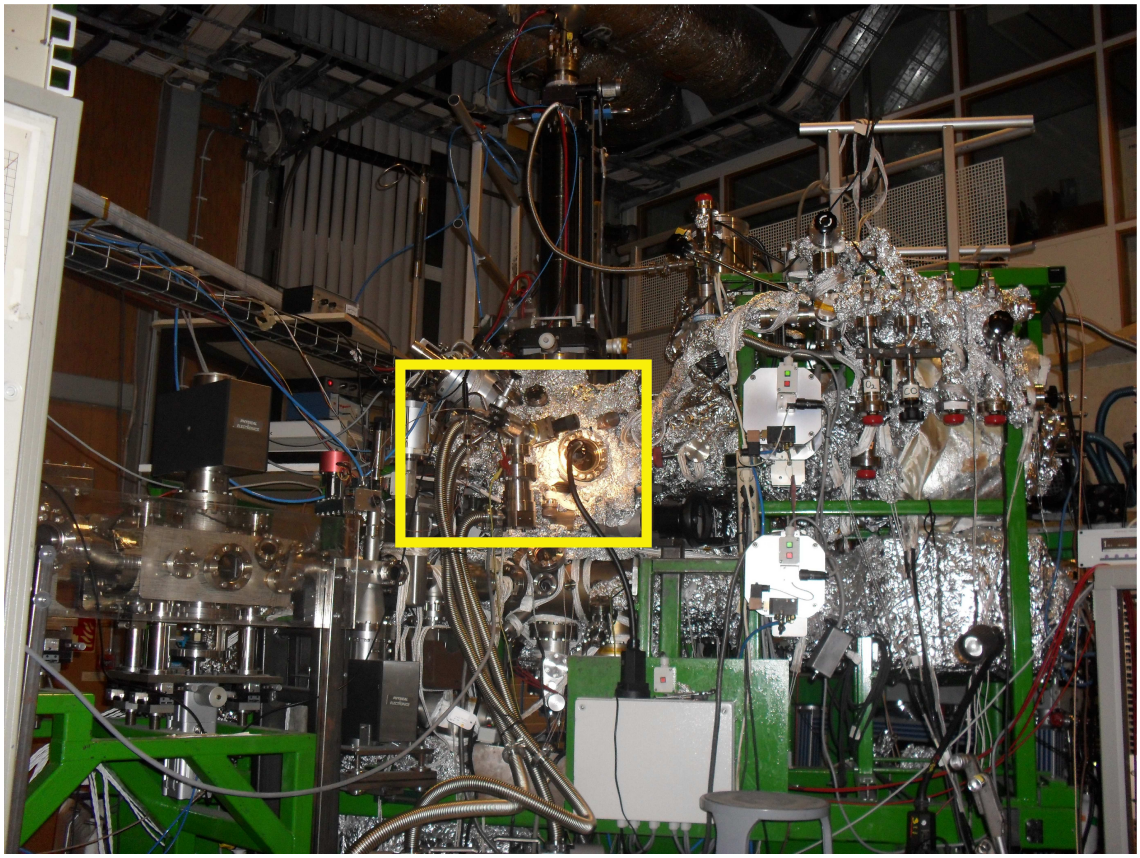

Figure 2.6: Photograph of the I311 end station. The manipulator can be seen at the top of the photograph, the electron analyser is on the other side of the end station and cannot be seen in this photograph. The electrospray deposition apparatus is highlighted by the yellow rectangle.

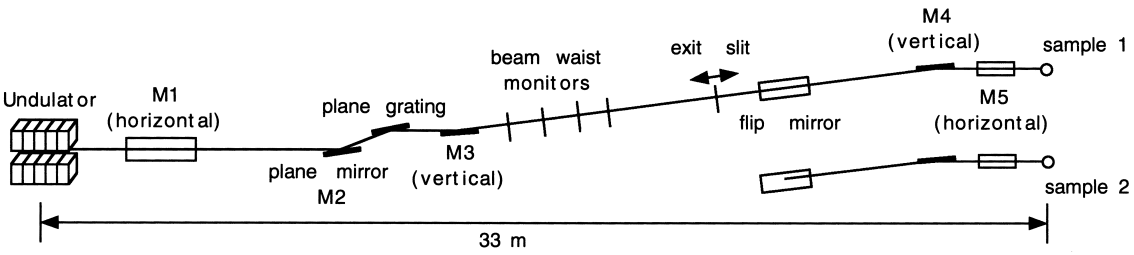

Figure 2.7: Schematic figure of the I511 beamline at the MAX-II synchrotron in MAX-lab, Sweden. The figure is adapted from reference [55].

rate of heating and cooling which helps to prevent damage to chamber windows and other sensitive components.

2.5 Other Beamlines

Some of the experimental data in this thesis was obtained from work performed at the undulator beamline I511 at the MAX II synchrotron of the National Swedish Laboratory MAX-lab. The photoemission data on single-centre water-splitting complexes was obtained from experiments on the I511 beamline. A schematic figure of beamline I511 is shown in Figure 2.7.

Beamline I511 has a few unique features compared to beamline I311. The beamline splits and has two end stations; the surface end station I511-1 and the bulk end station I511-3. A flip mirror directs the synchrotron light towards the end station in use. In this work only the surface science end station I511-1 was used. The I511-1 surface science endstation is set up so that the incoming photon beam is at grazing incidence to the sample, which provides greater sensitivity to the atoms on the surface. The monochromator grating on the beamline has a photon energy range from 90-1500 eV.[55] A Scienta R4000 electron analyser was attached to the chamber to detect the electrons emitted from the sample after excitation by the synchrotron beam.

Beamline D1011 at the MAX II synchrotron of the National Swedish Laboratory MAX-lab was used to obtain photoemission data on the dipyrrin molecules studied in Chapter 7. The beamline uses a bending magnet to generate the synchrotron light, this means that the photon flux on the sample is several orders of magnitude lower than the undulator beamlines I311 and I511. This lowered photon flux means that RPES spectra would take an excessive amount of time to complete, but photoemission spectra can be obtained without significantly damaging the molecule. A schematic diagram of the D1011 beamline is shown in Figure 2.8.

The beamline has two experimental chambers with radiation passing through the front

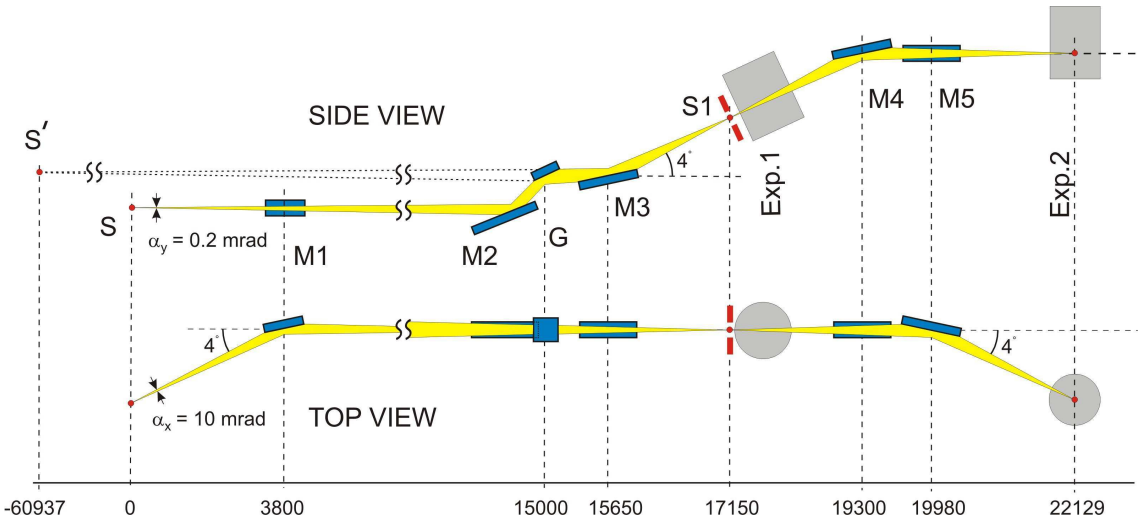

Figure 2.8: Schematic figure of the D1011 beamline at the MAX-II synchrotron in MAX-lab, Sweden. S is the dipole magnet source, M1 is a horizontally focusing spherical mirror, M2 is a plane mirror, G is the grating, M3 is a vertically focusing plane elliptical mirror, S1 is the exit slit of the monochromator and Exp. 1 is the experimental station used in this work. The rest of the schematic shows the mirrors and second end station which were not needed in this work. The figure is adapted from reference [57].

chamber to each the back chamber. In these experiments only the front chamber was used which has a VG Scienta SES200 electron analyser for surface science experiments. The monochromator grating used on the D1011 beamline has a photon energy range from 40-1500 eV.[56]

2.6 Sample geometry

If the synchrotron light is incident perpendicular to the surface the light will penetrate to a depth of approximately 100 nm. This means that electrons could be detected which originated from the substrate bulk instead of the adsorbed layer of molecules. By altering the angle of incidence of the light on the sample surface the penetration depth of the light can be altered. This is only particularly significant when using emitted photons to study the sample. Emitted electrons will undergo interactions with the bulk that severely reduce their escape depth below the penetration depth of the incident light. Changing the angle of incidence also changes the geometry of the illuminated spot on the sample surface spreading the beam out and causing less beam damage to the adsorbed molecules.

The main factor that affects how many electrons can escape from below a particular

depth in a surface is the kinetic energy of the emitted electrons as described in Section 3.2.10. Also many of the elements present in the adsorbed molecules are not present in the substrate or have a significant difference in binding energy allowing us to separate the molecular and substrate peaks based on their binding energies as described in Chapter 3.

CHAPTER 3

Adsorption of molecules to surfaces

3.1 Introduction

In DSC devices the dye complexes are adsorbed onto the surface of a semiconductor which allows for charge transfer from the dye complex to the semiconductor, the adsorption of the molecule is therefore important for the efficiency of the DSC device. An image of a molecule attached to the surface is shown in Figure 3.1. This chapter describes the techniques that have been used to study the adsorption of dye complexes on a surface. The information obtained by the techniques can be used to analyse the upper atomic layers of a surface and the atoms or molecules adsorbed onto the surface.

The adsorption of molecules onto a surface can change both the physical and electronic structures of the adsorbate molecule. The electronic energy levels in the sample can be investigated using either electrons or photons. These techniques can reveal both occupied and unoccupied electronic orbitals in the sample. By analysing the changes in the energy levels of certain orbitals it is possible to determine which atoms are involved in bonding to the surface. This experimental data can be used to perform computer simulations on the surface, this can give additional information that can be used to help interpret experimental results.

When performing experiments on surfaces a simple surface is preferred so that the molecules can adsorb consistently and the results are easier to interpret. The simplest surfaces are flat crystal surfaces which have been cut to a specific plane, this gives a well-defined periodic structure with long range order that is perfect for experiments. When the crystal is cut the reciprocal of the Cartesian axis intercepts of the cut are taken giving three integers which are the Miller indices used to define the crystal surface. In this work the TiO_2(110) crystal plane was used for all experimental work. The structure of this surface is shown in Figure 3.2.

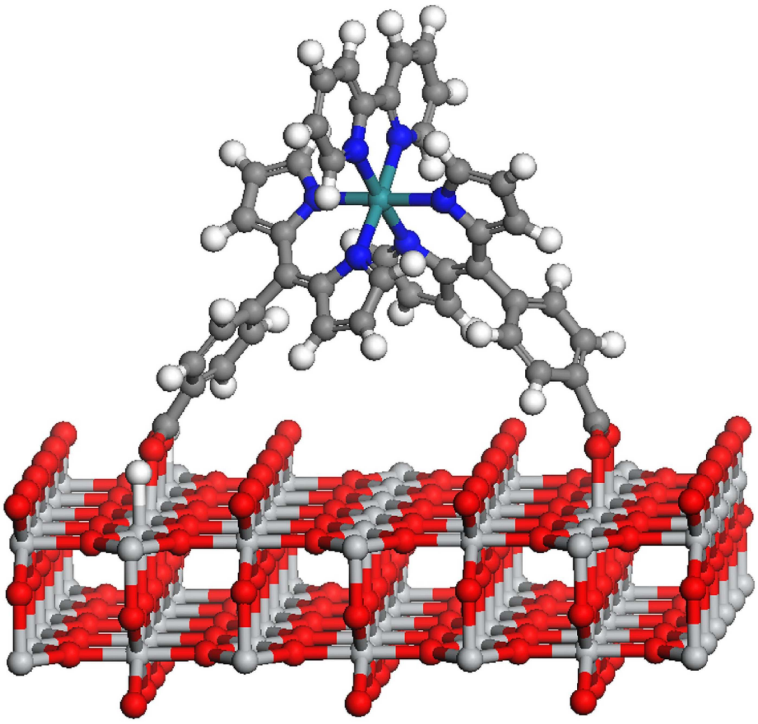

Figure 3.1: Calculated structure of a PY2 molecule adsorbed on a rutile TiO_2(110) surface. This structure is predicted by DFT as described in Chapter 3.4 and the specific parameters of this calculation are given in Chapter 7.2

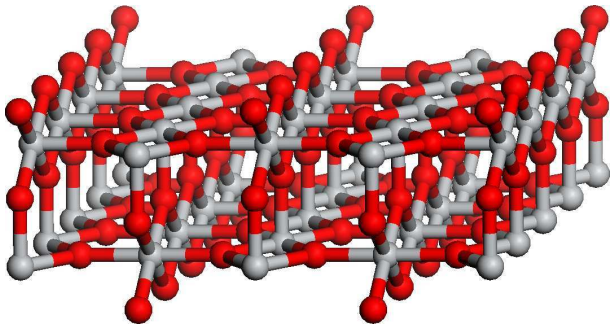

Figure 3.2: Structure of the TiO_2(110) crystal plane, red spheres represent oxygen atoms and grey spheres titanium atoms.

In this work studying the molecules was the main priority, the different chemical structures of these molecules will lead to differences in how the molecules adsorb to the surface and consequently how efficient a DSC using these molecules would be. In these experiments the TiO_2(110) surface is not studied as extensively as the molecules. The rutile surface has already been investigated by other groups and the surface is not the same as the nanocrystalline TiO_2 substrate used in real DSC devices. The surface of the substrate is however important to the functioning of the DSC device and there are ongoing studies in this field. For example the structure of the substrate could be made into a fractal structure allowing for a more direct electrical pathway than in conventional nanostructured semiconductors.[58] This should help to prevent recombination of the electron with the original molecule it transferred from.

3.2 Photoemission spectroscopy

3.2.1 Bound electrons

There are numerous atoms in the dye molecule and substrate of a DSC system which contain bound electrons. These electrons have different energy levels which are determined by the orbital the electron occupies and the chemical environment of the electron. The chemical environment of the electron depends on factors such as the identity of the host atom, the atom's oxidation state and the chemical bonds formed by the host atom. A diagram illustrating the different energy levels of an electron in a molecule is shown in Figure 3.3. The Fermi level is defined as the energy at which the probability of an electron occupying a level is $1/2$. The vacuum level is defined as the energy at which the electron no longer feels any interaction from the host system and the electron has zero kinetic energy. If the electron gained any further energy it would be used to increase its kinetic energy allowing the electron to move in the vacuum. The electrons have an ionisation potential which is the energy needed to remove an electron from the molecule. The ionisation potential can be split into the binding energy which is the amount of energy that the relevant orbital is below the Fermi level, and the work function which is the energy needed to move an electron from the Fermi level to the vacuum level. Unoccupied electronic levels lie between the Fermi level and the vacuum level. Electrons from lower occupied energy levels can be excited into these levels temporarily until the system relaxes and the excited electrons return to orbitals at a lower energy level.

In isolated atoms the electrons are in atomic energy levels, which can be represented by the quantum numbers n and l. n is the principal quantum number and l is the

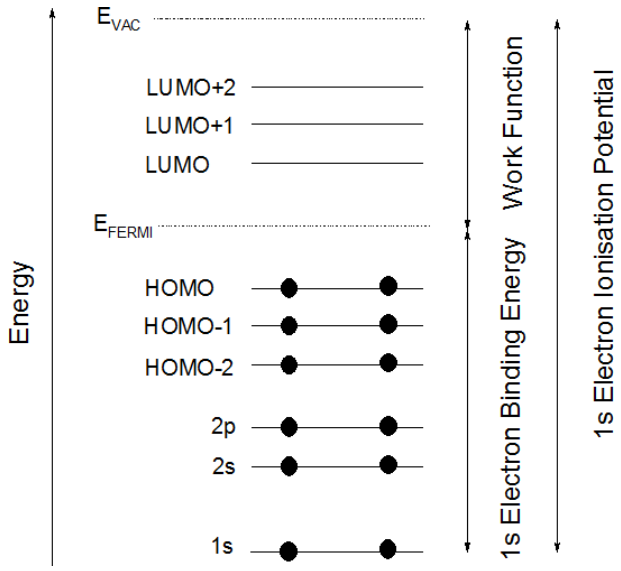

Figure 3.3: Schematic energy level diagram of bound electrons in a molecule showing some of the terms used to describe the system. LUMO and HOMO refer to lowest unoccupied molecular orbital and highest occupied molecular orbital respectively.

azimuthal quantum number, which refer to the shell number and the orbital angular momentum respectively. The quantum numbers describe the energy of the orbitals in a system. The 1s orbital has the highest binding energy followed by the 2s and then 2p orbitals. No two electrons in a system can have the same quantum numbers. The spin quantum number s can have only two values $+1/2$ or $-1/2$ so each orbital can contain a maximum of two electrons. Orbitals which are not involved in chemical bonding are known as core-levels, they have high binding energies due to their close proximity to the atomic nucleus. Orbitals with low binding energies are known as valence levels and can be used to form chemical bonds.

In molecules the electrons can exist in molecular orbitals formed from the mixing of individual atomic orbitals. Molecular orbitals contain weakly bound electrons and the occupied molecular orbitals can be too similar in energy to be resolved so they are collectively called the valence band. Conjugated molecules containing alternating single and double chemical bonds can have very large molecular orbitals, in highly conjugated molecules the molecular orbitals can extend over the entire molecule. In these highly conjugated systems the energy difference between orbitals can be reduced to the point that electrons can be excited to unoccupied orbitals by absorbing photons of visible light. Inorganic dye complexes can undergo metal-to-ligand charge transfer (MLCT). MLCT transitions can produce very intense absorption bands in the visible light region as they obey spectroscopic selection rules. The N3 dye complex has a very

strong MLCT transition which contributes to its high efficiency as a DSC sensitizer.[7]

Due to the added complexity involved in studying molecular orbitals a different nomenclature is used to refer to the orbitals which does not require as much information on the system. The highest occupied molecular orbital (HOMO) is defined as the lowest binding energy orbital which contains electrons, the next lowest binding energy orbital is called the HOMO-1, then the HOMO-2 etc. The lowest unoccupied molecular orbital (LUMO) is defined as the first unoccupied state above the Fermi level, the LUMO+1 is the next state and so on. This allows us to study realistic systems with large numbers of orbitals and electrons in a consistent fashion.

3.2.2 Uses of photoemission spectroscopy

Photoemission spectroscopy allows us to measure the binding energy of electrons within a sample. Each element produces a characteristic photoemission spectrum due to the electronic structure of the atom. Atoms with a high atomic number will have more occupied orbitals than atoms with a lower atomic number, meaning more peaks will be visible in a photoemission spectrum. Binding energies are used to identify atoms as the binding energy of electrons is affected by differences in the number of protons in each atomic nucleus and the distribution of other electrons providing charge screening of the nucleus.

The binding energies of electrons are also affected by the local chemical environment of the electrons. For example, if the target atom is chemically bonded to a more electronegative atom then the electron density near the target atom decreases increasing the effective charge of the nucleus. This would cause an increase in the binding energy of the electrons from the target atom due to the extra electrostatic force acting on the electrons. This shift in binding energy can be of the order of eV which is easily detectable in a photoemission experiment.

In this work photoemission spectroscopy has been used for identifying the elements present on a surface, to check that the surface is clean of contamination before deposition and to confirm that the molecules have been deposited. The results are also used to examine the chemical environments of the atoms in the adsorbed molecules. These data can be used to determine whether the molecule was deposited intact on the surface and to provide useful information on the adsorption geometry of the molecule on the surface. The efficiency of charge transfer is highly dependent upon the molecule's position relative to the surface and the chemical bonds attaching the molecule to the surface, so knowing the adsorption geometry is of great importance when studying

DSCs.

3.2.3 The photoemission process

Photoemission spectroscopy is based on the photoelectric effect,[59] in which a photon is absorbed causing the ejection of an electron from its host atom. The emitted electrons are called photoelectrons. On absorption the photon transfers its energy to the electron, if the amount of energy is high enough it allows the electron to overcome the binding energy and the work function of the surface so that the electron is no longer bound. Any remaining energy becomes kinetic energy which allows the electron to move through the vacuum. The kinetic energy of the electron (E_K) is given by Equation 3.2.1 below.

$$E_K = hv - E_B - \phi \tag{3.2.1}$$

The other terms in the equation are the energy of the absorbed photon (hv), the binding energy of the electron (E_B) and the work function of the surface (ϕ). The emitted electrons can be absorbed by a detector, in this process they gain energy equal to the work function of the detector. By knowing the work function of the detector, the kinetic energy of the electron and the incident photon energy. It is possible to calculate the binding energy of the electron to its host atom.

A schematic energy level diagram for the photoemission process and some of the processes which can occur afterwards is shown below in Figure 3.4. The molecule is initially in its ground state with all of its states below the Fermi level filled with electrons. An incident photon can be absorbed by the molecule causing the emission of a photoelectron. The probability of the photon being absorbed is dependent on several factors including the energy density in the final state; the magnitude and polarization of the photon's electric field vector; and the overlap between the initial and final electronic states of the molecule.

3.2.4 Relaxation processes

The emission of a photoelectron leaves a hole in the core or valence levels of the molecule, having a core-hole is an energetically unfavourable situation. The system can fill the core-hole by dropping a valence electron to fill the hole. The energy difference between the core and valence levels means that the transition increases the available energy of the system. The energy can be removed from the system by emission of another

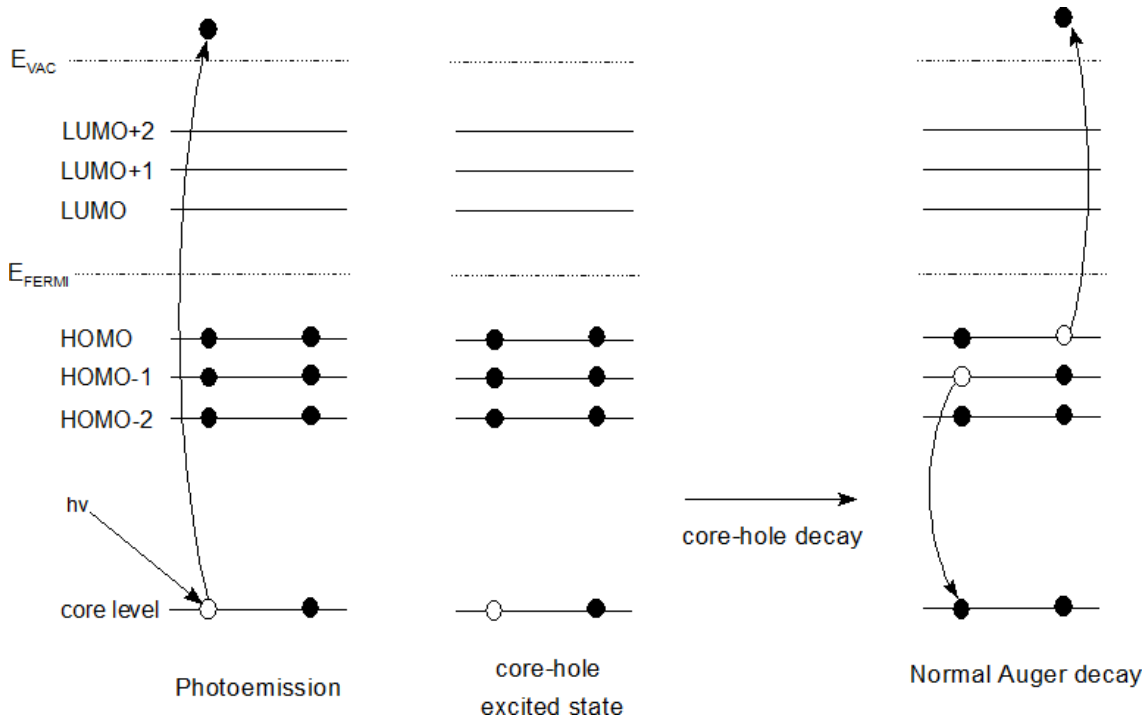

Figure 3.4: Schematic energy level diagram showing the photoemission and Auger decay processes for a molecule. An incident photon with enough energy to ionise the molecule is absorbed by the molecule and causes the emission of an electron. This leaves the molecule in an excited state with a core-hole. A valence electron will then fall to fill the core-hole which causes the ejection of either another electron (Auger decay) or a photon (fluorescent decay, not shown).

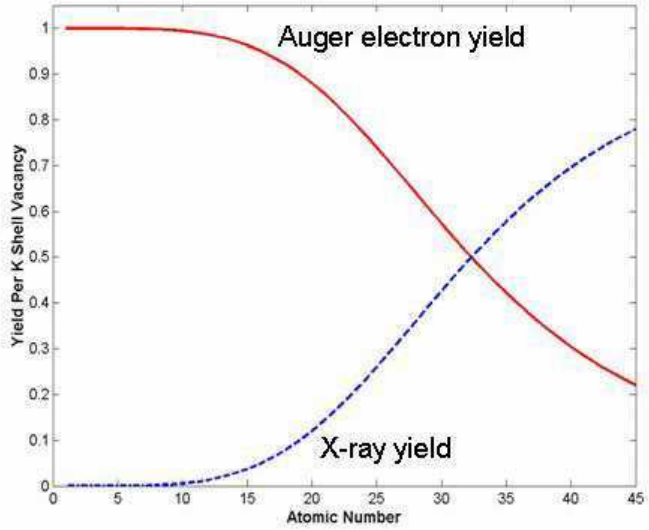

Figure 3.5: . Diagram showing relative yields of Auger and fluorescence decay processes as a function of atomic number. Figure adapted from Reference [60].

electron in a process called Auger decay or by emission of a photon which is termed fluorescent decay. The two processes are in competition with each other with Auger decay dominant for elements with low atomic mass and fluorescent decay prevailing for higher atomic mass elements. In this work the molecules studied were predominantly comprised of elements with low atomic mass. This makes Auger decay more suitable for studying these systems. A graph illustrating the probabilities of Auger and fluorescent decay as a function of atomic number is shown in Figure 3.5.

3.2.5 Loss processes

The emitted electrons can undergo interactions with their host atoms as they escape. This can affect their kinetic energy giving rise to additional features in a photoemission experiment. Only two interactions are resolvable in photoemission spectra as satellite peaks, other interactions cause inelastic scattering which will influence the background of the photoemission spectrum.

The two resolvable interactions are known as shake-up and shake-off processes and are depicted in Figure 3.6. Both processes are caused by the interaction of a valence electron with the original photoelectron as it leaves the molecule. The photoelectron can provide the valence electron with enough energy to either be excited into a higher energy unoccupied molecular orbital (shake-up) or to be ejected from the molecule (shake-off). As the original photoelectron has lost some of its kinetic energy in the interactions it appears as though the photoelectron has a higher binding energy. This

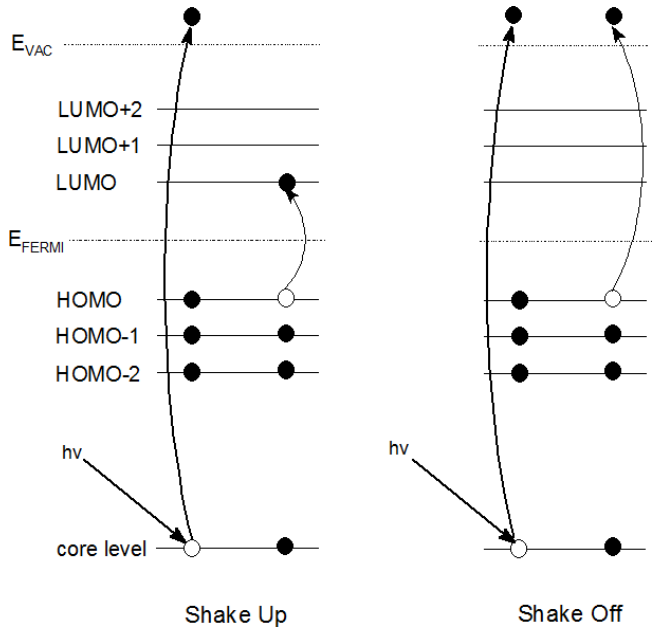

Figure 3.6: Schematic energy level diagram of potential energy loss processes during photoemission. The emitted electron can give some of its energy to valence electrons on its way out of the molecule. The shake-up process involves the excitation of a valence electron to an unoccupied molecular orbital, the shake-off process involves the ejection of a valence electron. These processes cause a reduction in the emitted electron's kinetic energy which increases its apparent binding energy.

creates a satellite feature at higher binding energy than the unaffected photoemission peak in a photoemission spectrum. These interactions are known as final state effects as the final state of the host atom has been changed by the interactions.

The loss processes involve the interaction of the emitted electron with the bulk as it travels through. The interactions that the electrons can undergo include the excitation of phonons and plasmons. These are quantisations of sound waves in matter and electron density oscillations around stationary positive ions respectively. Also once the electron has undergone an interaction it loses some of its kinetic energy and slows down, this makes it more susceptible to further inelastic processes. These electrons can no longer be used to identify the transition which produced them and form part of a background of secondary electrons.

3.2.6 l-s spin-orbit coupling

Electrons sharing an orbital interact with each other to conserve total angular momentum j. The total angular momentum is comprised of the orbital angular momentum l and the electron spin s, so that $j = l + s$. The properties l and s couple to ensure that

total angular momentum is conserved. After an electron is emitted from a core orbital the remaining electron can have either spin $s = 1/2$ or $s = -1/2$, this means the electron has a magnetic interaction with l. For levels with $l > 0$ i.e. p, d and f subshells which have l values of 1, 2 and 3 respectively, this interaction causes a splitting in the energy of the two possible final states. The emitted electron has two different possible binding energies depending on which final state the system is in. This spin-orbit splitting can be seen in photoemission spectra showing two peaks with slightly different binding energies.

For example spin-orbit coupling is seen in the S 2p spectrum, which has values of $l = 1$ and $s = \pm 1/2$. The total angular momentum $j = l + s = 1 \pm 1/2 = 3/2$ or $1/2$. The number of electrons in each j state is given by $2j + 1$, so the degeneracy of the $j = 1/2$ state is $2 \times 1/2 + 1 = 2$ and the $j = 3/2$ state has a degeneracy of $2 \times 3/2 + 1 = 4$. In a fully occupied p subshell with six electrons there would be two electrons with $j = 1/2$ and four electrons with $j = 3/2$. In this case spin-orbit splitting would produce two photoemission peaks with an intensity ratio of 1:2. The peak with the lower j value has the highest binding energy.

3.2.7 Elemental identification

Figure 3.7 shows an overview X-ray photoemission spectrum of the dye complex Ru 470 adsorbed on rutile TiO_2(110) taken using a photon energy of 620eV. This spectrum is low resolution showing the number of photoelectrons detected at each binding energy when the sample is illuminated with monochromatic light.

The background of the spectrum increases at higher binding energies and is caused by inelastically scattered electrons being detected. These electrons have lost kinetic energy increasing their apparent binding energies. The background rises sharply close to zero kinetic energy due to electrons undergoing multiple loss processes before leaving the surface.

Photoelectrons that leave the surface without losing kinetic energy produce narrow intense photoelectron peaks. Each element has different binding energies associated with it, meaning that the elements in a spectrum can be identified by comparing the peak binding energies with a reference table. In the overview spectrum the Ti 2p, 3s and 3p peaks come from the crystal, the O 1s, O 2s and valence band peaks come from both the crystal and the adsorbed dye molecules, and the N 1s, C 1s and Ru 3d peaks are solely due to the dye molecule.

The energy of the incident X-ray photons was 620 eV. When a photon is absorbed by

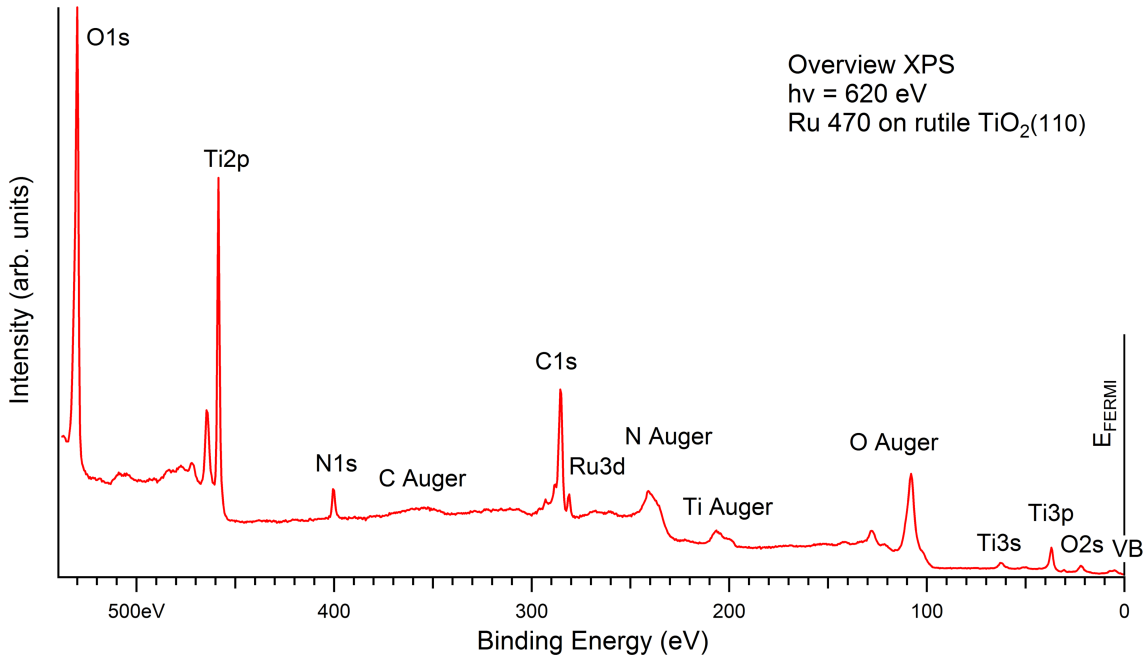

Figure 3.7: Overview X-ray Photoemission spectrum of Ru 470 adsorbed on rutile TiO_2(110) using a photon energy of 620 eV. The peaks have been labelled with the identity of electrons to show how photoemission spectroscopy provides information on the elements present in a sample.

the sample an electron gains the full 620 eV from the photon. This energy is used to overcome the binding energy of its original orbital and the work function of the surface. The remaining energy is used as kinetic energy which can be measured by the electron analyser. For example, an electron in an O 1s orbital which has an ionisation potential of 530 eV and excited using a photon energy of 620 eV would have a kinetic energy of 90 eV.

The photoemission process leaves the molecule in an excited state as shown in Figure 3.4. The core-hole relaxation process causes the emission of either an Auger electron or a photon as described in Section 3.2.4. The electron analyser is capable of detecting the Auger electrons and some example peaks can be seen in the overview spectrum in Figure 3.7. The peaks are broad and intense. Any photons emitted cannot be detected by the electron analyser and no peaks can be observed due to fluorescent decay. Unlike photoelectrons, Auger electrons are emitted with a fixed kinetic energy which is independent of the exciting photon energy. The energy of the Auger electron is determined solely by the energy difference between the orbitals involved in the core hole decay. Changing the photon energy and repeating the overview spectrum would cause a shift in the apparent binding energy of the Auger electrons as the kinetic energy is constant but the photon energy has changed.

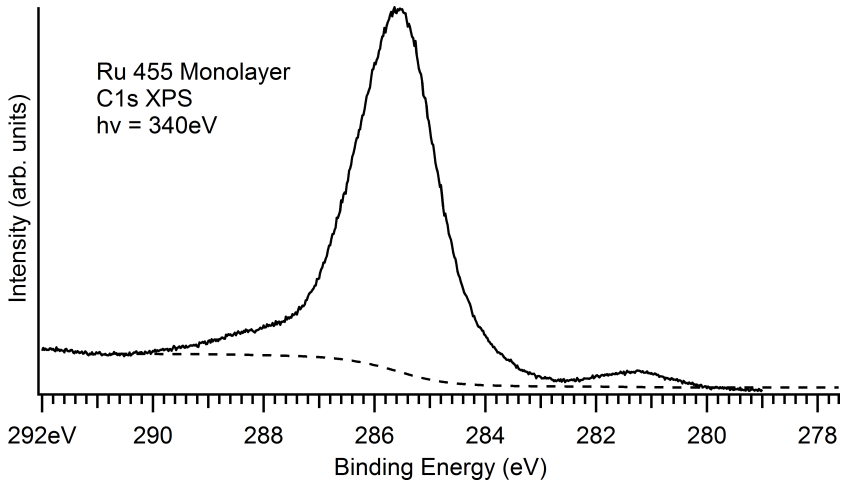

Figure 3.8: High resolution C 1s X-ray photoemission spectrum of a monolayer of Ru 455 on rutile TiO_2(110) using hv = 340 eV. The Shirley background is also shown, this is calculated iteratively using the intensity of the peak as described in the main text.

3.2.8 Chemical bonding

Figure 3.8 shows a high-resolution core-level photoemission spectrum of a monolayer of Ru 455 dye complex on rutile TiO_2(110). The diagram is shown as an example of a spectrum that can be used to obtain information on the chemical states present within the sample. To obtain the spectrum the kinetic energy detected by the analyser is changed in small increments and the number of detected electrons recorded for each step. In this spectrum there are two resolvable peaks and a shoulder on the dominant peak which can be assigned to C 1s or Ru 3d levels based upon their binding energies. More specific assignments can be accomplished by comparing the intensity of the peaks to the stoichiometry of the molecule on the surface. The peaks could be photoemission, Auger, shake-up or shake-off peaks. In this case the peaks are all due to photoemission and show the different chemical bonding states of carbon and ruthenium atoms.

In Figure 3.8 the background level is more intense at the high binding energy side of the dominant peak. Passing the threshold for excitation increases the number of electrons that can be inelastically scattered shifting them to higher binding energies and increasing the background intensity. This background needs to be removed using analysis software before attempting to curve fit the peaks. Shirley backgrounds are often used in this work.[61] The background is calculated iteratively and its intensity at a given point is proportional to the area of the spectrum from that point to lower binding energy as seen in Figure 3.8. The shape of each peak is a combination of Lorentzian and Gaussian peak shapes. The Gaussian component is due to instrument broadening of both the energy of the incident photons and the kinetic energies of the electrons in

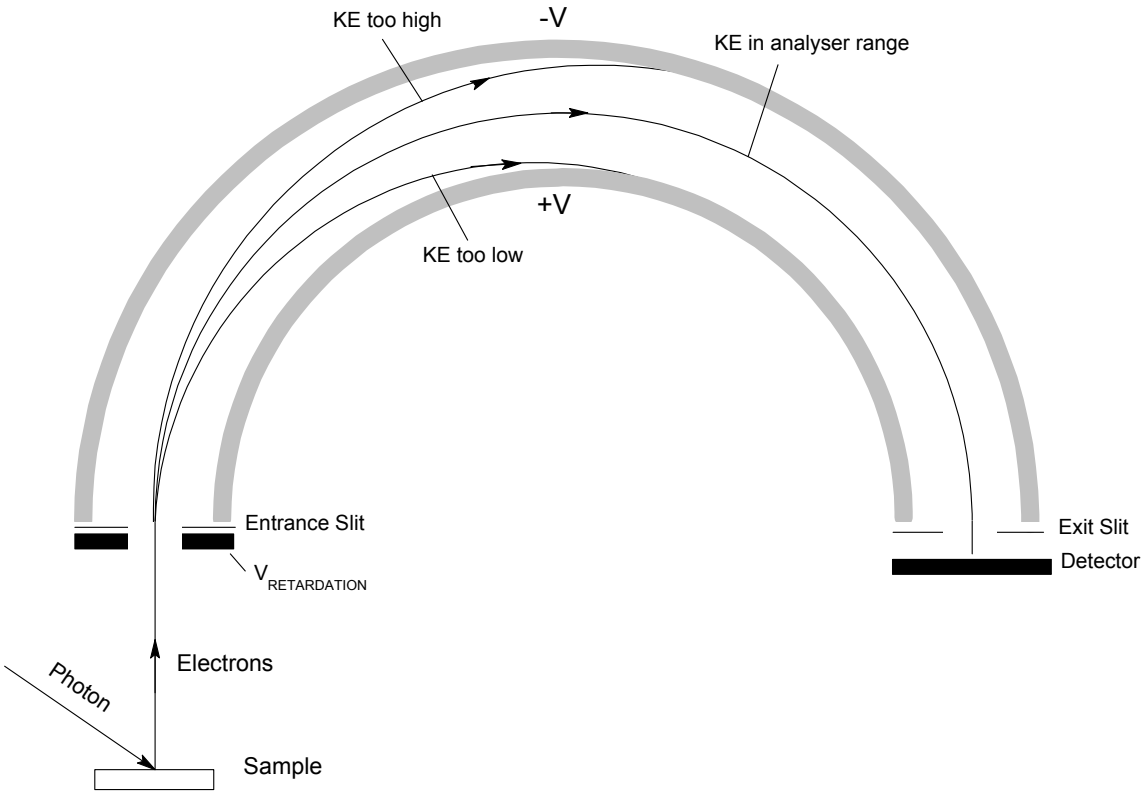

Figure 3.9: Schematic diagram of a concentric hemisphere analyser (CHA) used to determine kinetic energy of electrons emitted from a sample

the analyser. The Lorentzian component is caused by the states being broadened by the uncertainty principle $\Delta E \Delta \tau \leq \hbar/2$. The photoemission peaks are fitted using Voigt functions which are convolutions of Gaussian and Lorentzian functions.

3.2.9 Data acquisition

To obtain photoemission spectra a detector is needed that is capable of determining the kinetic energies of electrons emitted from the sample. A concentric hemisphere analyser (CHA) can be used to measure the kinetic energy of electrons. A schematic diagram of a CHA is shown in Figure 3.9, a photograph of a CHA used in preliminary experiments for this work is shown in Figure 3.10.

The electrons emitted from the sample have a wide range of kinetic energies due to the varied elements and chemical environments present on a typical surface. The electron analyser selects only electrons with kinetic energy within a specified range. After emission from the sample the electrons travel through the vacuum to a mesh held at a retardation voltage. This potential changes the kinetic energy of the electrons to values more suitable for the analyser's settings. After passing through the mesh the electrons then pass through an adjustable entrance slit. This can be used to increase the reso-

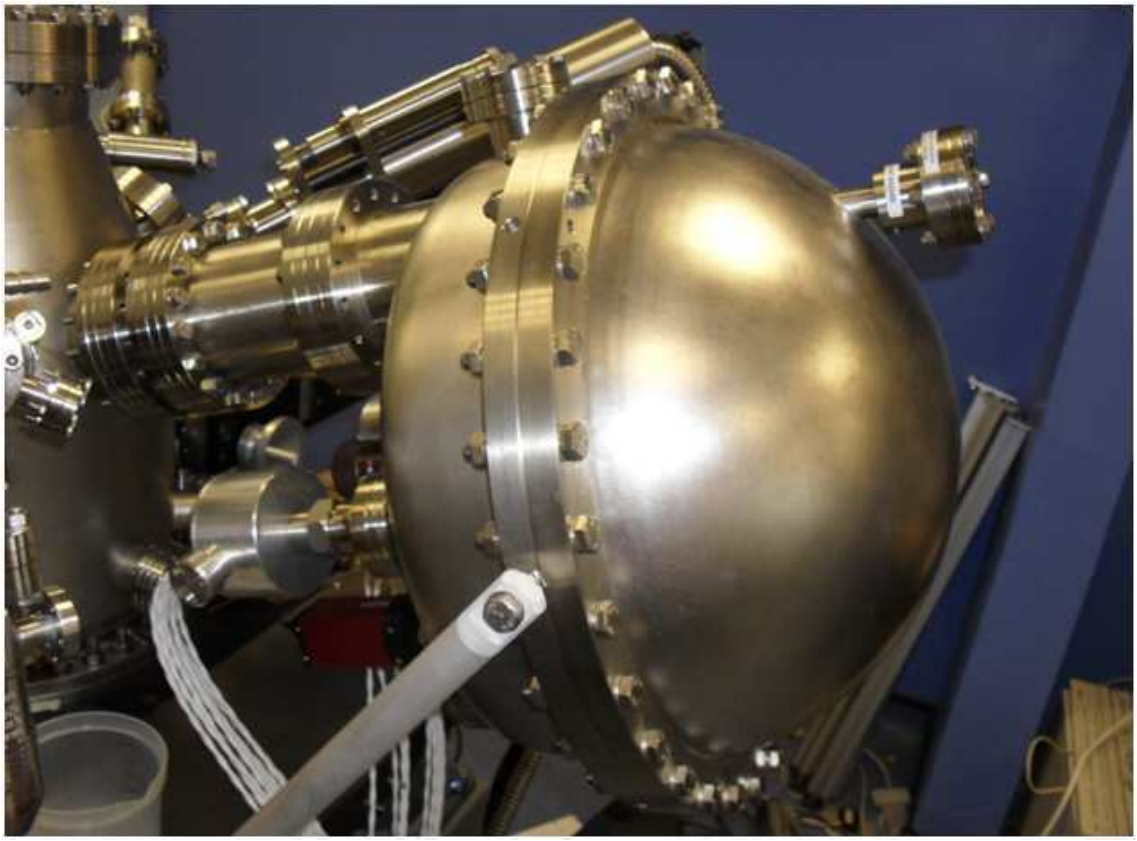

Figure 3.10: Photograph of a Scienta R3000 electron analyser mounted on a vacuum chamber.

lution of the analyser at the expense of the intensity of the signal. The entrance slit prevents electrons from entering the analyser with unusual trajectories which may be detected even if they have the “wrong" kinetic energy. Inside the analyser there are two hemispherical metal plates with potentials applied to them. The inner hemisphere is positive with respect to the outer plate.

The electric field generated by the plates causes the trajectory of the electrons to bend towards the inner plate as they pass through the analyser. The amount of curvature induced in the electrons path is dependent on the kinetic energy of the electrons and the strength of the electric field. If the kinetic energy of an electron is below the current range of the analyser then the electron’s path will turn too sharply towards the inner plate and it will be neutralised at the plate’s surface. If the kinetic energy of an electron is above the current analyser settings then the electron’s path will not curve enough to avoid the outer plate and the electron will be neutralised at the outer plate’s surface. This means that the electrons are spread out spatially depending on their kinetic energy and that only electrons with the correct kinetic energy can make it around the curved section of the analyser.

The electric field between the plates can be adjusted to change the spread of electrons by altering the potential applied to the plates. The kinetic energy range of the electrons allowed to pass through the analyser is called the pass energy, which can be set to values from 10 to 100 eV. The higher the pass energy the more electrons make it through the analyser but the resolution is lowered due to the greater range of kinetic energies that are allowed to reach the detector.

After passing through the hemispherical plates the electrons travel through an exit slit which allows only electrons with a trajectory passing through the opening of the slit to reach the detector. After passing through the slit the electrons are detected using a multi-channel plate detector. This is a 2D grid of electron multipliers, a single electron incident on a multiplier causes a cascade of electrons to be released. Beyond the electron multipliers is a phosphorescent screen, if a cascade of electrons hits the screen it causes a spot to phosphoresce. A camera is used to monitor the phosphorescent screen, a computer reads the images from the camera and records the positions of the phosphorescence events. The positions of the events are a function of the initial electrons’ kinetic energies. The events are recorded and accumulated to produce a spectrum consisting of the number of electrons detected as a function of kinetic energy.

If the voltage settings are not changed during data acquisition then the analyser is said to be in fixed mode, the kinetic energy range measured by the analyser in this mode is determined by the pass energy. Usually the analyser is operated in swept mode

where the retardation voltage is incremented throughout the scan so that the kinetic energy of the electrons that enter the analyser is changed at each increment. This mode has several advantages over fixed mode as the measurable kinetic energy range is no longer limited by the pass energy; the resolution is not dependent on the kinetic energy range; and any non-uniform sensitivity in the phosphorescent screen is averaged out.

The analyser software can display the detected electrons as a function of approximate binding energy instead of kinetic energy using Equation 3.2.2 below, this allows for easier interpretation of results.

$$E_{B(Uncalibrated)} = h\upsilon - E_K \tag{3.2.2}$$

This equation puts the spectrum on a binding energy scale. However, the binding energies in the spectrum are unlikely to be the true binding energies of the electrons. This is because there may be a difference between the requested photon energy and the actual photon energy. In addition, the work function of the analyser is unknown. The spectrum can be calibrated using a known feature such as the Fermi level of a metal at 0 eV or a known feature in the spectrum such as the O 1s peak of TiO_2. The Fermi level can be found for a semiconductor by taking a spectrum of the sample holder, the Fermi levels can be assumed to be aligned due to the contact between the sample and the sample holder. It is also possible to reference the binding energy to the vacuum level. Figure 3.11 shows the steps used to change a kinetic energy spectrum to a calibrated binding energy spectrum.

3.2.10 Surface sensitivity

The surface of the substrate and the dye molecules adsorbed onto it are crucial to the efficiency of DSC devices. The bulk of the sample is of comparatively limited relevance. Therefore it is necessary to maximise the signal obtained from the surface region of the sample whilst minimising the signal from the sample bulk. The major factor influencing the surface sensitivity is the kinetic energy of the emitted electrons.

An electron travelling through a solid can be inelastically scattered thus lowering the electron's kinetic energy. These electrons can no longer provide any information on the transition that emitted the electrons and form part of the background as secondary electrons. Electrons emitted near the surface have only a short distance to travel before leaving the surface so they are less likely to be affected by inelastic scattering. A short inelastic scattering distance is useful as electrons from the bulk are more likely than electrons from the surface to undergo scattering before leaving the surface and

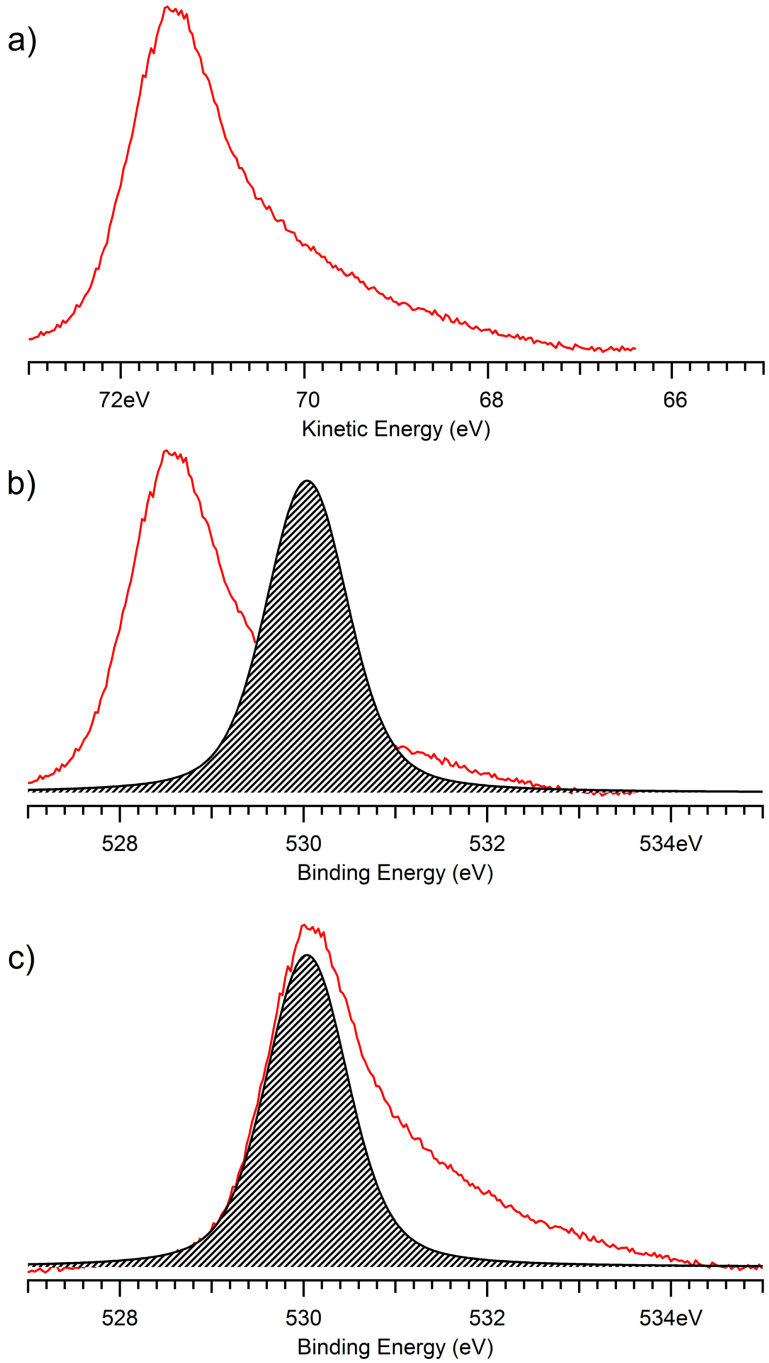

Figure 3.11: Diagram showing the steps taken to produce a calibrated photoemission spectrum on a binding energy axis. The example uses an O 1s photoemission spectrum of a monolayer of N3 on rutile TiO_2(110) using hv = 600 eV (red line). a) shows the experimental spectrum as recorded on a kinetic energy scale. Equation 3.2.2 is used to place the spectrum on a binding energy scale as shown in b). b) also shows the position of the TiO_2 O 1s peak at 530.05 eV. In c) the experimental spectrum has been shifted so that the experimental O 1s peak assigned to TiO_2 is at the correct binding energy.

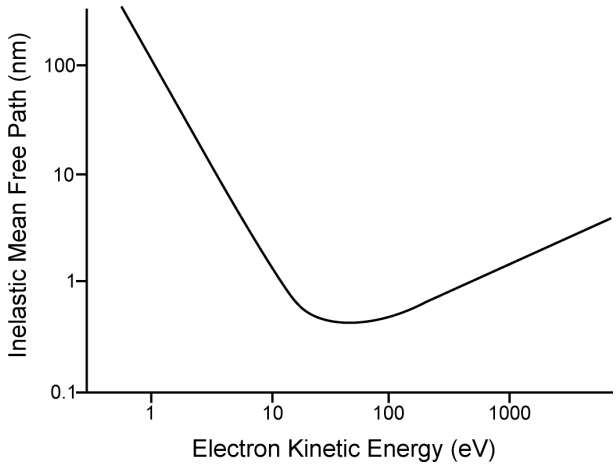

Figure 3.12: Universal curve showing the inelastic mean free path of an electron in a solid as a function of its kinetic energy. Figure adapted from Reference [62]

form part of the background. The inelastic mean free path λ(E) is a measure of how far an electron travels on average before losing energy, this quantity is defined by the equation.

$$I(d) = I_0 exp^{-d/\lambda(E)} \tag{3.2.3}$$

where *I(d)* is the intensity of the electron beam after travelling a distance d through a material, I_0 is the original intensity of the beam. The inelastic mean free path is defined as the distance the electron beam travels through the material before its intensity is reduced to 1/e (~0.37) of its initial intensity. The mean free path of electrons is primarily affected by the kinetic energy of the electrons. The relationship between the mean free path and the kinetic energy of the electrons is described by the empirically found universal curve shown below in Figure 3.12.

The shortest mean free path for the electrons in a medium is given by the minimum on the graph, this is in the kinetic energy range of 40-100 eV. At higher kinetic energies the electron travels through the sample quicker giving it less chance to interact, this causes an increase in the inelastic mean free path of the electrons. At lower kinetic energies the inelastic mean free path is increased as the electrons do not have as much energy to excite loss processes in the solid. For surface science experiments the kinetic energy of the electrons should be approximately 50 eV. By setting the exciting photon energy approximately 50 eV higher than the binding energy of the orbitals being studied it is possible to increase the probability electrons in the bulk will undergo scattering before reaching the detector.

3.3 Near-edge X-ray absorption fine structure spectroscopy

Photoemission spectroscopy has been used in this work to examine the occupied electronic states of an adsorbed molecule on a substrate as described in Section 3.2. In order to observe the unoccupied electronic states of the samples in this work near-edge X-ray absorption fine structure (NEXAFS) spectroscopy has been used. In photoemission spectroscopy the electrons simply need to be ejected from their original orbitals using X-ray photons and the spectra are obtained by measuring the emitted electrons kinetic energy. To measure a NEXAFS spectrum, electrons are initially excited to the unoccupied molecular orbitals of interest, the excited state then relaxes which emits a detectable particle such as an electron or photon.

Initially the adsorbed molecules are in the ground state with no electrons in the unoccupied molecular levels. In order to study the unoccupied states electrons need to be excited to these unoccupied levels from a well-defined core level. To reach these unoccupied levels an electron must be provided with enough energy to reach the unoccupied levels above the Fermi level but not enough to cause the ejection of the electron from the molecule. A schematic energy level diagram illustrating the excitation and election ejection processes used in NEXAFS spectroscopy is shown in Figure 3.13.

After an electron has been transferred to an unoccupied level the molecule is in a unstable excited state, this state can then decay to a more stable state by filling the core-hole with an electron from a higher energy level. The energy released by filling the core-hole is then used to eject either a photon or an electron from the molecule. The photon ejection process is slightly different from the photoemission process due to the presence of an extra election which changes the kinetic energy of the emitted particles. There are two types of electron ejection depending on whether the originally excited electron is involved in the decay process. Participator decay involves the original excited electron whilst spectator decay does not. The difference is important for studying the charge transfer process as described in Chapter 4.

In NEXAFS spectroscopy electrons are mostly emitted when the energy of the incident photons is exactly the same as the energy gap between the core level and the unoccupied level, this is known as being on resonance. When the energies of the photon and the energy gap are different no photoexcitation occurs and therefore no Auger electrons can be emitted.

To acquire a NEXAFS spectrum the sample is first illuminated using a photon energy that is slightly lower than that needed to excite an electron into the LUMO of the molecule. As this photon energy is not on the resonance condition no photoexcita-

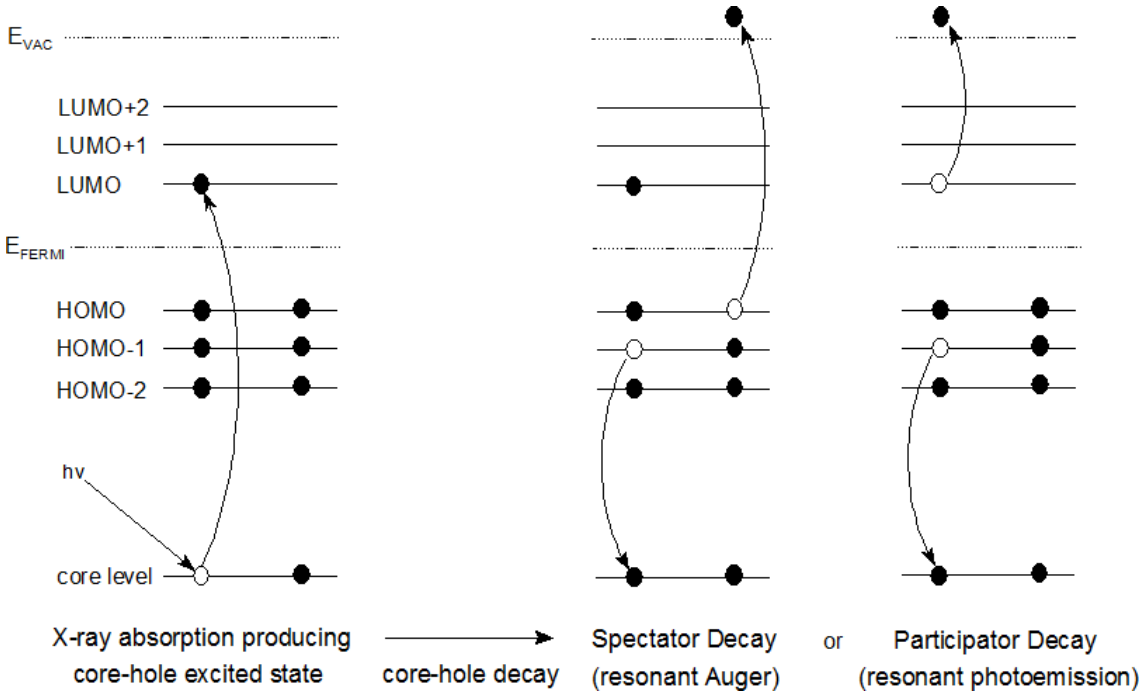

Figure 3.13: Schematic energy level diagram showing the creation of a core-hole excited state by absorption of a photon with the exact energy needed to excite an electron to an unoccupied level. The core-hole decay process involves an electron dropping to fill the core hole which causes the ejection of either an electron or a photon (not shown). There are two possible electron ejection processes which can occur: spectator decay which does not involve the originally excited electron, and participator decay which ejects this excited electron.

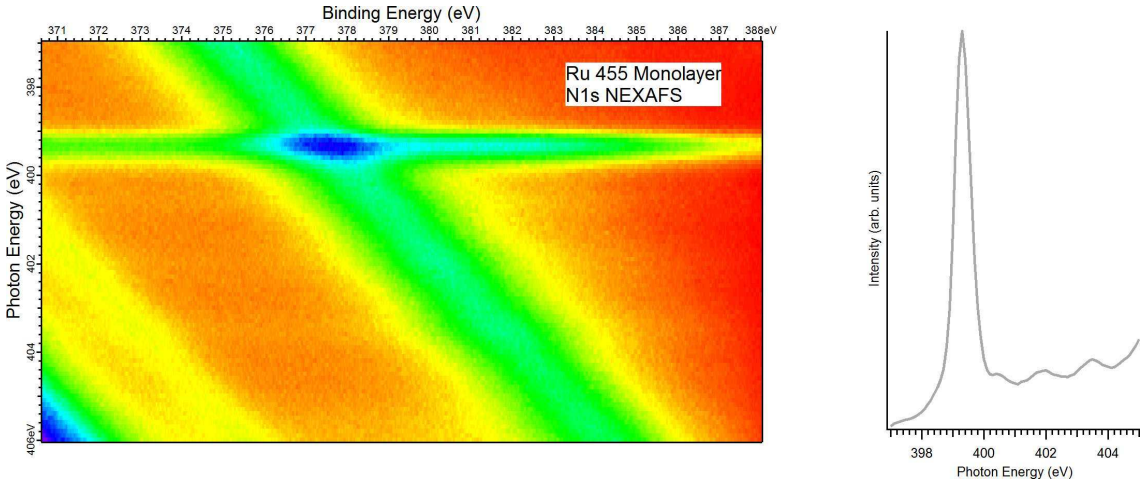

Figure 3.14: An example of a NEXAFS spectrum taken of a monolayer of Ru 455 molecules adsorbed on rutile TiO_2(110). An integrated spectrum showing the number of emitted electrons for each photon energy is shown on the right.

tion to the LUMO can occur. The photon energy is then increased. Once the resonance condition is achieved a core level electron can be excited into an unoccupied orbital. After excitation a core-hole is created leaving the system in an unstable state, decay processes can then occur which lead to the emission of detectable electrons. In NEXAFS spectroscopy it is not necessary to measure the energy of the emitted electrons, only the number of electrons emitted at each photon energy. An example of a NEXAFS spectrum is shown below in Figure 3.14.

Electrons can be collected using a partial yield detector. This type of detector counts electrons of all kinetic energies except for secondary electrons which are excluded using a retardation plate held at a positive potential. It is also possible to acquire a NEXAFS spectrum by measuring the current on the sample, this current is created by the large number of electrons being emitted from the sample. In this work an electron analyser was used to take NEXAFS spectra by measuring the number of electrons detected as well as the kinetic energy of the emitted electrons. This provides additional information on the kinetic energy distribution of the electrons and can be used to detect photoemission peaks which may drift into the data. The electron kinetic energy window can be confined to a specific region. The different regions correspond to 'Auger yield' where Auger electrons associated with a certain core level are collected or 'secondary electron yield' which counts background secondary electrons. On resonance, more background secondary electrons are produced which allows NEXAFS spectra to be measured using these electrons.

3.4 Density Functional Theory

In order to interpret some of the experimental data obtained in this work computer simulations were used to model some of the systems being studied. Density functional theory (DFT) was used to provide additional information on the molecular orbitals and adsorption geometries of the molecules studied in this work.

DFT is a modelling technique using quantum mechanics to predict observable quantities such as the positions of atoms in a molecule, the results of these calculations should always be compared to experimental data to ensure that the results are reliable. DFT can be used to find the geometry of a molecule by changing the positions of the atoms until the lowest energy configuration is found. The bonding geometry of a molecule on a surface can be calculated using the same method but due to the larger number of atoms and potential interactions the calculations become more intensive and take longer to perform.

DFT calculations also produce information on the electronic orbitals within the molecule such as their spatial and energetic distribution. Figure 3.15 shows the calculated structure and distribution of the HOMO of a Ru 455 molecule after geometry optimisation, these calculations are performed on an isolated molecule in vacuum using the DFT software Dmol^3.[63, 64]. The results of this software are stored in a text file and converted to a visual format using Materials Visualizer which is part of the Materials Studio software package.

If DFT were to completely accurately model a system using full quantum mechanics then it would be impossible to study a system of more than a few atoms as the amount of computer power and time needed to complete the simulation would be currently unrealistic. In order to study larger and more relevant systems in a reasonable timeframe approximations have to be made to the theory. By choosing the approximations carefully it should be possible to reduce the computational load of a simulation without significantly affecting the results.

DFT is used in this work to support experimental data, only a brief overview will be given here. The reader is directed to Capelle[65] for a more thorough description if required.

The starting point for DFT is the time-independent Schrödinger equation which describes an electron moving in a potential $v(\mathbf{r})$.

$$\left[-\frac{\hbar^2\nabla^2}{2m} + v(\mathbf{r})\right]\psi(\mathbf{r}) = \epsilon\psi(\mathbf{r}) \tag{3.4.1}$$

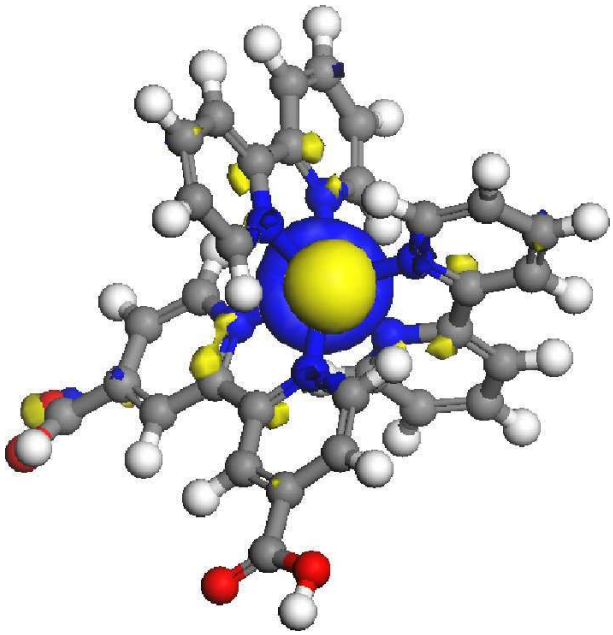

Figure 3.15: Geometry optimised free Ru 455 molecule with the calculated HOMO shown in blue and yellow, this was generated using Dmol[3] in Materials Studio.[63, 64]

$-\hbar^2\nabla^2/2m$ is the kinetic energy operator and $v(\mathbf{r})$ is the potential energy operator, these act on the wavefunction $\psi(\mathbf{r})$ of a single electron. The total energy of the electron is ϵ which is the sum of the kinetic and potential energy of the electron.

Electrons in atomic systems also interact with the nucleus which has its own kinetic and potential energy. As the nucleus has a mass several orders of magnitude higher than an electron it moves at a much slower rate, this leads to the Born-Oppenheimer approximation where the kinetic energy of the nucleus is treated as negligible. The nuclear potential energy can be treated as part of the potential $v(\mathbf{r})$ acting upon the electron.

As extra electrons are added to the system the complexity increases due to an additional energy term caused by the interactions between the electrons. Schrödinger's equation becomes:

$$\left[\sum_{i}^{N}\left(-\frac{\hbar^2\nabla_i^2}{2m}+v(\mathbf{r}_i)\right)+\sum_{i<j}U(\mathbf{r}_i,\mathbf{r}_j)\right]\psi(\mathbf{r}_1,\mathbf{r}_2...,\mathbf{r}_N)=\epsilon\psi(\mathbf{r}_1,\mathbf{r}_2...,\mathbf{r}_N) \tag{3.4.2}$$

where N is the number of electrons and $U(\mathbf{r}_i,\mathbf{r}_j)$ is the interaction between electrons. This equation can be simplified by using operators:

$$\left[\sum_{i}^{N}(\hat{T}+\hat{V})+\sum_{i<j}\hat{U}\right]\psi(\mathbf{r}_1,\mathbf{r}_2...,\mathbf{r}_N)=\epsilon\psi(\mathbf{r}_1,\mathbf{r}_2...,\mathbf{r}_N) \tag{3.4.3}$$

where for a Coulombic potential and non-relativistic atomic system.

$$\hat{T} = -\frac{\hbar^2}{2m}\sum_i \nabla_i^2, \tag{3.4.4}$$

$$\hat{U} = \sum_{i<j} U(\mathbf{r}_i, \mathbf{r}_j) = \sum_{i<j} \frac{q^2}{|\mathbf{r}_i - \mathbf{r}_j|} \tag{3.4.5}$$

$$\hat{V} = \sum_i v(\mathbf{r}_i) = \sum_i \frac{Qq}{|\mathbf{r}_i - \mathbf{R}|} \tag{3.4.6}$$

where q and $\mathbf{r}$ are the electronic charge and positions and Q and $\mathbf{R}$ are the nuclear charge and positions respectively.

Both $\hat{T}$ and $\hat{U}$ can be used for any non-relativistic atomic system with a Coulombic potential, $\hat{U}$ is dependent upon the position of the nuclei. When solving the Schrödinger equation the external potential $v(\mathbf{r})$ is specified to represent the system, this can be used to find the wavefunction $\Psi(\mathbf{r})$ and then to calculate observable information by taking expectation values of the operators.

One very useful observable that can be calculated is the electron density,

$$n(\boldsymbol{r}) = N\int d^3\mathbf{r}_2 \int d^3\mathbf{r}_3 ... \int d^3\mathbf{r}_N \psi^*(\mathbf{r}, \mathbf{r}_2 ..., \mathbf{r}_N)\psi(\mathbf{r}, \mathbf{r}_2 ..., \mathbf{r}_N) \tag{3.4.7}$$

In Schrödinger's equation one of the most important variables is the electron position $\mathbf{r}$. This variable can be replaced with the density of the electrons $n(\mathbf{r})$. In this case the operators are now functions of the electron density which is itself a function of the electrons positions. This is also described as a functional. These approximations allow for simulations to be run on systems with many nuclei and electrons in a reasonable timeframe allowing for the study of molecules and surfaces.

There are a lot of types of DFT simulations for different applications. The accuracy of the simulation can be adjusted to make the results more accurate or to make the simulations easier to run. In this work Dmol^3 is used to model the dye complexes studied in experimental work. When modelling the dye complexes adsorbed on surfaces periodic boundary conditions need to be used, this effectively makes the surface extend to infinity and prevents the surface from distorting due to the edge atoms not being fully connected as in a real surface. Bloch waves are utilised in the calculations which use a cell-periodic factor and phase factor to make the wavefunctions periodic.

CHAPTER 4

Molecule to substrate charge transfer

4.1 Introduction

DSCs rely on electron transfer from an adsorbed molecule to the surface of the substrate. This chapter describes the experimental techniques used in this work to study the transfer of electrons. The systems studied in this work are models of sections of a multi-centre water-splitting DSC.

- The commercially available single centre dye complexes N3, Ru 455 and Ru 470 adsorbed onto a rutile TiO_2(110) surface were used to study molecule to substrate charge transfer. The N3 dye complex is currently one of the most efficient dyes used in photovoltaic DSC devices.[7] Ru 455 and Ru 470 have similar chemical structures to N3 but with different ligands. All of these dye complexes have a bi-isonicotinic acid ligand which is known to effectively bond a dye complex onto a TiO_2 surface. By comparing the charge transfer timescales of the three dye complexes it should be possible to determine how changes in the dye complex structure affect the charge transfer process.

- The dipyrrin-based complexes PY1 and PY2 adsorbed onto a rutile TiO_2(110) surface were used to study molecule to substrate charge transfer. The two dye complexes do not contain a bi-isonicotinic acid dye complex and instead bind to the surface through dipyrrin-based ligands. By comparing the charge transfer timescales for dipyrrin-based complexes with bi-isonicotinic acid based complexes we may get some information on how the bonding ligand affects the efficiency of the charge transfer process.

- A single centre water-splitting dye complex adsorbed onto a rutile TiO_2(110) surface was used to study the dynamics behind the water-splitting process. The efficiency of a single centre water-splitting DSC should be closely related to the efficiency of charge transfer from the dye to the surface. This system could be also used as a simplified model of a multi-centre water-splitting complex, this model could provide vital insights into the water-splitting reaction and could be used to help interpret future results from the multi-centre dye complex.

In the previous chapter the experimental and theoretical techniques used to investigate the adsorption of molecules to surfaces were described. The results from these techniques are also important to the transfer of electrons between the molecule and the surface. In addition to the spatial distribution of the electrons in the system it is useful to know the electronic energy levels and the timescale of charge transfer from an excited dye molecule to the substrate.

In a DSC device a photon of visible light can cause the excitation of an electron from the dye molecule's valence levels to an unoccupied level. It is then possible for this excited electron to transfer into the conduction band of the substrate. The valence band has a high density of states so there are many possible transitions to the unoccupied levels for a valence excited system. By exciting an electron from a single core level we can reduce the range of possible transitions for the system making it easier to study. It is expected that charge transfer from core-excited and valence-excited systems will be similar, as previous results have shown the core and valence excitons have similar distributions to each other.[66]

In order to excite an electron from the core level to a previously unoccupied level an x-ray photon needs to be absorbed by the molecule. This absorption is most likely to occur, when the energy of the photon matches the energy difference between the molecules energy levels. When this condition is satisfied the system is referred to as being on-resonance. The experimental techniques detailed in this chapter can be described as resonant spectroscopy techniques due to this condition.

After excitation with an x-ray photon the molecule is in a core-excited state. This is energetically unfavourable and the molecule will decay after a short time period. In this short time it is possible for the excited electron to be transferred to the substrate. This changes the possible decay paths of the molecule's excited state. The decay paths emit either electrons or photons from the molecule to conserve energy. By detecting these particles and calculating their energies we can determine whether the originally excited electron was still present when the decay event occurred. In the model DSC devices studied here if the electron was no longer present at the decay event then it is

likely that the electron has been transferred into the substrate which is also called electron injection. It is also possible that the electron could be transferred to neighbouring molecules or an alternative ligand on the same molecule.

The lifetime of a core-hole is of the order of a few femtoseconds. This allows us to measure charge transfer timescales on the femtosecond timescale. Charge transfer is effectively in competition with some specific core-hole decay pathways. If charge transfer occurs efficiently then the number of electrons emitted from these decay paths is significantly decreased. By analysing the number and energies of the emitted particles it is possible to quantify the timescale of charge transfer from unoccupied molecular orbitals to the substrate.

This chapter will describe the experimental techniques used to analyse the unoccupied molecular orbitals of the model DSCs that we studied. Energy level alignment diagrams can be produced showing occupied and unoccupied orbitals of a dye molecule on a common binding energy scale. This is needed to see where these orbitals are with relation to the substrate energy levels. This allows us to see which orbitals will be capable of charge transfer in both valence and core-excited molecules. Resonant electron spectroscopy is also described which provides the energies of electrons emitted by various core-hole decay processes. The results from this spectroscopy can be used in the core-hole clock method which can provide an estimate of the charge transfer timescale on the femtosecond timescale.

4.2 Energy level alignment

To study the charge transfer process in detail it is useful to know which molecular orbitals are capable of charge transfer. In this work the semiconductor substrate TiO_2 is studied extensively. In theory semiconductors have no states in the band gap between the conduction and valence bands and the valence band contains only filled states. In practice the semiconductor will have impurities, defects and surface states, these will lead to some states lying in the band gap and the valence band may not be completely filled. However, the vast majority of the density of available states will be in the conduction band. In a solar cell device we typically only consider the conduction band region is suitable for accepting electrons. For successful charge transfer to occur the unoccupied molecular orbitals of the dye complex should overlap energetically with the conduction band of the substrate.

An energy level alignment diagram is shown in Figure 4.1a). This diagram incorporates photoemission spectra of a clean surface and the same surface with a monolayer of

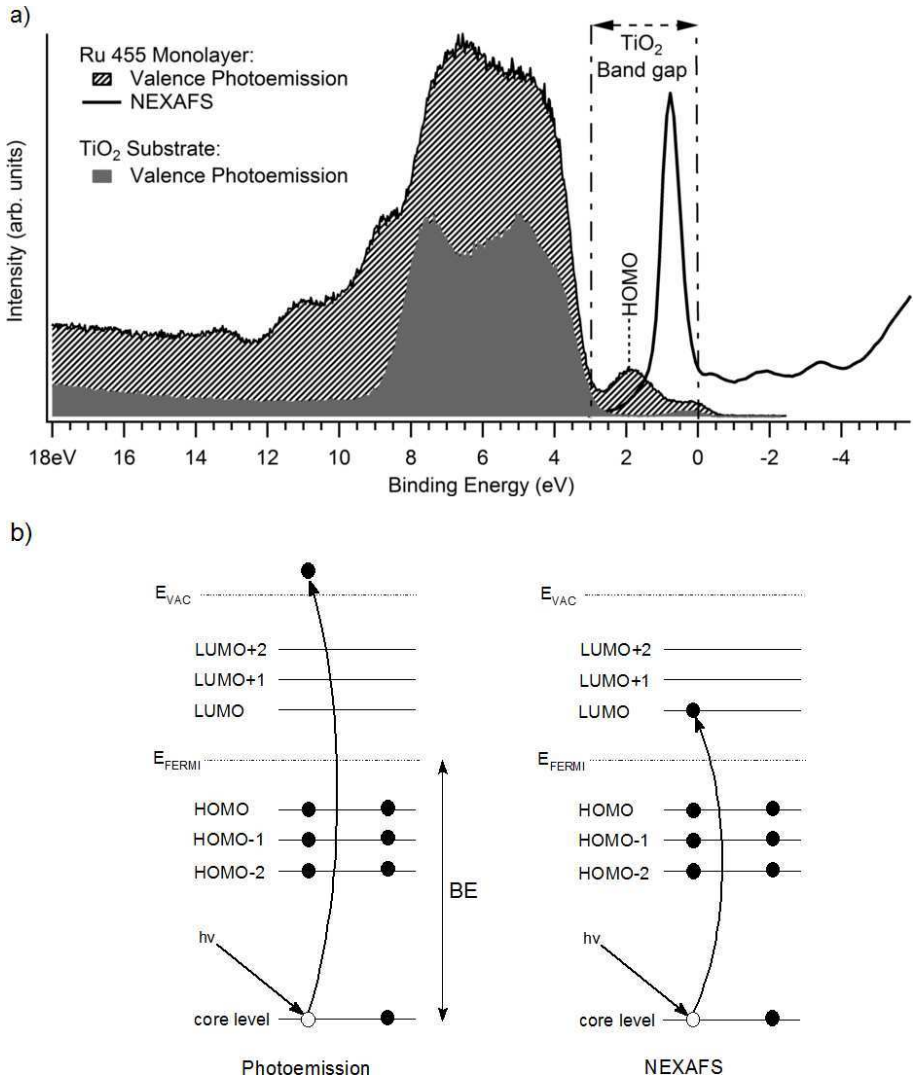

Figure 4.1: Part a) shows an energy level alignment diagram for a monolayer of Ru 455 on TiO_2. This diagram primarily consists of a valence band XPS spectrum and a NEXAFS spectrum converted to a binding energy scale. The diagram also includes a valence band XPS spectra of a clean TiO_2 surface and the band gap of the TiO_2 substrate.[16] Part b) shows electronic energy level diagrams for photoemission and NEXAFS processes to show the relationship between the two types of spectra.

adsorbed molecules. These spectra show the occupied levels of the substrate and the molecules respectively as described in Section 3.2. The diagram is also composed of a NEXAFS spectrum of the surface with a monolayer of adsorbed molecules, which shows the unoccupied levels of the system as described in Section 3.3.

For semiconductors the optical band gap can be found through absorbance studies. In these studies the absorbance of the sample is measured as the photon energy is increased. The optical band gap is the energy of the absorption band edge. The optical band gap can have a different value to the electronic band gap. This is because photon absorption creates electron-hole pairs that are bound together whilst an electronic transition creates an unbound electron-hole pair. The binding energy of the electron-hole pair can cause a difference between the optical and electronic band gaps. The difference is marginal for the inorganic titanium dioxide crystals that are used here.

The substrate conduction band is at higher energy than the band gap and it is in this range where charge transfer is energetically possible. Before combining all of the spectra it is necessary to change the NEXAFS spectrum from a photon energy scale to a binding energy scale so that all of the spectra can be aligned on a common axis to show both occupied and unoccupied states.[67]

Figure 4.1b) shows schematic energy level diagrams of the NEXAFS and photoemission processes with the exciting photon energy and binding energies marked on the relevant diagrams. Figure 4.2 is included to help show how to change a NEXAFS spectrum from a photon energy scale to a binding energy scale. In a NEXAFS spectrum the unoccupied levels are initially measured relative to the core level, to make them relative to the Fermi level the binding energy of the core-level must be taken into account. The method used in this work for changing the scale of NEXAFS spectra is described below.

The binding energy of any point on the NEXAFS spectrum is defined as -Δ relative to the binding energy of the core hole.

$$BE_{\text{NEXAFS}} = -\Delta \text{ relative to } BE_{\text{core-hole}} \tag{4.2.1}$$

The binding energy of the core hole is then calibrated relative to the Fermi level at 0 eV.

$$BE_{\text{core-hole}} = BE_{\text{core-hole}} \text{ relative to Fermi level} \tag{4.2.2}$$

Equation 4.2.3 is obtained by combining equations 4.2.1 and 4.2.2.

$$BE_{\text{NEXAFS}} = (-\Delta + BE_{\text{core-hole}}) \text{ relative to Fermi level} \tag{4.2.3}$$

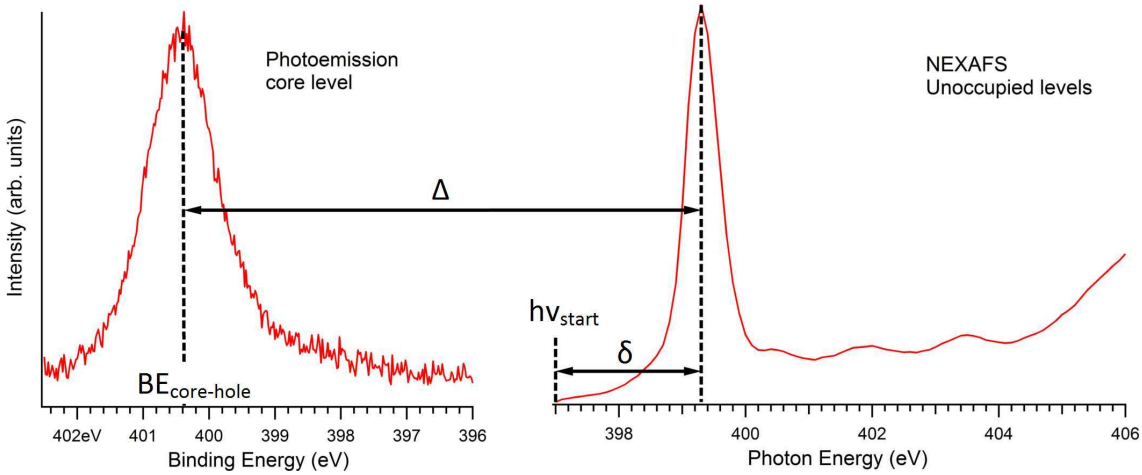

Figure 4.2: This figure illustrates the terms involved in changing a NEXAFS spectrum from a photon energy scale to a binding energy scale

The -Δ in the above equations can also be defined in terms of the starting photon energy (hv_{start}) and the shift in photon energy at each point in the NEXAFS spectrum (δ).

$$-\Delta = h\upsilon_{\text{start}} + \delta \tag{4.2.4}$$

Equation 4.2.5 is obtained by replacing the -Δ in Equation 4.2.3 with the definition in Equation 4.2.4. This leaves a formula for changing the photon energy scale of a NEXAFS spectrum into a binding energy scale which is relative to the Fermi level. The formula is in terms of quantities which are easily obtained during data acquisition.

$$BE_{\text{NEXAFS}} = BE_{\text{core-hole}} - h\upsilon_{\text{start}} - \delta \tag{4.2.5}$$

The photon energy for the NEXAFS spectrum is calibrated by not moving the monochromator after obtaining the NEXAFS spectrum and acquiring a core level photoemission spectrum with both first and second order light. The shift in kinetic energy between the two spectra can be used to find the actual photon energy used to record the spectrum.

Figure 4.1b) shows an energy level alignment diagram for a monolayer of Ru 455 on a rutile TiO_2(110) substrate. The diagram shows that the LUMO of the dye complex (the most intense peak of the NEXAFS spectrum) lies within the substrate band gap, this means that charge transfer from the molecule to the substrate should not occur for this orbital. The other peaks seen in the NEXAFS spectrum lie within the conduction band of the substrate. This means that charge transfer is theoretically possible for these peaks although there are other factors which may prevent charge transfer from occurring in practice.

Having a molecular orbital incapable of charge transfer is an advantage for performing the core-hole clock implementation of RPES. The decay in the signal between the NEXAFS and RPES spectra for an orbital incapable of charge transfer can be compared with other orbitals to more accurately determine whether charge transfer is occurring in those orbitals and at what rate. It should be noted that the energy level alignment diagram applies only to a system with a core-hole. The core-hole causes an increase in the binding energies of the unoccupied levels as the emitted electron is less well screened from the charge of the atomic nucleus. The effect leads to a binding energy shift on the order of eV compared to a system without a core-hole. The shift can be removed by comparing the HOMO-LUMO energy gap from the core hole experimental data with optical studies and the magnitude of the shift can provide additional information on the system.

4.3 Core-level resonant photoemission spectroscopy

In this work resonant photoemission spectroscopy (RPES) was used extensively to quantify the rate of charge transfer from unoccupied molecular orbitals to the substrate for each DSC system studied. In this section we will discuss the processes that occur after an electron has been resonantly excited from a core level to an unoccupied level, in particular the decay events which lead to the emission of an electron. This section will also describe how the spectra are obtained and the core-hole clock implementation of RPES which is used to determine the timescale of the charge transfer process.

4.3.1 Resonant electron processes

After initial excitation by an X-ray photon the system has to relax to a more stable configuration. Potential decay processes involving the emission of an electron are shown below in Figure 4.3. In the diagram the semiconductor energy levels are shown. This is relevant for the experimental work on TiO_2. Figure 4.3a) shows the potential decay processes that occur after a core electron is excited to an unoccupied level overlapping with the semiconductor band gap. In this case no electron transfer can occur as there are no states in the band gap of the semiconductor available for the electron to transfer into.

The excited state is then shown relaxing via resonant Auger decay. This is similar to a normal Auger decay except for the presence of the excited electron in an unoccupied energy level. This process is also known as spectator decay due to the excited electron

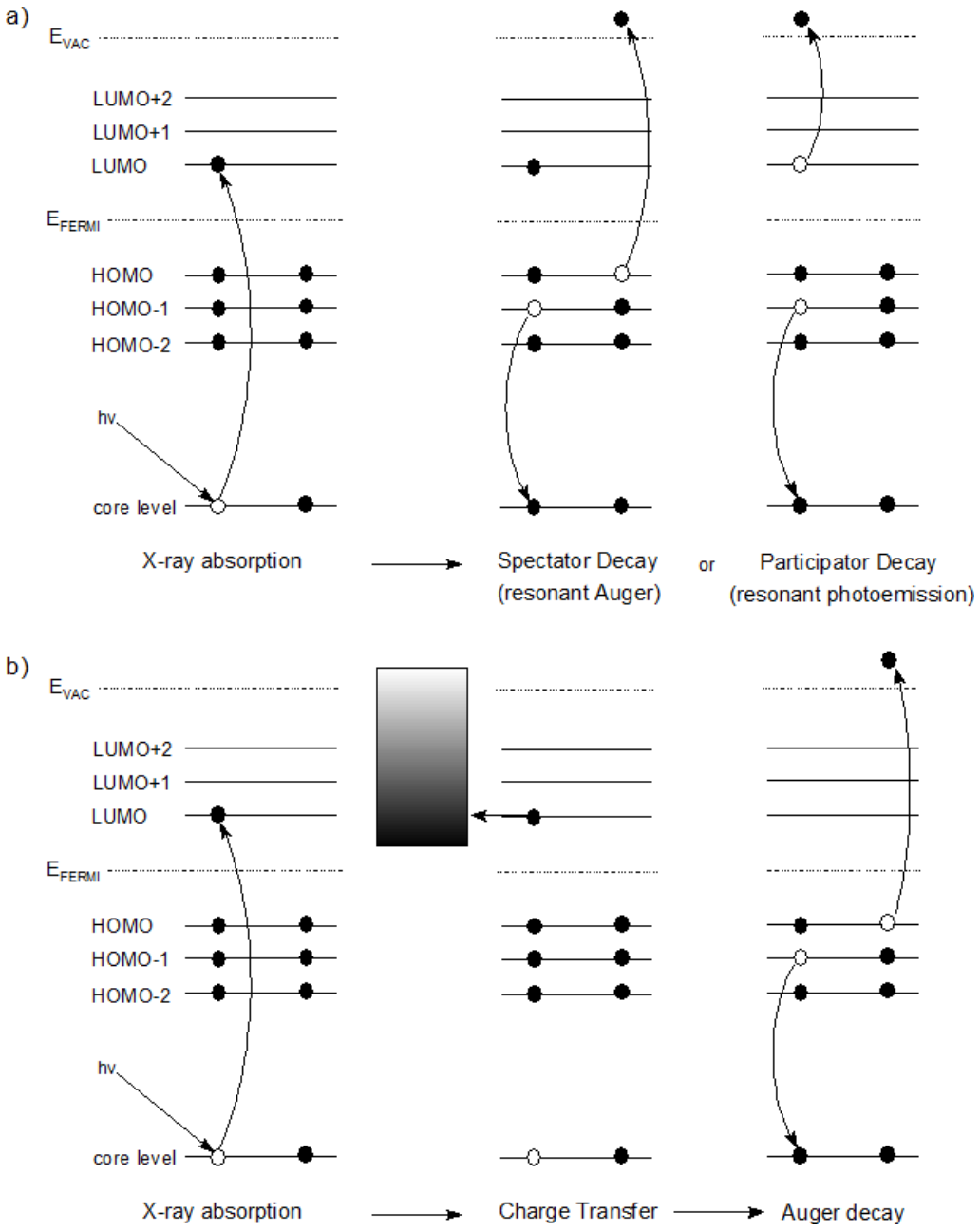

Figure 4.3: Diagram showing potential electron ejection processes after initial excitation by an X-ray photon. Part a) shows an electron excited to an unoccupied molecular orbital, the electron then decays via either participator or spectator decay processes. Part b) shows an electron excited to a molecular orbital which overlaps with available states in the substrate. The excited electron is transferred to the substrate and the excited system relaxes via Auger decay.

being a spectator in the process and not taking part in the decay. This process provides no information on the absorbed photon energy due to the excited electron not being involved in the decay. The emitted Auger electron has constant kinetic energy which is independent of the absorbed photon energy, as with normal Auger emission. The presence of the spectator electron causes a slight shift in the kinetic energy of the Auger electron compared to normal emission. This is due to the spectator electron screening the effect of the core-hole, which decreases the effective binding energy of the Auger electron and increases its kinetic energy compared to ordinary Auger emission. The effect is called the spectator shift and the energy difference it causes between the two types of Auger electron is typically too small to accurately resolve the processes.[68]

The second possible electron emission decay event shown in Figure 4.3a) is participator decay. In this case the originally photoexcited electron actually participates in the decay process. As this process involves the photoexcited electron the emitted electron carries information on the unoccupied state that the excited electron decayed from and the absorbed photon energy. In participator decay the system is left with a hole in the HOMO level that the electron was excited from. The same final state also results from direct photoemission from this level. As these processes result in the same final state the emitted electron appears to have the same binding energy. Due to participator decay only occurring on resonance, and at the same binding energy as direct photoemission, the process is also known as resonant photoemission.

Figure 4.3b) shows possible de-excitation processes for a core-level electron excited to an unoccupied level which overlaps with the conduction band of the semiconductor. Electron transfer between the molecule and the substrate is possible as the levels overlap energetically. However, there are other factors influencing the transition such as the spatial overlap of the levels and quantum selection rules which may hinder the electron transfer. Charge transfer is also in competition with participator decay which may occur before charge transfer can take place. The strength of the coupling between the relevant molecule and substrate orbitals determines the probability that the excited electron will charge transfer or undergo participator decay. If charge transfer does occur then the system relaxes via normal Auger emission to fill the hole in the core level left by the photoexcited electron.

If some but not all of the excited electrons in the molecule charge transfer into the substrate then the decay events that occur will be a proportional mixture of the processes described above. In order to determine which decay processes have taken place in a sample and in what proportion it is necessary to measure the kinetic energy of the emitted electrons. Spectator decay and normal Auger decay signals usually can-

not be resolved energetically meaning that they cannot be used to determine whether charge transfer is occurring. This leaves the participator decay and charge transfer processes which are in competition with one another. If the participator decay signal is not present in a spectrum it indicates that most if not all electrons have charge transferred into the substrate. The higher the intensity of the participator peak the lower the efficiency of charge transfer.

It is important to know which molecular orbitals are capable of transferring electrons into the substrate so that they can be studied. This can be determined using energy level alignment diagrams as discussed previously in Section 4.2.

4.3.2 Data acquisition and identification of features

Resonant photoemission spectra are acquired in a similar way to normal photoemission spectra. Both techniques work by measuring the kinetic energy of the emitted electrons using an electron analyser. The difference between these two techniques is in the choice of photon energy. In resonant spectra the photon energy is selected to be exactly the energy difference between the unoccupied and core levels involved in the transition i.e. the photon energy is at resonance. In normal photoemission the photon energy is chosen so that the emitted electrons have ~ 50 eV of kinetic energy.

In a resonant photoemission spectrum a valence band spectrum is taken at a range of different photon energies. These spectra can be displayed in a 2D figure to show the resonances which occur at different photon energies. A sample RPES spectrum of an N3 multilayer on rutile TiO_2(110) is shown in Figure 4.4. Below the absorption edge at 399 eV the photon energy is not enough to cause excitation to an unoccupied level so there are no decay events in this pre-edge region. At approximately 399 eV the photon energy is on resonance for a transition from a core-level to the LUMO level, at this photon energy decay events can occur and signals emerge in the RPES spectrum. As the photon energy is increased more resonances occur due to transitions to the higher energy LUMO states, this produces more signals in the RPES spectrum from the subsequent decay events.

The different decay processes in the RPES spectrum can be identified by examining the position and shape of the peaks. A schematic top-down diagram of a resonant photoemission spectrum with the peaks highlighted is shown in Figure 4.5. Constant binding energy features observed across the whole range of photon energies are due to direct photoemission. Features observed on resonance can be the result of participator decay, spectator decay or normal Auger decay. As discussed previously spectator decay and

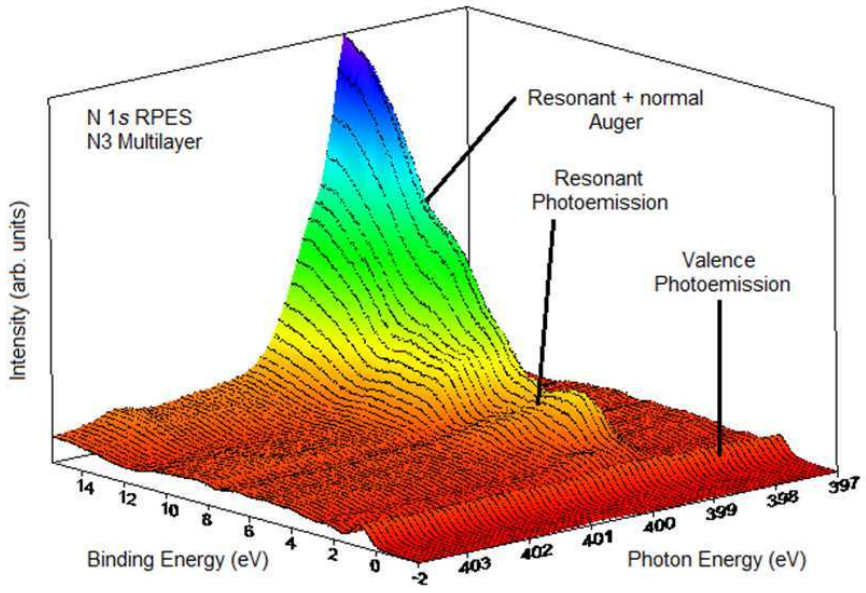

Figure 4.4: N 1s Resonant photoemission spectrum of a multilayer of N3 on rutile TiO_2(110). Valence band spectra were taken over a binding energy of -2 to 15.5 eV, using a photon energy range of 397 to 404 eV

normal Auger decay are normally unresolvable, as there is only a small spectator shift in the kinetic energy of the electrons that differentiates the two processes. The peaks can therefore be classified as either Auger type peaks or participator peaks.

The participator decay peaks are present at lower binding energy than Auger peaks as the decay involves an unoccupied level and a valence level, whilst in Auger decay both of the electrons involved are from valence states. The unoccupied levels have a lower binding energy than the valence levels meaning that emitted electrons have a higher kinetic energy in participator decay than Auger decay. As the different processes cause peaks at different binding energies it is possible to identify the peaks in the RPES spectrum and separate them in analysis.

Both normal Auger and spectator Auger decay do not involve the originally excited electron. This means that these processes are independent of the incident photon energy and the emitted electrons have constant kinetic energy. An exception occurs for the Auger resonant Raman (ARR) regime,[68, 69] when the electron is localized and undergone excitation to certain states. In that case the resonant Auger feature disperses with constant binding energy. ARR relatively rarely occurs as it requires the photon energy bandwidth to be narrower than the natural line width of the electronic energy levels which does not normally occur.

Another problem is that the complexity of the overlapping features in an RPES spec-

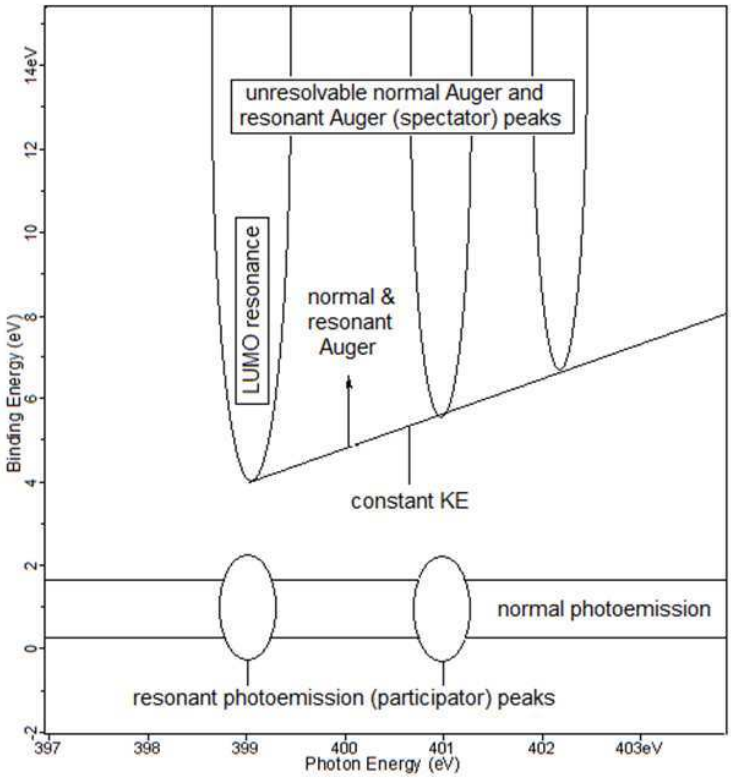

Figure 4.5: Schematic diagram identifying the different processes that can give rise to peaks in a resonant photoemission spectrum. A constant kinetic energy line has been drawn on the spectrum which helps assign the features

trum can prevent the decay channels from being identified. The example plots shown are not in the ARR regime so the Auger peaks drift along constant kinetic energy lines. As the photon energy increases the apparent binding energy also increases as the kinetic energy is unchanged. The separation of the participator and Auger peaks at the LUMO is equal to the energy of the HOMO-LUMO gap. The Auger peak at the LUMO photon energy can be used to determine the low binding energy limit. Drawing a line of constant kinetic energy from this limit allows for the identification of Auger and participator peaks. Auger peaks will occur at higher binding energies than the line and participator peaks occur on resonance at lower binding energies than the line.

4.3.3 Core-hole clock quantification method

By analysing RPES spectra it is possible to determine whether charge transfer occurs from a specific unoccupied molecular orbital. The intensity of features in NEXAFS and RPES spectra can be compared and used in the core-hole clock implementation of RPES. The core-hole clock method allows quantification of an upper time limit for the charge transfer process for each unoccupied level. This provides more information on the charge transfer process and allows for the comparison of several molecular orbitals in a single molecule or similar orbitals in closely related molecules, this is especially useful when combined with DFT simulations on the geometry of the orbitals involved.

In section 4.3.1 it was shown that the presence of a participator decay signal in an RPES spectrum indicates that the charge transfer process is not occurring on the same timescale as the decay, whilst the absence of the signal signifies that charge transfer is taking place on a similar or faster timescale. In order to accurately determine the amount of charge transfer occurring a comparison must be made to a similar system which is unable to charge transfer to the substrate. Dye molecules above the first adsorbed layer cannot charge transfer to the surface due to the fact that these molecules are separated from the substrate and the solid forms of the dyes are non-conducting. By comparing the participator peaks in the multilayer and monolayer RPES spectra it is possible to determine whether charge transfer is occurring or not.

To more accurately measure the amount of charge transfer the intensities of the peaks in the RPES spectra are measured and compared for monolayer and multilayer samples, the lifetime of the core-hole decay can be used to quantify an upper time limit in which charge transfer occurs. This approach is known as the core-hole clock method. Charge transfer has to occur before the core-hole has decayed as the decay process will remove the excited electron which is capable of charge transfer.

A theoretical model has been developed to allow the core-hole clock method to be used on experimental data. The model relies on several assumptions on the core-hole decay and charge transfer processes. Firstly the charge transfer and core-hole decay processes are assumed to be independent of each other, the core-hole decays no matter whether the electron is transferred or not. The second assumption is that the probability of charge transfer is exponential as a function of time.[68, 70] Finally it is assumed that the probability of the core-hole decay is also exponential as a function of time.[68, 71–73]

The number of molecular systems left in the excited state at time t (N(t)) is shown in Equation 4.3.1. Where $N(0)$ is the number of excited systems at time t=0 and τ is the timescale of the event of interest.

$$N(t) = N(0)exp^{-t/\tau} \tag{4.3.1}$$

The probability of the core-hole decaying before time T ($P_{chd}(T)$) is shown below in Equation 4.3.2. τ_{chd} is the average time of the core hole decay. Similarly Equation 4.3.3 shows the probability of charge transfer not occurring before time T ($P_{noCT}(T)$), where τ_{CT} is the average time of charge transfer.

$$P_{\text{chd}}(T) = \int_0^{\tau} \frac{1}{\tau_{\text{chd}}} exp^{-t/\tau_{\text{chd}}} dt \tag{4.3.2}$$

$$P_{\text{no CT}}(T) = 1 - \int_0^{\tau} \frac{1}{\tau_{\text{CT}}} exp^{-t/\tau_{\text{CT}}} dt \tag{4.3.3}$$

Since the core-hole decay and charge transfer events are assumed to be independent, the probability that charge transfer occurs as well as core-hole decay is obtained by combining the probabilities of each process as seen in Equation 4.3.4.

$$P_{\text{chd \& no CT}}(T) = \int_0^{T} P_{\text{chd}}(t) P_{\text{no CT}}(t) dt \tag{4.3.4}$$

Equation 4.3.5 is obtained by substituting Equations 4.3.2 and 4.3.3 in Equation 4.3.4. Completing the integrations in Equation 4.3.5 gives Equation 4.3.6.

$$P_{\text{chd \& no CT}}(T) = \int_0^{T} \frac{1}{\tau_{\text{chd}}} exp^{-t/\tau_{\text{chd}}} \left[1 - \int_0^{T} \frac{1}{\tau_{\text{CT}}} exp^{-t'/\tau_{\text{CT}}} t' \right] dt \tag{4.3.5}$$

$$P_{\text{chd \& no CT}}(T) = \frac{\tau_{\text{CT}}}{\tau_{\text{chd}} + \tau_{\text{CT}}} \left[1 - exp^{-(T/\tau_{\text{chd}} + T/\tau_{\text{CT}})} \right] \tag{4.3.6}$$

Spectra are measured at far greater timescales than these two processes, so by taking the limit as $T \rightarrow \infty$ Equation 4.3.6 becomes Equation 4.3.7.

$$P_{\text{chd \& no CT}}(\infty) = \frac{\tau_{\text{CT}}}{\tau_{\text{chd}} + \tau_{\text{CT}}} \tag{4.3.7}$$

This probability can also be put in terms of the experimental intensity of the resonant and normal Auger channels ($I_{resonant}$ and $I_{normal\,Auger}$ respectively). When no charge transfer occurs the decay channel is resonant and can be either spectator or participator decay, the normal Auger decay process after charge transfer is non-resonant. The experimental intensity of the resonant channels can be normalised by dividing by the summation of the resonant and non-resonant intensities as shown in Equation 4.3.8.

$$P_{\text{chd \& noCT}}(\infty) = \frac{I_{\text{resonant}}}{I_{\text{resonant}} + I_{\text{normal Auger}}} \tag{4.3.8}$$

Equation 4.3.9 is obtained by equating equations 4.3.7 and 4.3.8.

$$\frac{\tau_{\text{CT}}}{\tau_{\text{chd}} + \tau_{\text{CT}}} = \frac{I_{\text{resonant}}}{I_{\text{resonant}} + I_{\text{normal Auger}}} \tag{4.3.9}$$

In section 4.3.2 it was established that the normal Auger and spectator decay processes were too similar in energy to be separated. This leaves the participator peaks to examine the charge transfer process. The participator peak intensities for the charge isolated multilayer and the charge coupled monolayer can be measured from the experimental RPES spectra. The decrease in the participator peak intensity for the monolayer compared to the multilayer ($I_{isolated}^{participator}$-$I_{coupled}^{participator}$) can be normalised to the isolated participator peak intensity to determine the probability of charge transfer occurring in the studied system as shown in Equation 4.3.10.

$$P_{\text{chd \& CT}}(\infty) = \frac{I_{\text{isolated}}^{\text{participator}} - I_{\text{coupled}}^{\text{participator}}}{I_{\text{isolated}}^{\text{participator}}} \tag{4.3.10}$$

As the excited molecule is certain to relax in the timeframe of the experiment, the two probabilities for the two possible decay scenarios must add up to 1 as shown in Equation 4.3.11.

$$P_{\text{chd \& CT}}(\infty) = 1 - P_{\text{chd \& no CT}}(\infty) \tag{4.3.11}$$

Equation 4.3.12 is attained by substituting Equation 4.3.7 into Equation 4.3.11. Equation 4.3.13 is a rearrangement of Equation 4.3.12.

$$P_{\text{chd \& CT}}(\infty) = 1 - \frac{\tau_{\text{CT}}}{\tau_{\text{chd}} + \tau_{\text{CT}}} \tag{4.3.12}$$

$$P_{\text{chd \& CT}}(\infty) = \frac{\tau_{\text{chd}}}{\tau_{\text{chd}} + \tau_{\text{CT}}} \tag{4.3.13}$$

Equation 4.3.14 is obtained by equating Equations 4.3.13 and 4.3.10. Equation 4.3.15 is a rearrangement of Equation 4.3.14 to show how the variables are used to calculate the timescale of charge transfer.

$$\frac{\tau_{\text{chd}}}{\tau_{\text{chd}} + \tau_{\text{CT}}} = \frac{I^{\text{participator}}_{\text{isolated}} - I^{\text{participator}}_{\text{coupled}}}{I^{\text{participator}}_{\text{isolated}}} \tag{4.3.14}$$

$$\tau_{\text{CT}} = \tau_{\text{chd}} \frac{I^{\text{participator}}_{\text{coupled}}}{I^{\text{participator}}_{\text{isolated}} - I^{\text{participator}}_{\text{coupled}}} \tag{4.3.15}$$

The experimental intensities for the participator peaks need to be normalised to the intensity of the same participator peaks in the NEXAFS spectra of the monolayer and multilayer dye samples.

$$\tau_{CT} = \tau_{chd} \frac{\dfrac{I^{\text{participator}}_{\text{coupled}}}{I^{\text{NEXAFS}}_{\text{coupled}}}}{\dfrac{I^{\text{participator}}_{\text{isolated}}}{I^{\text{NEXAFS}}_{\text{isolated}}} - \dfrac{I^{\text{participator}}_{\text{coupled}}}{I^{\text{NEXAFS}}_{\text{coupled}}}} \tag{4.3.16}$$

Equation 4.3.16 is the equation used to obtain charge transfer time scales for each unoccupied molecular orbital from the experimental data in this work. By comparing charge transfer timescales between orbitals in the same molecule and a similar orbital in different molecules we hope to uncover methods of improving the efficiency of charge transfer through molecular design.

CHAPTER 5

Electrospray deposition

The molecules studied in this work were non-volatile and thermally fragile meaning that they could not be deposited in vacuum onto a clean surface using traditional means such as K-cells. In this work molecules were therefore deposited using electrospray deposition (ESD) onto surfaces cleaned in ultra-high vacuum. By using electrospray deposition we can study a broader range of molecules than possible using traditional methods and we can maintain the cleanliness of the surface during deposition. This chapter will describe the background of electrospray deposition and will include a description of the apparatus used in this work and the physical principles that underlie it.

5.1 Background

Electospray ionisation was first developed by Fenn and co-workers in the 1980s.[74, 75] This work later led to Fenn being given a share of the 2002 Nobel prize in chemistry.[76] Electrospray ionisation was first developed for analytical chemistry applications. To perform techniques such as mass spectrometry it is necessary to have the molecules in the gas phase.[74, 77] Electrospray ionisation is necessary to take thermally labile or non-volatile molecules, such as bio-molecules, into the gas phase where they can be studied. The molecules first need to be in the liquid state which can be done by dissolving or suspending the molecules. The liquid flows through a small metal capillary with an electric field applied to it. The electric field ionises droplets and forms an electrospray plume. This technique has found a wide range of applications including depositing molecules at ambient pressure which is used in the production of lithium ion batteries,[78] organic light emitting diodes[79] and gas sensors.[80, 81] Biological thin films can also be produced using this technique for applications such as immune-

system resistant coatings for medical implants[82–84] and degradable coatings that release drugs over time.[85]

Early forms of the electrospray ionisation systems could produce a molecular jet in a pressure range from ambient to medium vacuum. The current generation of electrospray deposition was partly developed in Nottingham and allows for the deposition of non-volatile or thermally labile molecules. This technique allows for *in situ* deposition of molecules onto surfaces cleaned in ultra-high vacuum.

One of the most popular options for depositing organic molecules under UHV conditions is the Knudsen cell (K-cell).[86, 87] The substance to be deposited in placed within a cleaned crucible and the crucible is mounted within the K-cell housing. The K-cell is attached to a UHV chamber and placed under vacuum, the crucible can then be heated by passing an electric current through a wire threaded around the crucible. The molecules will sublime (change state straight from the solid phase to the gas phase) into vacuum once the temperature inside the crucible reaches the sublimation temperature of the sample. The molecules will then travel through the vacuum towards a surface held in line with the aperture of the K-cell.

This sublimation technique can be carried out in UHV. This means that the sample surface can be cleaned and will remain relatively clean throughout the experiment. The temperature of the crucible can be simply controlled by varying the current applied to the wire, raising the temperature above the sublimation temperature increases the rate of deposition. This means that it is possible to control the rate of deposition allowing for greater control over the coverage of molecules on the surface. The main limitation of sublimation is that applying high temperature to the molecules in the crucible can lead to the molecules becoming damaged. The worst case scenario occurs when the decomposition temperature of the molecules is lower than their sublimation temperature. In this case the molecules break apart before they sublime and only fragments of the original molecule will be deposited.

Many of the molecules studied are composed of a ruthenium metal centre with mostly bidentate ligands surrounding the centre. The bonding of the ligands to the metal centre is relatively weak and would not survive the heating process during sublimation. The main area of research with these molecules is how they bond to the substrate of the solar cell and the interactions between the adsorbed molecules and the substrate. This interface is key to how incident light energy is transformed into electrical energy. Without using the electrospray device the only options for studying these molecules on the titanium dioxide surface would be *ex situ* preparations, this would lead to contamination of the samples which would make it harder to study these molecules effec-

tively. Using the UHV electrospray device we can study a wide range of thermally labile molecules. This technique has been successfully used previously to deposit carbon nanotubes,[88] C_{60} molecules,[89–91] zinc protoporphyrin,[92] polymers,[93] biomolecules,[77] host-guest complexes[94] and the N3 dye complex along with related molecules.[7, 95, 96]

5.2 Apparatus and physical processes

To perform the electrospray process the molecule of interest must be dissolved or suspended in a suitable solvent. Methanol is a common solvent for the molecules studied in this work. A solution of molecules in pure methanol is difficult to electrospray however, so water is commonly added to methanol solutions to make them easier to electrospray. Other solutions which can be electrosprayed include dichloromethane and a mixture of toluene and acetonitrile. These solutions are typically used only if the molecule to be studied does not dissolve in methanol as these solutions are significantly harder to spray. After the molecule has been dissolved or suspended in solution the mixture is placed into a sealed reservoir with a small exit which has a 2 μm frit filter (Valco). The filter is used to prevent undissolved clusters or particulates from clogging the narrow PEEK (polyetheretherketone) tubing which has an inner diameter of 860 μm, the tubing leads to the needle of the electrospray device. Positive pressure applied to the reservoir causes the liquid to flow through the tubing, in earlier iterations of the electrospray device nitrogen was used to apply pressure. In the current version of the device a syringe is used as the reservoir and pressure is applied by pushing the plunger. After passing through the PEEK tubing the liquid enters a stainless steel tube with an inner diameter of 250 μm, before entering a hollow stainless steel needle with an inner diameter of 100 μm (New Objective, USA) known as the emitter. The narrow diameter of the tubes leads to a low flow rate of $\sim$10 μl min^{-1}. The steel tube and emitter are secured within insulated housing and the position of the emitter can be changed using a manipulator to give precise control over the spray position.

When the liquid reaches the end of the emitter the liquid forms rounded droplets as seen in Figure 5.1a), the droplet will increase in size until the weight of the droplet overcomes the surface tension of the liquid and the droplet falls off the emitter. To produce a spray a large positive bias is applied to the steel tube and emitter. The positive bias removes electrons from molecules inside the liquid at the interface between the liquid and the inner surface of the steel tubes. After losing electrons the molecules become positive ions, these positively charged molecules repel each other and are re-

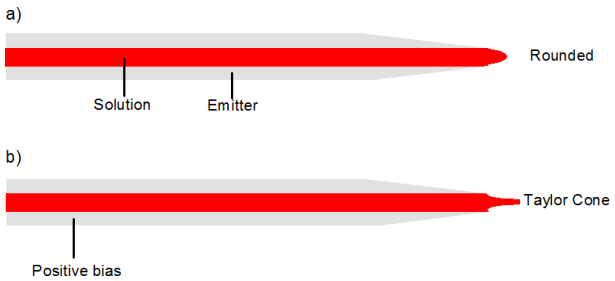

Figure 5.1: Part a) shows the solution of molecules in the emitter when the emitter is grounded, the liquid emerges from the capillary tip in a rounded drop. Part b) shows what happens when a large positive potential is applied to the emitter, the molecules become charged and repel each other and the emitter walls causing the formation of a Taylor cone.

pulsed from the sides of the emitter. To minimise this Coulomb repulsion the liquid forms a tapered shape at the exit of the emitter known as a Taylor cone as shown in Figure 5.1b).[97] By increasing the voltage applied to the emitter the liquid at the exit of the emitter changes from a rounded shape to a Taylor cone shape. At higher voltages the Coulomb repulsion increases and can overcome the surface tension of the Taylor cone causing a jet of positively charged droplets to be emitted from the cone.

After being emitted from the Taylor cone the droplets travel through the air towards an entrance capillary. As the droplets move through the air, solvent molecules and ions evaporate from the droplets. This decreases the size of the droplets and increases the charge density within the droplets. Once the charge density becomes large enough the droplets split apart in a process called the Coulomb explosion. The surface energy of the droplet is described in Equation 5.2.1

$$E_s = 4\pi r^2 \gamma \tag{5.2.1}$$

where E_s is the surface energy of the droplet, r is the radius of the droplet and γ is the surface tension of the liquid. The electrostatic energy of a charged droplet can be determined using Equation 5.2.2

$$E_q = \frac{\epsilon_0}{2} \int_V E^2 dV \tag{5.2.2}$$

where ϵ_0 is the permittivity constant, E is the magnitude of the electric field and the integral is over all space. The net charge of the droplet q resides on the surface of the droplet. From Gauss' law $E = 0$ inside the droplet and $E = q/4\pi\epsilon_0 r'^2$ outside the droplet, where r' is the radius in spherical coordinates. Replacing E in Equation 5.2.2 gives Equation 5.2.3

$$E_q = \frac{\epsilon_0}{2}\int_{-\pi}^{\pi}\int_{0}^{2\pi}\int_{r}^{\infty}\left(\frac{q}{4\pi\epsilon_0 r'^2}\right)^2 r'^2 sin\theta dr' d\theta d\phi = \frac{q^2}{8\pi\epsilon_0 r'} \tag{5.2.3}$$

The surface and electrostatic energies can both be differentiated with respect to the radius to give the change in energy for an infinitesimal change in the radius of the droplet. Equations 5.2.4 and 5.2.5 show the difference in energy for the surface tension and electrostatic energy respectively.

$$\Delta E_s = 8\pi r\gamma dr \tag{5.2.4}$$

$$\Delta E_q = \frac{-q^2 dr}{8\pi\epsilon_0 r'^2} \tag{5.2.5}$$

where ΔE_s and ΔE_q are the changes in surface energy and electrostatic energy respectively. The point at which the droplets split apart is when these two terms are equal, this is known as the Rayleigh limit. Equations 5.2.4 and 5.2.5 have been equated and rearranged for r in Equation 5.2.6.

$$r = \left(\frac{q^2}{64\pi^2\epsilon_0\gamma}\right)^{1/3} \tag{5.2.6}$$

After splitting through Coulomb explosion the droplets become smaller and can go through more cycles of solvent evaporation and Coulomb explosion to produce increasingly smaller droplets turning the jet of droplets into a plume of very fine droplets. Figure 5.2 is used to illustrate the Coulomb explosion process. The voltage applied to the emitter can be adjusted to optimise the shape and size of the plume. Ideally the plume should consist of a very fine mist of particles and the plume should have a large lateral size, these properties indicate that Coulomb explosion is occurring effectively and that the droplets are very small. Usually the ideal bias is $\sim$ 2.3kV although optimisation will need to be carried out on this voltage especially when using different solvents. To view the plume a light source can be used perpendicular to the jet and the observers eye-line to enhance the visibility of the droplets. An image of the plume is shown in Figure 5.3

To transfer the molecules into ultra-high vacuum the droplets will pass through a series of differentially pumped chambers within the electrospray device. The chambers are connected using apertures increasing in diameter from 0.5 to 1 mm. The apertures allow the molecules to pass through the chambers unimpeded towards the sample in the preparation chamber. The emitter, entrance capillary and apertures are aligned pointing towards the sample allowing the molecules to travel straight towards the sample

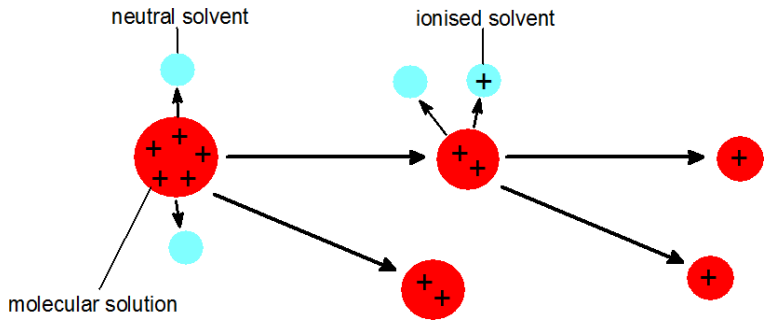

Figure 5.2: Diagram showing the process of Coulomb explosion. Drops of molecular solution lose solvent molecules and ions through evaporation, this causes the charge density of the drop to increase until it splits into more drops

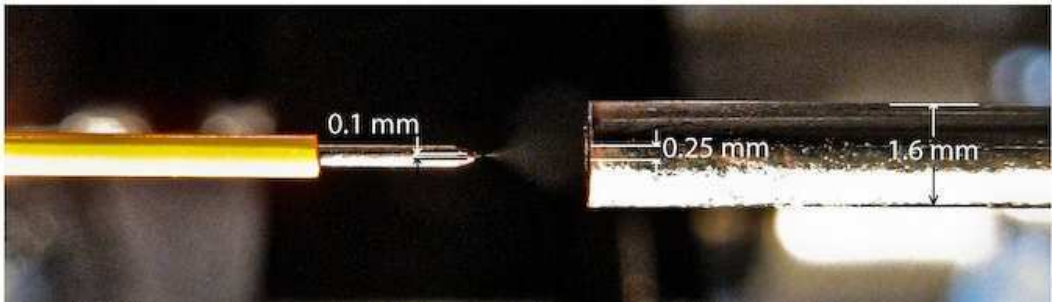

Figure 5.3: Photograph showing the Taylor cone produced by the electrospray system going into the entrance capillary leading to a preparation chamber.

if they are on the correct trajectory. The electrospray system can be optically aligned by shining a high intensity light source through the final two apertures of the electrospray and viewing the light spot on the sample. The pressure that the molecules experience moving through the electrospray apparatus is reduced from atmospheric pressure at the emitter to near-UHV in the preparation chamber. The small size of the apertures and the pumping on each chamber allow for the gradual reduction of pressure in each chamber. The deposition spot on the sample is approximately 3-4 mm in diameter with the sample at a distance of 20 cm from the final aperture, the coverage will vary according to position. In the center of the deposition the coverage will be highest and as the distance from the center increases the coverage will decrease. This means that a single deposition can be used to produce both multilayer and monolayer coverages of a molecule for study. Usually the sample is swept during deposition and the deposition time is used to control the coverage of molecules on the surface. The ions are estimated to be travelling at the speed of sound meaning they have significant kinetic energy upon colliding with the surface. Molecular damage can be an issue in very weakly bound complexes and the adsorption of the molecules could be affected by their impact with the surface. A schematic diagram showing the pressures involved in each stage of the electrospray is shown in Figure 5.4.

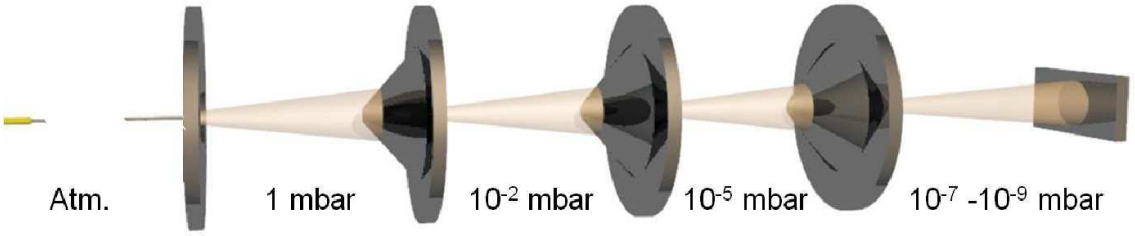

Figure 5.4: Schematic diagram of the electrospray deposition apparatus showing the pressures involved at each stage of the apparatus. An entrance capillary allows molecules to enter the apparatus. The first two stages are pumped by scroll pumps and the third by a turbo pump. The molecules then pass through the final aperture into the preparation chamber and are incident upon a sample surface.

The entrance to the electrospray apparatus consists of a small metal tube with an inner diameter of 0.25 mm and a length of 5 cm known as an entrance capillary. The capillary allows for a high flux of molecules whilst keeping the pressure in the final chamber low. The spray travels through three pumped chambers before entering the preparation chamber as shown in Figure 5.4. The chambers are separated by conical apertures with diameters increasing from 0.5 to 1 mm. The first two chambers are pumped by scroll pumps, whereas the third chamber is pumped by a 70 ls^{-1} turbomolecular pump (Varian). The pressure of the chambers decreases from approximately 1 mbar in the first chamber to 10^{-5} mbar in the third chamber. A UHV gate valve is usually placed between chamber three and the preparation chamber so that between depositions the preparation chamber can be sealed off completely from atmosphere.

The base pressures of the various preparation chambers used in this work were usually on the order of approximately 10^{-10} mbar. When the gate valve between the electrospray device and the preparation chamber is opened but no electrospray is occurring the pressure in the preparation chamber usually rises to approximately 10^{-8} mbar. After starting the electrospray process the pressure in the preparation chamber may rise to approximately 10^{-7} mbar, this increase in pressure has been attributed to residual solvent molecules evaporating from the droplets as shown by residual gas analysis in Nottingham. The increase in pressure can be used to estimate the rate of deposition of molecules on the surface and can also be used to optimise the electrospray apparatus to produce the highest flux of molecules on the surface.

The coverage of the deposited molecules on the surface can be controlled using multiple methods. By simply increasing the deposition time the coverage will increase. Also the molecular flux can be increased which will increase the rate of deposition. This can be monitored using a pressure gauge inside the preparation chamber. The position of

Figure 5.5: Photograph of a UHV electrospray system mounted onto the end chamber of beamline I311 at MAX-lab, Sweden. The syringe is covered in foil to help prevent the photodegradation of the molecules contained in the syringe. A microscope can be seen attached to the system to observe the electrospray plume, the red electrical connector has been used to ground the entrance capillary on the electrospray device.

the emitter can be optimised in front of the entrance capillary using the manipulator, also the voltage applied to the emitter and the pressure applied to the reservoir can be optimised. It is also possible to monitor the current on the sample. The positive ions hitting the surface of the sample cause the production of an electric current on the order of approximately 10 pA. The rate of deposition can change significantly between depositions so the deposition time is usually adjusted to compensate for any changes in rate. In order to keep the coverage consistent across the surface we would scan the sample in two dimensions multiple times during the deposition to average out changes in molecular flux during the deposition. This technique also increases the area of molecules on the surface providing a larger area to work with for longer experiments such as RPES.

5.3 Summary

Using an electrospray system which is compatible with a UHV system allows for the adsorption of molecules onto surfaces prepared and cleaned in UHV such as TiO_2 and Au. By performing the deposition in high vacuum conditions the surface of the sample will not undergo reconstruction or significant contamination. The UHV electrospray system allows for the deposition of thermally labile or non-volatile molecules onto a surface so that the molecules and their interaction with a surface can be analysed using UHV techniques such as photoelectron spectroscopy. A photograph of an electrospray system mounted onto a UHV chamber for sample preparation is shown in Figure 5.5.

CHAPTER 6

Bipyridine-based dye complexes on TiO_2(110)

6.1 Introduction

In this chapter experimental data is presented on three DSC dye sensitizers adsorbed onto rutile TiO_2(110), these complexes contain ligands which are based on bipyridine. One of the molecules is the N3 dye complex (here referred to as Ru 535 for consistency with the other molecules) and the other two molecules (Ru 455 and Ru 470) are closely related to it. The chemical structures of the dye complexes Ru 535 (cis-bis(isothiocyanato)bis(2,2′-bipyridyl-4,4′-dicarboxylato)-ruthenium(II)), Ru 455 (cis-bis(2,2′-bipyridyl)-(2,2′-bipyridyl-4,4′-dicarboxylic acid) ruthenium(II)) and Ru 470 (tris(2,2′-bipyridyl-4,4′-dicarboxylic acid) ruthenium(II)) are shown in Figure 6.1. Ru 535 was studied as it is currently one of the most efficient sensitizer molecules used in DSCs,[9] the other molecules were chosen as they were commercially available and had similar chemical structures to Ru 535. By comparing experimental results for these three dye complexes we hope to determine how the chemical structure of the adsorbed dye affects the efficiency of charge transfer from the dye molecules to the substrate. Changes in the chemical structure of the dye will lead to changes in the electronic structure of the DSC system, by analysing the differences between molecules we might be able to develop better sensitizers for photovoltaic and water-splitting DSCs.

Due to its high efficiency as a sensitizer in photovoltaic DSCs Ru 535 has been widely studied using a variety of experimental techniques. In particular Ru 535 has been studied adsorbed on TiO_2 using photoemission to determine the electronic levels of the system,[7, 98–100] charge transfer within the system has also been studied before using infrared transient absorption,[101] time-resolved femtosecond absorption

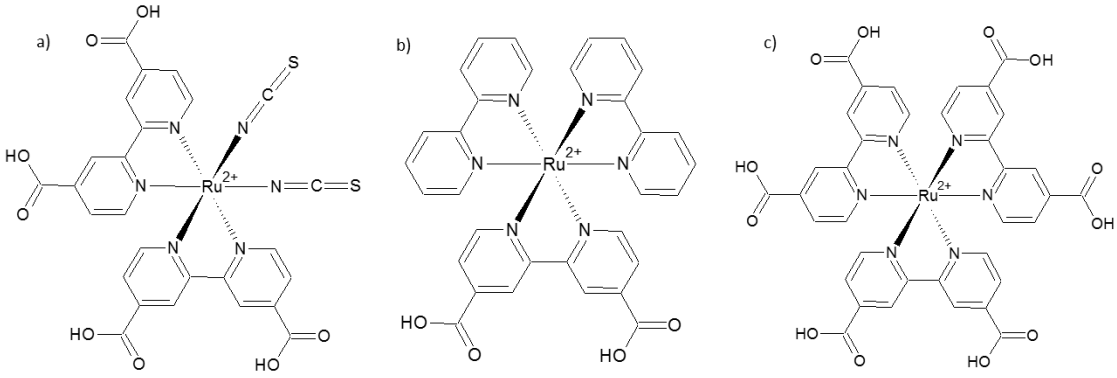

Figure 6.1: Chemical structures of the Ru 535 molecule (a) also known as N3, Ru 455 molecule (b) and Ru 470 molecule (c).

spectroscopy[102] and the core-hole clock implementation of RPES.[7] Many of these studies were on *ex-situ* prepared samples but *in-situ* prepared samples were used in a previous study by our group that produced charge transfer results.[7] The photoemission results obtained for Ru 535 in this work are included as a comparison to the results for the Ru 455 and Ru 470 complexes, the charge transfer results have decreased the upper limit on charge transfer from the previous study. Ru 455 and Ru 470 have not been studied as extensively as Ru 535 and to the best of the author's knowledge no photoemission or charge transfer measurements have been performed on either.

It is difficult to prepare in-situ samples of the molecules studied here as they undergo decomposition upon heating, this means that they cannot be deposited intact using the traditional UHV deposition method of thermal evaporation. Electrospray deposition was used to deposit the molecules onto rutile TiO_2(110) intact at monolayer and multilayer coverages as described in Chapter 5. This method of preparation allows for deposition of molecules in the pressure range of 1×10^{-6} to 1×10^{-9} mbar. By depositing molecules at these pressures the cleanness and surface reconstruction of the TiO_2 surface can be maintained apart from some hydroxylation of bridging oxygen atoms due to residual gases in the preparation chamber.[103]

In a real DSC device the dye molecules would be adsorbed to the surface of nanocrystalline TiO_2, the crystal plane of this surface is mainly anatase (101). All three molecules have bi-isonicotinic acid as a bonding ligand. Previous studies of this ligand have shown that it bonds to both rutile TiO_2(110)[14] and anatase TiO_2(101)[15] in the same manner. In addition, the optical band gaps of the two surfaces are similar with 3.05 eV for rutile[16] and 3.20 eV for anatase.[6] There are practical reasons for using a single crystal rutile substrate for our experiments instead of the more realistic nanocrystalline

one. Using a well defined periodic substrate means all of the molecules should be in the same adsorption geometry making it easier to interpret results. The rutile TiO_2(110) surface was studied instead of the anatase TiO_2(101) surface as it is cheaper and is more suitable for the experimental techniques used here. Rutile crystals can have larger surface areas than anatase crystals. As the photon beam is swept during RPES scans to avoid beam damage a larger surface area allows for longer scans to improve the RPES statistics.

In this chapter the geometric and electronic structures of N3 (Ru 535), Ru 455 and Ru 470 adsorbed on rutile TiO_2(110) are studied using photoemission spectroscopy (XPS or PES depending upon the energy of the incident photons), near-edge x-ray absorption fine structure spectroscopy (NEXAFS) and density functional theory (DFT). Charge transfer between the molecules and the substrate was studied using the core-hole clock implementation of resonant photoemission spectroscopy (RPES). Results from these techniques can be used to study the occupied and unoccupied electronic orbitals of the different molecules, and the interactions between the molecule and the substrate conduction band. This information should give insights into the charge transfer processes that occur in DSCs and may allow us to develop better dye sensitizers for photovoltaic and water-splitting DSCs.

6.2 Method

Experiments were carried out at the undulator beamline I311 at MAX-lab, Sweden.[54] The I311 end station is equipped with a Scienta SES-200 electron analyzer allowing us to obtain photoemission, NEXAFS and RPES spectra.

The experiments were performed using a single crystal rutile TiO_2(110) substrate of dimensions 10 mm $\times$ 10 mm $\times$ 1 mm (Pi-Kem, UK), mounted on a pyrolytic boro nitride heater which allowed for annealing of the sample. Cycles of sputtering using 2 keV and 1 keV Ar^+ ions, and annealing in UHV to $\sim 600\,^{\circ}C$, were used to prepare the surface. Initially, repeated cycles of sputtering and annealing were performed in order to change the crystal from an insulator to an n-type semiconductor. This process induces bulk defects which are necessary to prevent sample charging.[104] These defects, which also turn the crystal slightly blue, were minimised at the surface through annealing as described above. These defects can frequently be observed as a density of states just below the conduction band edge in the valence band photoemission spectrum. The titanium dioxide crystal was initially contaminated with potassium which was removed through repeated cycles of sputtering and annealing. The surface was

determined clean when there were negligible C 1*s* and K 2*p* core-level signals and a single Ti^{4+} oxidation state in the Ti 2*p* spectrum.

The dye molecules (Solaronix SA, Switzerland) were deposited using an *in situ* electrospray deposition source (MolecularSpray, UK), from a solution of $\sim$ 5 mg of dye in 200 ml of a 3(methanol):1(water) mixture. The apparatus used, and the process by which the molecules are taken from *ex situ* solution to *in situ* vacuum was described in detail in Chapter 5. The electrospray device is first optically aligned using a laboratory light source to make sure electrosprayed molecules will be incident upon the sample. The emitter of the electrospray equipment was held at $\sim$ 2 kV producing a Taylor cone of the molecular solution, droplets from the cone can then pass through the electrospray apparatus and then into the preparation chamber. Between depositions, the electrospray system was sealed off from the preparation chamber using a UHV gate valve. With the valve open but the needle voltage turned off and thus no electrospray occurring, the pressure in the preparation chamber was $\sim 2 \times 10^{-8}$ mbar. With the voltage turned on, the preparation chamber pressure rose to $\sim 5 \times 10^{-7}$ mbar, the additional pressure is due to residual solvent molecules in the beam.

For the electron spectroscopy data, the total instrument resolution ranges from 65-195 meV. All XPS spectra have been calibrated to the substrate O 1*s* peak at 530.05 eV,[105] and a Shirley background removed before curve fitting using Voigt functions. NEXAFS and RPES spectra were taken over the N 1*s* absorption edge and measured using the electron analyzer. For NEXAFS spectra the nitrogen Auger yield was used whilst for RPES spectra the valence band photoemission was monitored. For RPES measurements, the sample was swept continuously at a rate of at least 1.25 μm/s, following beam damage studies using NEXAFS spectra taken before and after an RPES spectrum to determine a safe exposure time.

Density functional theory simulations (DFT) calculations were carried out as an aid to interpreting the experimental data. Geometry optimizations were performed on free molecules of each dye complex using $Dmol^3$ at the DFT-generalized gradient approximation level (DFT-GGA) with the Perdew-Burke-Enzerhof (PBE) functional.[63, 64, 106] The optimized structures were then used to calculate the molecular orbitals for each molecule.

6.3 Results and Discussion

6.3.1 Adsorption

The samples used for the following spectra are classed as either *monolayer* or *multilayer*. Here a monolayer is defined as a sample having the vast majority of molecules directly adsorbed to the surface and a multilayer as having a film of molecules thick enough that the majority of photoelectrons in XPS come from molecules above the first adsorbed layer. The coverage was calibrated by approximating the inelastic mean free path (IMFP) of electrons through the molecule. The IMFP is a function of the electron's kinetic energy and was calculated using the TPP-2M equation.[107] The IMFP can be used in the Carley-Roberts formula to determine the surface concentration.[108] DFT was used to calculate the molecular footprint on the surface to calculate molecular coverage. The coverage for a set of spectra was determined by comparing the intensities of substrate and molecular O 1*s* peaks. The binding energies (BEs) of the peaks discussed are summarised in Table 6.1.

Table 6.1: BEs (eV) for monolayers of each molecule calibrated to the substrate O 1*s* peak at 530.05eV.

		Ru 535	Ru 455	Ru 470
PES				
O 1*s*	TiO_2	530.05	530.05	530.05
	C=O and COO^-	531.2	531.2	531.1
	C-OH	532.3	...	532.3
C 1*s*	Pyridine	285.0	285.6	285.4
	Thiocyanate	286.0	...	...
	Carboxyl	287.8	288.1	288.0
Ru 3*d*		280.6	281.1	281.0
N 1*s*	Thiocyanate	397.6	...	...
	Pyridine	399.7	400.4	400.1
Valence band	HOMO	1.3	1.8	1.8
N 1*s* NEXAFS				
Unshifted	LUMO	0.1	0.8	0.5
Aligned to optical data	LUMO	-1.1	-0.9	-0.75

Figure 6.2 shows the O 1*s* monolayer spectra of each dye complex on rutile TiO_2(110). For all three dye molecules the spectrum is dominated by the TiO_2 substrate oxygen peak. The two smaller peaks are due to the oxygen atoms in the carboxylic acid groups

of the bi-isonicotinic acid ligands of each molecule. For isolated dye molecules the intensity of these two peaks should be equal due to the equivalent number of carbonyl (C=O) and hydroxyl (C-OH) oxygen atoms.

Previous studies of bi-isonicotinic acid and Ru 535 have shown deprotonation of the hydroxyl groups on adsorption to TiO_2. The oxygen atoms bond to two titanium atoms on the surface so the structure is described as 2M-bidentate where M stands for metal.[7, 14] This is a common bonding arrangement for pyridine based molecules with carboxylic acid groups on the TiO_2 surface.[109–111] Ru 535 has previously been shown to bond to the surface using a single bi-isonicotinic acid ligand.[7] After deprotonation the two oxygen atoms share an electron and are chemically equivalent. The BE of this oxygen species is similar to that of the carbonyl oxygen atom in isolated molecules and the two groups are unresolvable in the XPS spectra.[14] In Figure 6.2 the monolayer COO^-/C=O:C-OH intensity ratio is approximately 3:1 for Ru 535 and 2:1 for Ru 470. There is no evidence of a hydroxyl oxygen peak in the Ru 455 spectrum. Assuming that all molecules of a dye complex bond to the surface in the same geometry these results are similar to those expected if two carboxylic acid groups of each dye complex are bonded to the surface. The expected ratios from this bonding geometry would be 3:1 for Ru 535 and 2:1 for Ru 470, and no hydroxyl peak for the Ru 455 complex, in direct agreement with the experimental results. This shows that each molecule bonds to the surface using two carboxylic acid groups which provides information on the bonding geometry of each complex.

Previous experiments have shown that Ru 535 has an additional bond to the TiO_2 surface through the sulphur atom of one of its isothiocyanate groups,[7] however the other two dye complexes do not contain isothiocyanate groups so they are incapable of bonding to the surface in this fashion. Ru 455 can only bond to the surface using both of the carboxylic acid groups on its lone bi-isonicotinic acid ligand. The adsorption geometry of a Ru 455 molecule on the rutile TiO_2(110) surface has been calculated using DFT and is shown in Figure 6.3

Ru 470 could bond to the surface using either both of the carboxylic acid groups on a single bi-isonicotinic acid ligand or a single carboxylic acid group from each of two bi-isonicotinic acid ligands. DFT calculations of the two configurations were performed using two types of cell size, the two cell sizes are shown in Figure 6.4. In the small cell the molecule barely fits into the cell corresponding to a surface with a full or almost full monolayer coverage. In the large cell the molecules are further spaced apart and do not interact with each other as much as the small cell, this corresponds more to sub-monolayer coverages of the molecule on the surface.

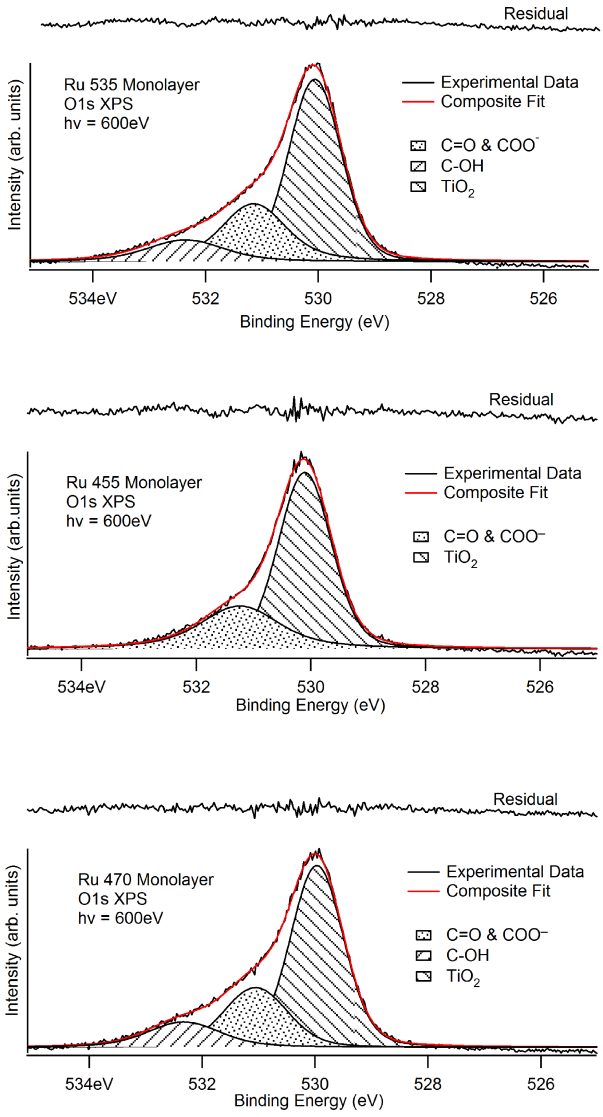

Figure 6.2: O 1*s* core-level photoemission spectra of monolayers of Ru 535 (top), Ru 455 (middle) and Ru 470 (bottom) on rutile TiO_2(110), measured using hν = 600 eV.

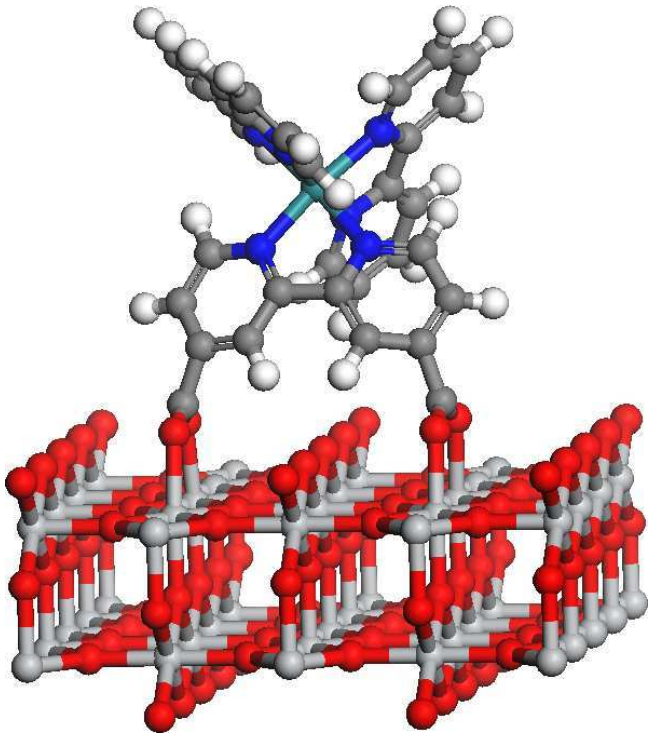

Figure 6.3: DFT calculation of a Ru 455 molecule adsorbed onto a rutile TiO_2(110) surface.

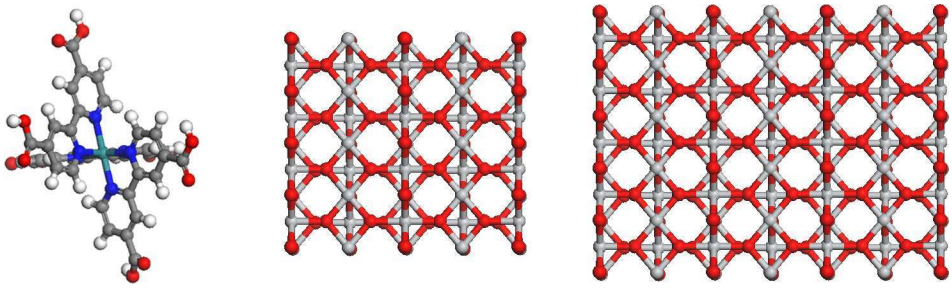

Figure 6.4: Figure illustrating the relative sizes of the Ru 470 molecule (left) and the cells used to perform the DFT simulations. The small cell (middle) corresponds approximately to full monolayer coverage and the large cell (right) corresponds to sub-monolayer coverage.

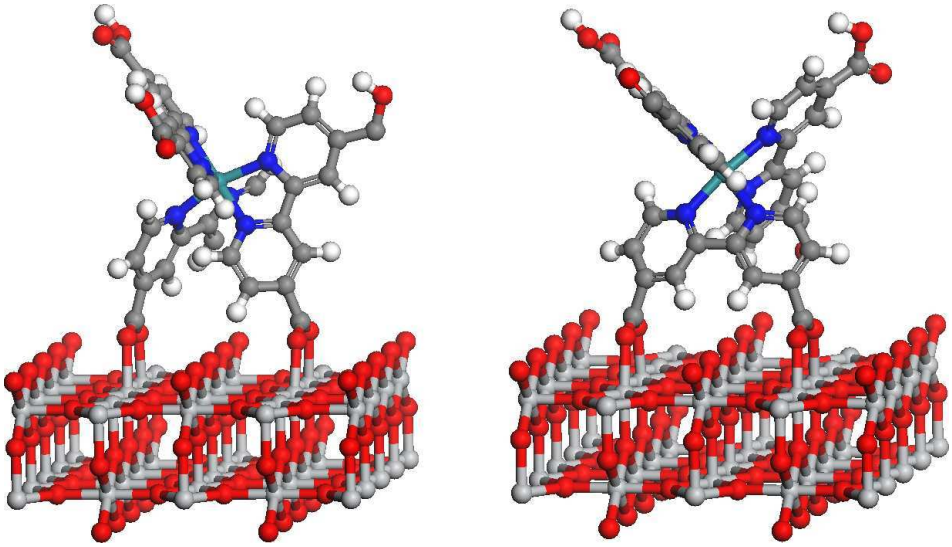

Figure 6.5: Small cell DFT optimised structures of the Ru 470 molecule adsorbed onto the rutile TiO_2(110) surface. The configurations either bond through two carboxylic acid groups on two different bi-isonicotinic acid ligands (left) or on a single bi-isonicotinic acid ligand (right)

DFT optimised small cell structures of the two different configurations of Ru 470 on the rutile TiO_2(110) surface are shown in Figure 6.5. In the small cell case the bonding structure using carboxylic acid groups from two different bi-isonicotinic acid ligands is energetically favourable compared to the other configuration by 1.60 eV. In the large cell case the structure using carboxylic acid groups from the same bi-isonicotinic acid ligand is energetically preferred by 0.25 eV. The difference is likely due to the molecule interacting with itself in the small cell. In a practical DSC device the molecules will be present at high coverages on the TiO_2 surface suggesting that the bonding configuration using carboxylic acid groups from two different ligands will be preferred. More realistically there may be a mixture of the two configurations on the surface depending on the local environment of the molecules.

Figure 6.6 shows O 1*s* XPS spectra of multilayer coverages of each dye complex. The multilayer spectrum of the Ru 535 molecule shows the expected intensity ratio of 1:1 for the C=O:C-OH oxygen peaks, which is in agreement with results reported previously.[7] The spectrum for Ru 455 appears to show evidence of deprotonation already in the multilayer from the reduced intensity of the C-OH signal. This is likely due to some hydrogen loss from the dye complex to the PF_6^- counter ions present in the deposition solution. The multilayer spectrum for Ru 470 shows the expected intensity ratio of 1:1 however an additional peak is visible in the spectrum at higher BE than the C-OH peak. This feature is most likely due to intermolecular hydrogen bonds between the

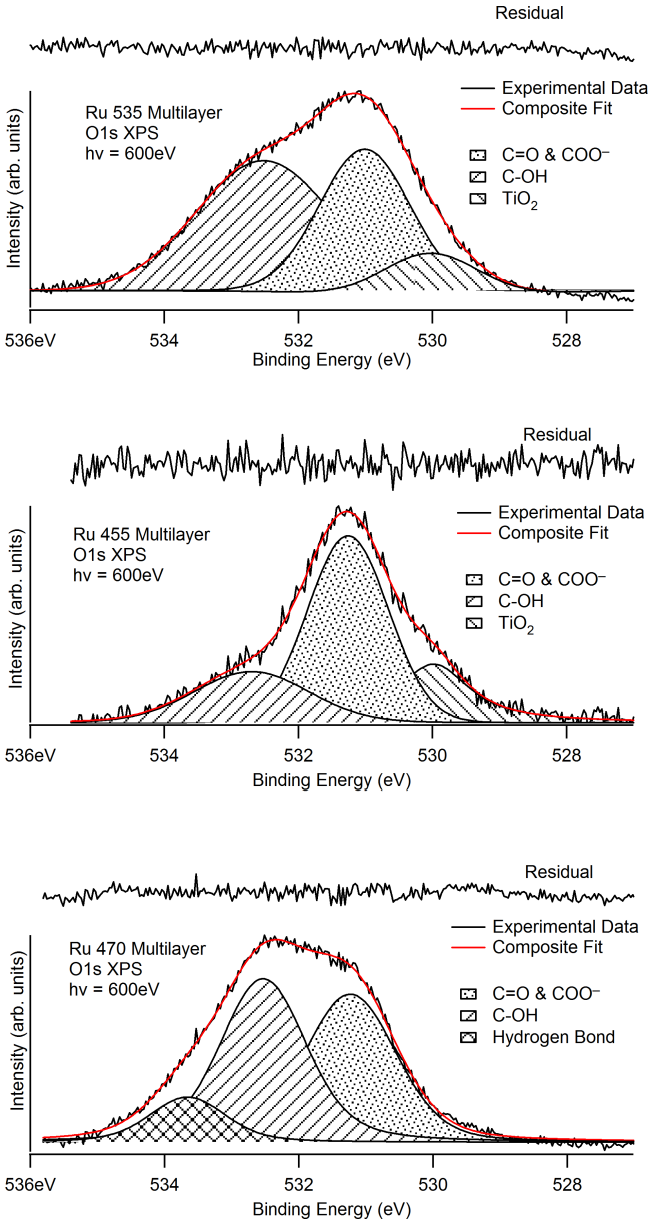

Figure 6.6: O 1*s* core-level photoemission spectra of multilayers of Ru 535 (top), Ru 455 (middle) and Ru 470 (bottom) on rutile TiO_2(110), measured using hν = 600 eV.

dye molecules in the multilayer.[109] This molecule may be more likely to form islands on the surface instead of layers as each molecule will interact strongly with its neighbours. This would be inefficient in a real DSC device where a strong interaction with the surface is a useful feature.

Figure 6.7 shows the C 1*s* and Ru 3*d* XPS spectra of monolayers of all three dye complexes. The spectra look similar for each molecule, with the exception of an additional peak in the Ru 535 spectrum attributed to the additional carbon atoms present in the isothiocyanate groups. Each spectrum is dominated by a peak due to the carbon atoms in pyridine groups. Also present at higher BE is a lower intensity peak attributed to the carbon atom in the carboxylic acid groups. There are also two peaks due to the central ruthenium ion as the Ru 3*d* state is a doublet state with a spin orbit splitting of 4.2 eV.[112] The lower BE Ru $3d_{5/2}$ peak is present at 281 eV. This is approximately 1 eV higher than metallic ruthenium,[112] which is consistent with the Ru^{2+} oxidation state of the metal centre. This strongly suggests that the molecules have retained their molecular integrity during deposition.

Figure 6.8 shows the N 1*s* XPS spectra of monolayer coverages of each dye complex. The Ru 535 molecule shows two peaks due to the nitrogen atoms in its pyridine and thiocyanate groups, in agreement with previously reported results.[7] The Ru 455 dye complex shows only a single nitrogen peak as expected from its chemical structure. Ru 470 also exhibits a single peak reflecting the structure of the molecule but also a low binding energy tail, possibly due to a small amount of impurities in the deposition solution.

6.3.2 Electronic Structure

In a DSC, electrons are photoexcited from high-lying occupied molecular orbitals to previously unoccupied molecular orbitals. For the excited electron to be injected into the substrate, the unoccupied level in question must overlap with available states in the substrate conduction band. Spectra representing the occupied and unoccupied states of monolayers of each dye complex have here been placed on a common BE scale as shown in Figure 6.9, following the procedure described in Section 4.2. This procedure has previously been performed on a monolayer of Ru 535.[7] The resulting energy level alignment diagrams can be used to identify the potential charge transfer processes that can occur in the model charge transfer centres.[113–116]

Figure 6.9 shows the N 1*s* (Auger yield) NEXAFS and valence photoemission spectra for a monolayer of each dye complex, along with the clean substrate valence photoe-

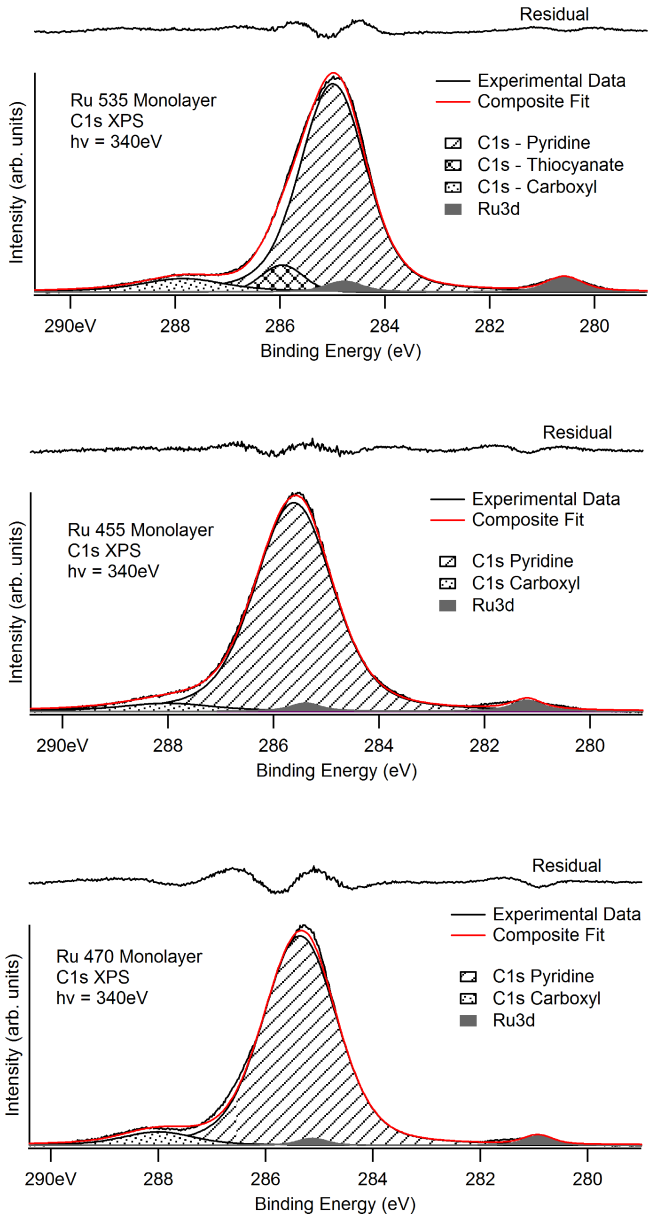

Figure 6.7: C 1*s* and Ru 3*d* core-level photoemission spectra of monolayers of Ru 535 (top), Ru 455 (middle) and Ru 470 (bottom) on rutile TiO_2(110), measured using hν = 340 eV.

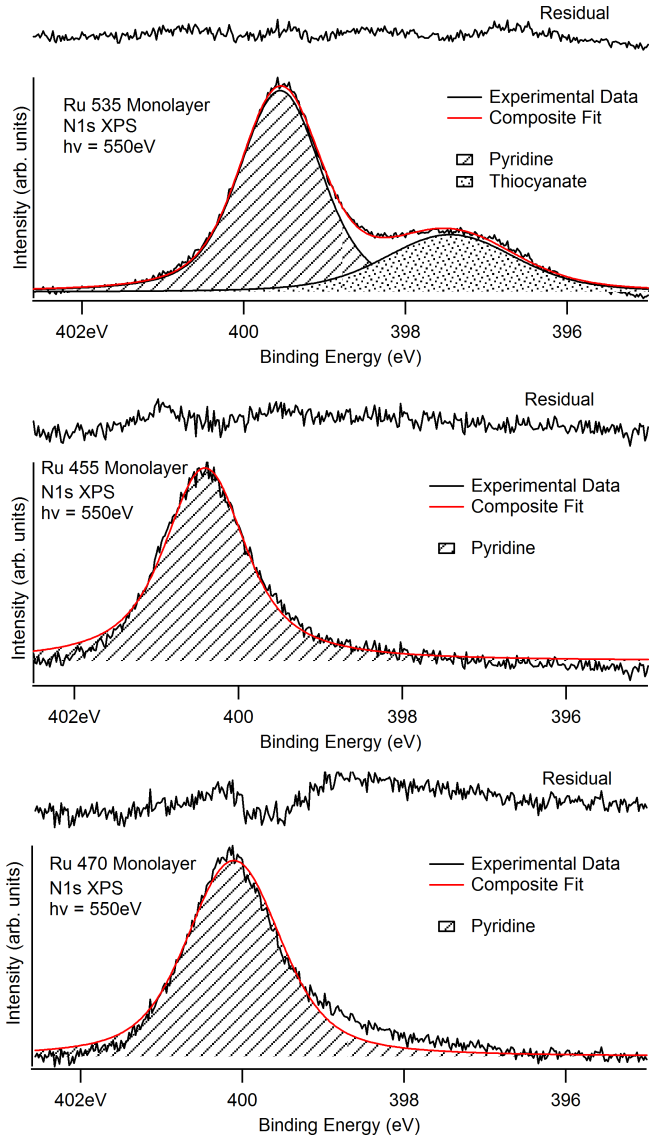

Figure 6.8: N 1*s* core-level photoemission spectra of monolayers of Ru 535 (top), Ru 455 (middle) and Ru 470 (bottom) on rutile TiO_2(110), measured using hν = 550 eV.

mission spectrum (all valence spectra are measured using a photon energy of hν=110 eV). The N 1*s* core level spectra of monolayers of all three dye complexes are dominated by the pyridine N peak, therefore this peak was used to place the NEXAFS on the common BE axis. Previous studies on the bi-isonicotinic acid ligand and on the Ru 535 dye complex have shown that the N 1*s* NEXAFS for these molecules are dominated by pyridine-like π* orbitals.[7, 117, 118]

The LUMO of Ru 535 is slightly broader than the LUMO orbitals for Ru 455 and Ru 470. The shoulder on the low binding energy side has previously been attributed to orbitals from the isothiocyanate ligands using DFT simulations showing orbitals localised on the isothiocyanate ligands at approximately the right energy. Further evidence is given by the absence of this feature in NEXAFS spectra of bi-isonicotinic acid.[7]

The lowest binding energy peak in the valence photoemission spectra corresponds to the highest occupied molecular orbital (HOMO). For each dye complex the HOMO is present within the substrate band gap which prevents back transfer of electrons from the substrate. The HOMO is located at a BE of 1.85 and 1.90 eV for the Ru 455 and Ru 470 dye complexes respectively. The HOMO of the Ru 455 and Ru 470 dye complexes are both located at higher BE than for Ru 535 (1.3 eV). After charge transfer from the molecules to the substrate has occurred this could create a larger potential to remove electrons from an attached water molecule. Optical absorption spectra of the dye complexes have maxima at photon energies corresponding to the energy gap between occupied and unoccupied levels. The lowest in energy of these maxima is attributed to the HOMO$\rightarrow$LUMO transition corresponding to a Ru(4d)$\rightarrow$bpy(π*)COOH transition.

In the present case where the unoccupied states are probed using N 1*s* NEXAFS a *core* exciton (bound electron-hole pair) is created, whereas in an optically excited system a *valence* exciton is created. The presence of a hole in the system shifts the unoccupied states to higher binding energy with respect to the ground state. The BE of the excitons, equivalent to the amount by which the unoccupied levels shift, is attributed to a combination of the Coulomb interaction between the hole and the excited electron and the rehybridization of the molecular states upon core or valence hole creation.[66] Comparing the HOMO-LUMO gap for optical excitation (2.3, 2.73 and 2.65 eV) to the HOMO-LUMO gap for the core-excited system (1.2, 1.1 and 1.4 eV), the difference in energy is 1.1, 1.6 and 1.3 $\pm$ 0.1 eV for the Ru 535, Ru 455 and Ru 470 dye complexes respectively. This is indicative of the energy difference between the N 1*s* core exciton and valence exciton BEs for the molecules. These values are consistent with the difference in BE found for pyridine (1.3 eV),[66] a molecule closely related to the bi-isonicotinic acid ligands of the dye complexes, especially concerning the chemical environment of

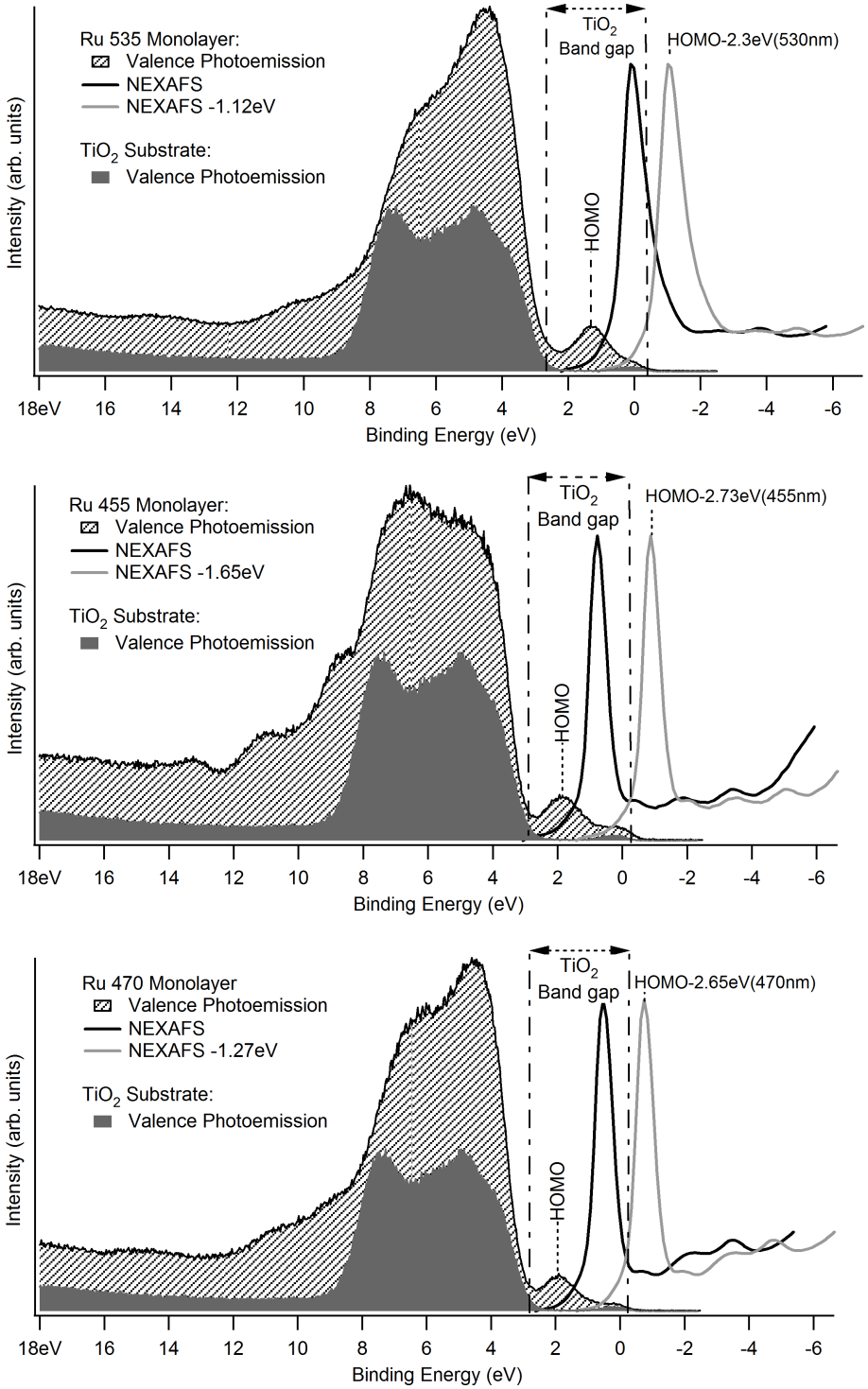

Figure 6.9: Valence band photoemission spectra of the clean substrate and of a monolayer of dye molecule, adjacent to a N 1*s* NEXAFS spectrum of the monolayer. The NEXAFS spectra are also shown shifted to align with the relevant optical HOMO-LUMO gap. The photoemission spectra were measured using hν = 60 eV. The NEXAFS spectra were taken over the photon energy range hν = 397-406 eV.

the nitrogen atoms being probed here. This suggests that the core and valence excitons are located on a similar part of the molecule.

Shifting the NEXAFS spectra of each dye complex into line with the optical HOMO-LUMO gap as shown in Figure 6.9, causes all three LUMOs to lie above the conduction band edge. In a real solar cell or water-splitting device this energetic overlap permits electron injection from the LUMO into the substrate for all of the dye complexes. The presence of a core exciton in the NEXAFS causes the LUMO of the core-excited systems to lie within the substrate band gap preventing charge transfer for this orbital. In the next section, electrons excited to the LUMO are used as a reference, allowing us to probe electron injection from those remaining unoccupied levels that lie above the conduction band edge.[68, 115]

6.3.3 Charge Transfer Dynamics

In water-splitting DSCs the initial step of the reaction is electron injection from the excited molecule into the substrate conduction band. RPES is used here to investigate molecule-to-substrate charge transfer. This technique enables us to quantify the delocalization of charge from unoccupied molecular orbitals to the substrate on the low femtosecond time scale, previously demonstrated for the bi-isonicotinic acid ligand and the Ru 535 molecule on TiO_2(110).[7, 115] This technique was described in detail earlier in Chapter 4.

The energy alignment diagrams in Figure 6.9 show that the LUMO of each of the dye complexes is capable of charge transfer when the dye is excited using visible light. The creation of a core-hole in RPES prevents the LUMO from being studied directly due to the LUMO lying within the TiO_2 band gap in the core-excited system. However, the LUMO, LUMO+2 and LUMO+3 of each dye complex are all thought to be located on the bi-isonicotinic acid ligands. Therefore it can be assumed that the coupling of these orbitals to the substrate and, therefore, the corresponding charge-transfer dynamics will be similar. The LUMO+2 and LUMO+3 orbitals of these dye complexes are in the same energy range as the substrate conduction band allowing us to obtain charge transfer data on these orbitals.

The core-hole clock implementation of RPES uses the fact that if charge transfer is occurring, it must be competing with the de-excitation of the excited state via resonant photoemission or resonant Auger. The time taken for de-excitation can also be described as the lifetime of the N 1*s* core hole. Here we calculate the electron injection time from the LUMO+2 and LUMO+3 orbitals of each dye complex where possible.

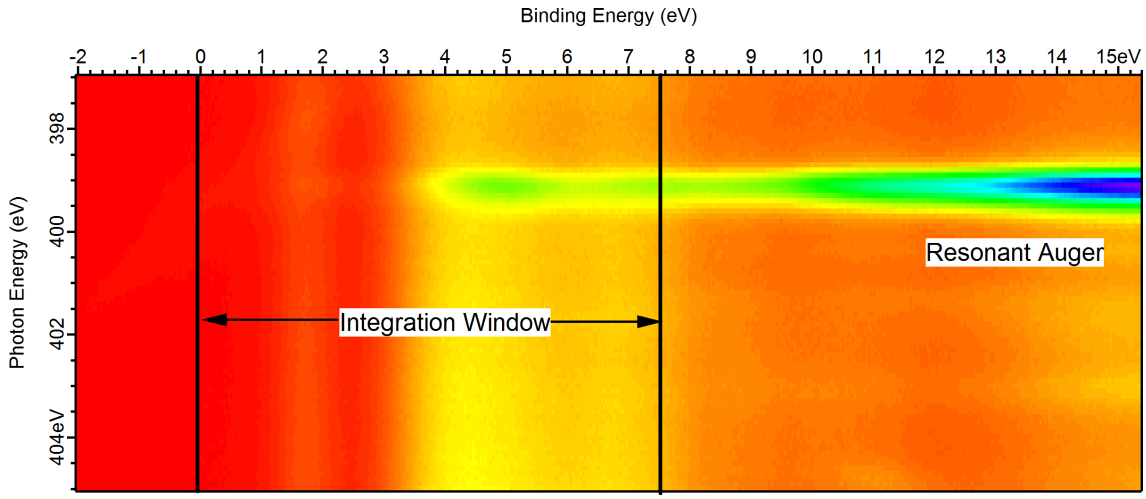

Figure 6.10: N 1*s* RPES spectrum of a monolayer of Ru 470 on rutile TiO_2(110) showing the BE integration window used to remove the Auger peaks.

The electron injection time τ_{EI} for electrons moving from the unoccupied level of the molecule adsorbed to the substrate to unoccupied substrate states is given by Eq. 6.3.1., the derivation of this equation is shown in Section 4.3.3.

$$\tau_{EI} = \tau_{CH} \frac{I^{mono}_{RPES} / I^{mono}_{NEXAFS}}{I^{multi}_{RPES} / I^{multi}_{NEXAFS} - I^{mono}_{RPES} / I^{mono}_{NEXAFS}} \tag{6.3.1}$$

The variables I^{mono}_{RPES} and I^{multi}_{RPES} represent the intensities of the unoccupied peak being studied in the monolayer and multilayer respectively. These values are each normalized by the total cross sections as provided by the NEXAFS intensities I^{mono}_{NEXAFS} and I^{multi}_{NEXAFS}. The variable τ_{CH} is the average $N1s$ core-hole lifetime which has been measured as 6 fs for the N_2 molecule.[119] The lifetime of the core-hole is dependent upon the environment of the atom. It is longest for atomic Auger transitions and shorter for molecular transitions depending on the electronegativity of the ligands.[120] Therefore the upper limit of the core-hole lifetime would be for atomic nitrogen which has previously been calculated at 7.5 fs.[120]

The experimental RPES data includes Auger peaks which need to be excluded from the charge transfer analysis. These peaks are removed by integrating over a selected BE window as shown in Figure 6.10 for both the multilayer and monolayer. Any peaks at the energies of the LUMO+2 and LUMO+3 resonances are due solely to resonant photoemission, as normal photoemission contributes a sloping background only. The LUMO+1 is not considered as it cannot be separated from the LUMO for these molecules.

The RPES and NEXAFS spectra are normalized to the intensity of the LUMO, the re-

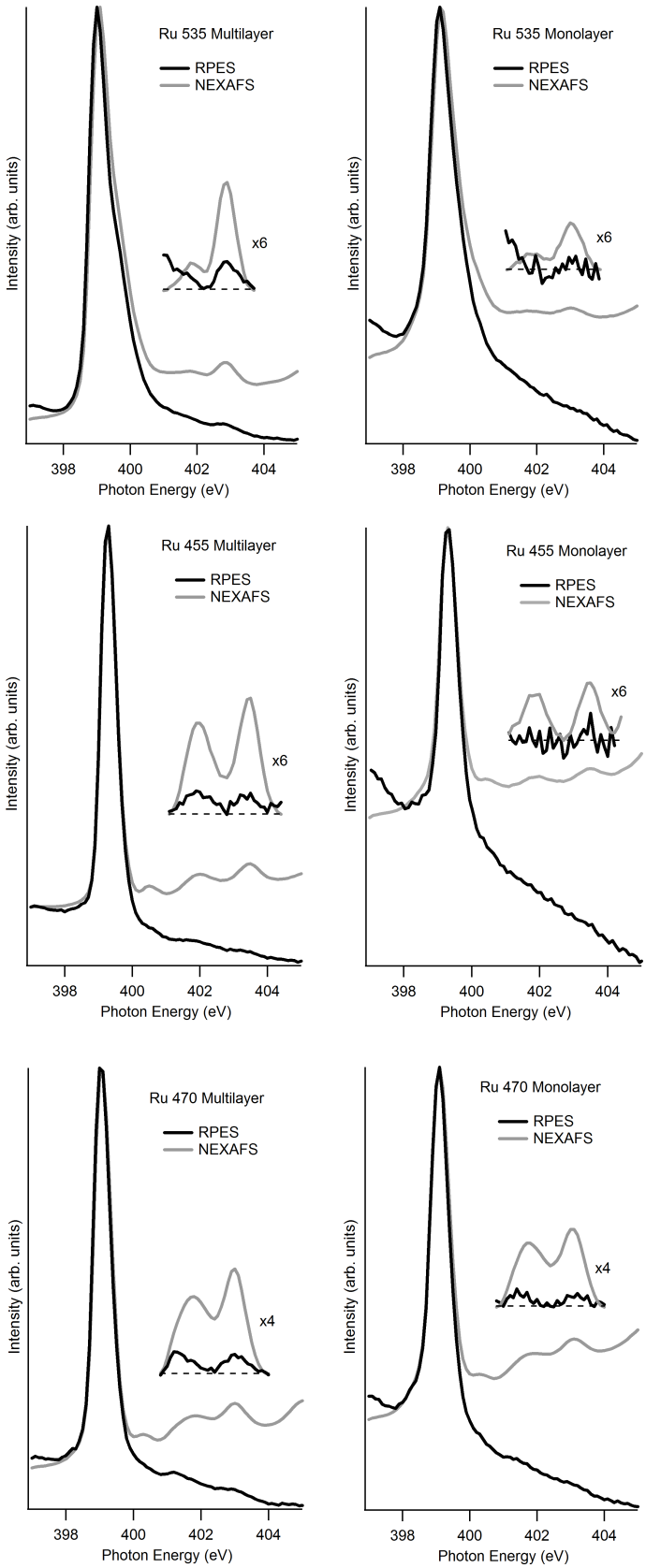

Figure 6.11: N 1*s* RPES and N 1*s* NEXAFS spectra of multilayers (left) and monolayers (right) of Ru 535 (top row), Ru 455 (middle row) and Ru 470 (bottom row). The RPES spectra are BE integrations over a range which excludes the Auger peaks. Also shown are magnifications of the LUMO+2 and LUMO+3 region.

sulting spectra are shown in Figure 6.11. In the NEXAFS spectra, the peaks represent the unoccupied levels' full intensities, whereas for RPES the LUMO has its full intensity but the other unoccupied levels may be depleted by charge transfer. For the multilayer it can be seen that the LUMO+2 and LUMO+3 peaks are smaller in the RPES than in the NEXAFS. Since no charge transfer to the substrate can occur in the multilayer this intensity reduction is attributed purely to matrix element effects due to the different techniques used.[116] For the monolayer RPES the peaks have been reduced further, in some cases down to the level of noise, indicating that charge transfer is occurring from these levels on the timescale of the core-hole lifetime.

The multilayer RPES spectrum of Ru 535 in Figure 6.11 shows a very broad LUMO peak compared to the multilayer RPES spectra of the Ru 455 and Ru 470 molecules. This has been attributed to overlapping signals coming from the two different types of nitrogen atoms found in Ru 535. In Ru 455 and Ru 470 there is only a single major chemical environment for the nitrogen atoms. In the Ru 455 and Ru 470 multilayer RPES spectra it is possible to see a distinct LUMO+1 peak, which is not possible in the Ru 535 spectrum due to the broad peak.

For the Ru 535 and Ru 455 spectra there are monolayer RPES peaks that have no discernible peak at the same photon energy as the corresponding peak in the NEXAFS spectrum. For these peaks the level of noise is taken as an upper limit for the intensity of any peak that might be present. This is then used to calculate an upper limit for the charge transfer time according to Eq 6.3.1, shown for each molecular orbital studied in Table 6.2. These values are in agreement with the upper limit on the time scale for charge transfer of both Ru 535 and the bi-isonicotinic acid ligand on TiO_2, which have previously been found to be 16 fs and 3 fs respectively.[7, 115] The reduction of the Ru 535 LUMO+3 upper limit on the charge transfer timescale is attributed to a better signal to noise ratio in the current experiment.

Various different experimental techniques have previously been used to study Ru 535 on TiO_2 such as laser pump-probe techniques which have found instrument limited charge transfer timescales of 50 fs.[101, 121] DFT simulations have also been performed on this system examining the charge transfer process which predict charge transfer time scales on the order of 10 fs.[122] The results for the charge transfer timescale for the molecules studied in these experiments are consistent with the results obtained from these other types of experiments.

The Ru 455 and Ru 470 dye complexes show charge transfer timescales on the same order of magnitude as the Ru 535 complex, however all of the orbitals studied on these complexes appear to have slower charge transfer timescales than the Ru 535 LUMO+3.

The Ru 470 complex appears to be the least efficient at charge transfer, this could be explained by the different bonding geometry on the rutile TiO_2(110) surface that Ru 470 complex appears to have compared to the Ru 535 and Ru 455 complexes as suggested by earlier DFT results. This geometry may be less efficient for charge transfer as it may not provide as much chemical coupling to the surface as the bonding geometries adopted by Ru 535 and Ru 455 using a single bi-isonicotinic acid ligand.

Table 6.2: Table of RPES/NEXAFS ratios for multilayer and monolayer coverages of dye molecules and the calculated upper limit on charge transfer timescale for each orbital studied.

Dye molecule	Orbital	Multilayer RPES/NEXAFS	Monolayer RPES/NEXAFS	Upper limit on charge transfer timescale (fs)
Ru 535	LUMO+3	0.259	0.170	12 ± 1
Ru 455	LUMO+2	0.252	0.190	18 ± 1
Ru 470	LUMO+2	0.198	0.155	21 ± 1
Ru 470	LUMO+3	0.168	0.124	17 ± 1

For resonant photoemission to occur following core excitation, the occupied and unoccupied orbitals involved must have some interaction. The largest probability for resonant photoemission occurs when both of the electrons involved in the transition are located on the same atom, specifically the site of the core-hole. Resonant photoemission is in essence a special type of Auger decay and whilst interatomic Auger transitions can occur,[123] the rates of these events are negligible in all but the lowest energy Auger processes.

In these experiments resonant photoemission requires some degree of overlap between the HOMO, LUMO and the core-excited atom, however in a real DSC only an overlap between the HOMO and LUMO is required for photoexcitation between the states. Figure 6.12 shows that the calculated HOMO and LUMO of the Ru 455 dye complex have some overlapping spatial distribution on the central ruthenium metal ion which facilitates photoexcitation between the two orbitals. The Ru 470 dye complex appears to show little spatial overlap between the calculated HOMO and LUMO orbitals which may reduce the efficiency of this dye complex as a DSC.

6.4 Summary

UHV electrospray deposition has been used to deposit monolayers and multilayers of Ru 455, Ru 535 and Ru 470 dye complexes on the rutile TiO_2(110) surface *in situ*.

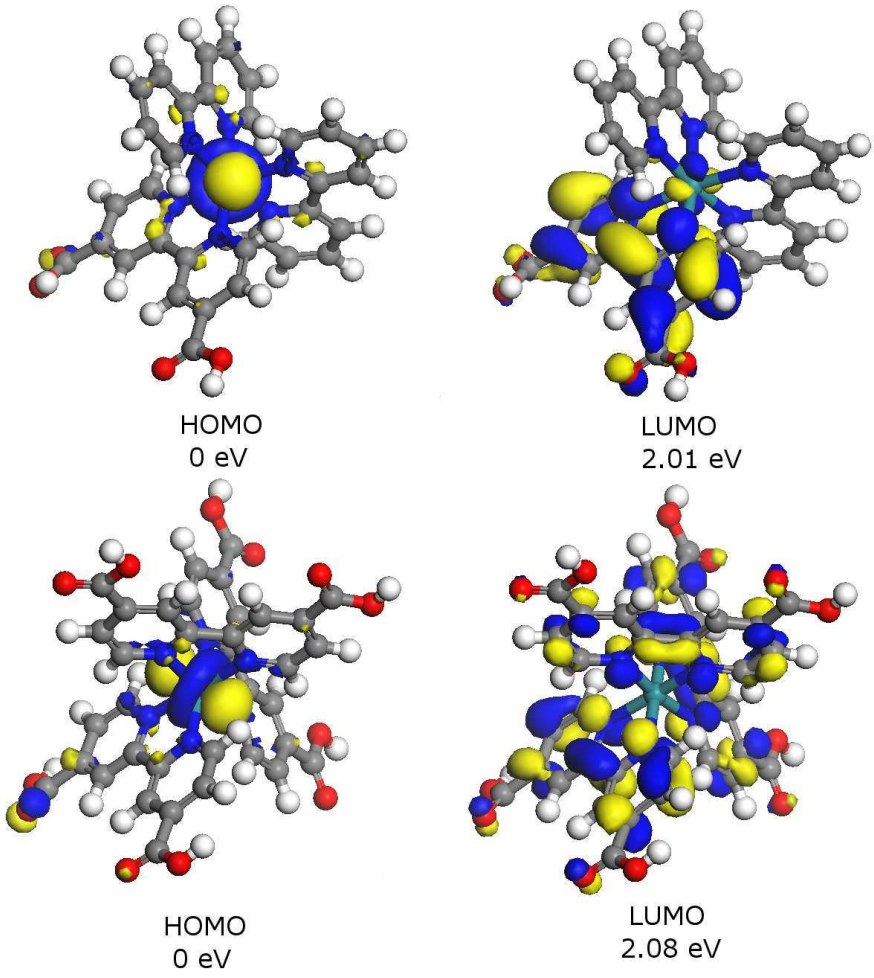

Figure 6.12: DFT calculations showing electron orbitals of a geometry-optimized free Ru 455 molecule (top) and Ru 470 molecule (bottom) together with calculated orbital energies.

Photoemission spectroscopy has been used to characterize the core and valence levels of the system, which were used to deduce the bonding geometry of each dye complex on the rutile TiO_2(110) surface. We find that for all three dye complexes it is most likely that two carboxylic acid groups deprotonate so that their O atoms bond to Ti atoms of the substrate surface. The Ru 470 dye complex appears to adopt a different bonding geometry to the Ru 535 and Ru 455 complexes, using two different ligands to bond to the surface instead of just one.

The energetic alignment of the system was determined by placing the valence photoemission and N 1*s* NEXAFS of a monolayer of each dye complex onto a common BE scale. The bandgap of TiO_2(110) was aligned using the valence photoemission of the clean substrate. The optical absorption maximum for each dye complex was attributed to the HOMO→LUMO transition in a working solar cell. This was used to compare the energetics as they would appear for photoexcitation from the valence band (as occurs in working DSCs) with those found for photoexcitation from the N 1*s* core level, for which the unoccupied levels appear at higher BE. This comparison allowed quantification of the difference in BE of a core and valence excitation for each dye complex system, found to be 1.6 and 1.3±0.1 eV. for the Ru 455 and Ru 470 dye complexes respectively.

The core-hole clock implementation of RPES was used to find that the LUMO+2 and LUMO+3 orbitals of each dye complex have upper limits on the timescale of charge transfer in the range of 12-21 fs. In agreement with previous studies of Ru 535, bi-isonicotinic acid and related molecules on TiO_2, which found charge transfer to occur on the femtosecond timescale. It is thought that the studied orbitals and the LUMO of each dye complex are all located on the bi-isonicotinic acid ligands, so electron injection in valence excited systems is expected to occur in a similar time scale. The Ru 470 monolayer RPES peaks are still clearly visible suggesting that this dye complex is the least efficient molecule at charge transfer studied here, possibly due to the different bonding geometry adopted by this molecule on the surface.

The valence band photoemission spectra show that the HOMO of the Ru 455 and Ru 470 dye complexes occur at higher BE than the Ru 535 dye complex. The difference between the BEs is attributed to the difference in electron densities on the central ruthenium ion, which is caused by the difference in electronegativity of the attached ligands. In a water-splitting dye complex the potential to remove electrons from a water molecule is created by a hole in the HOMO. Having the HOMO at higher BE causes a larger potential which should be more effective at removing electrons from the water molecule.

CHAPTER 7

Dipyrrin-based dye complexes on TiO_2(110)

7.1 Introduction

In the last chapter the dye complexes studied used bi-isoniotinic acid ligands to attach to the TiO_2 surface. These ligands have been extensively studied and are known to be efficient at charge transfer.[7] By studying other types of ligands we may discover molecules that have different adsorption geometries on the TiO_2 surface. This may help to determine some of the underlying factors that affect the efficiency of charge transfer. This is the reason why we chose to study dipyrrin-based ligands which have a significantly different chemical structure to bi-isonicotinic acid ligands.

In this chapter several dye complexes containing dipyrrin-based ligands have been studied adsorbed onto a rutile TiO_2 substrate. In Chapter 6 the dye complexes that were studied used bi-isonicotinic acid ligands to attach the molecules to the substrate. Bi-isonicotinic acid contains carboxylic acid groups which can deprotonate to form chemical bonds with the TiO_2 substrate.[7, 14, 100] By bonding to the surface the dye complexes are kept in close contact with the substrate which provides a suitable spatial overlap of orbitals from the molecule and the substrate for the charge transfer process to occur efficiently.[7, 115, 122] Currently most dye complexes in DSCs use bi-isonicotinic acid ligands as the anchor ligand.[5, 22, 124]

An advantage of using bi-isonicotinic acid ligands in a sensitizing dye complex for a dye-sensitized solar cell is that the bi-isonicotinic acid ligands have a large conjugated π system which makes them efficient at absorbing incident photons. By increasing the size of the conjugated π system it may be possible to improve the light harvesting properties of a dye complex without significantly affecting its charge transfer proper-

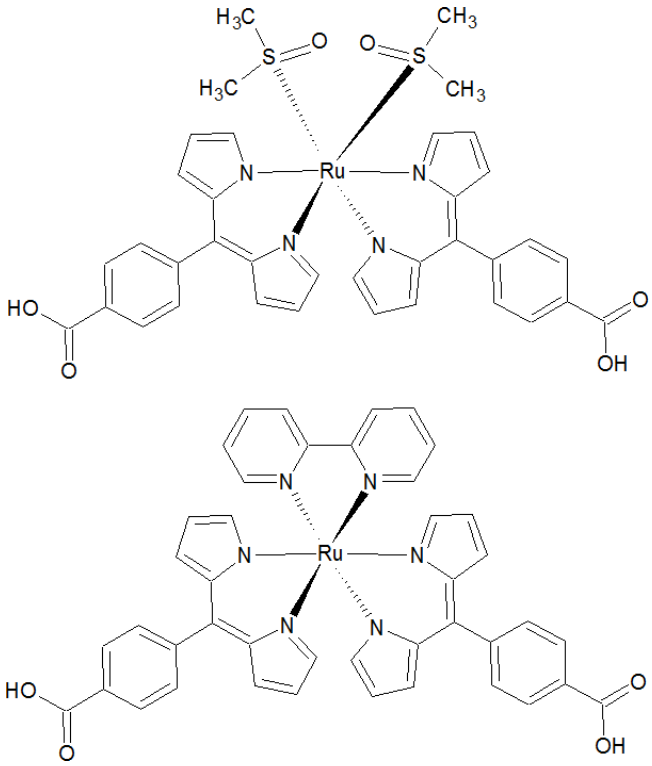

Figure 7.1: Chemical structures of the two dipyrrin complexes studied in this investigation, PY1 (top) and PY2 (bottom).

ties. Dipyrrin-based ligands contain a larger conjugated π system than bi-isonicotinic acid molecules and can also be functionalised with carboxylic acid groups to allow them to bond with a TiO_2 surface.[125, 126]

Two dipyrrin-based dye complexes were studied; PY1 (bis(5-(4-carboxyphenyl)-4,6-dipyrrin)bis(dimethylsulfoxide)Ruthenium(II)) and PY2 (bis(5-(4-carboxyphenyl)-4,6-dipyrrin)(2,2'-bipyridine)Ruthenium(II)). The chemical structures of the two dye complexes are shown in Figure 7.1. The dimethylsulfoxide (DMSO) groups in the PY1 dye complex are capable of bonding to the metal centre of the complex either through their oxygen atom or their sulphur atom. Our DFT calculations suggest that the sulphur atom in each group bonds to the metal core.

The dipyrrin ligands in these molecules contain carboxylic acid functional groups, which will most likely deprotonate on adsorption to the TiO_2 surface as previously seen in dye complexes containing bi-isonicotinic acid ligands in Chapter 6. Bi-isonicotinic acid ligands have previously been found to deprotonate to form a 2M-bidentate structure on the rutile TiO_2(110) surface both in their uncomplexed form and as part of a larger dye complex.[7, 14] Molecules with similar structures to bi-isonicotinic acid have similar adsorption geometries on the TiO_2 surface.[109–111]

The size of the dipyrrin ligands may allow both ligands to bond to the surface at the

same time. This can be determined by monitoring the amount of deprotonation in the monolayer O 1*s* XPS spectra. If both dipyrrin ligands can bond to the surface then the efficiency of charge transfer may be improved as there may be more spatial overlap between the molecule and substrate orbitals.

The core-hole clock implementation of resonant photoemission spectroscopy (RPES) has revealed charge transfer from an adsorbed N3 molecule to a TiO_2 substrate can take place within a 12-16 fs timescale as seen in Chapter 6 and previous experiments.[7] It is likely that the dipyrrin and bi-isonicotinic acid based dye complexes will have reasonably similar timescales for charge transfer due to similarities in their chemical structures. By comparing charge transfer timescales between the different types of molecule we hope to determine if dipyrrin-based dye complexes will be useful in both photovoltaic and water-splitting DSC devices.

If a ruthenium dye complex with dipyrrin-based ligands proves to be an efficient light harvesting molecule for use in photovoltaic DSCs, then this type of complex could also be adapted to be used as the charge transfer centre of a multi-centre water-splitting dye complex. The charge transfer centre is responsible for bonding the dye complex to the substrate, absorbing photons of visible light and subsequently for electron transfer from the adsorbed molecules to the substrate. This charge transfer process creates the potential to oxidise a water molecule attached to the reaction centre of the multi-centre complex. The oxidation process creates H^+ ions which migrate towards the cathode where they recombine with the electrons initially transferred into the substrate and produce hydrogen molecules.[31] These hydrogen molecules could potentially become a portable source of large quantities of energy.[23, 24, 26–28] If the water-splitting process could be carried out with a DSC architecture then this could prove to be a cost-effective, environmentally friendly method of generating a potent fuel.

Dye complexes were deposited onto a rutile TiO_2 substrate at both monolayer and multilayer coverages using *in situ* ultra high vacuum electrospray deposition. The adsorbed dye molecules in this study were examined using X-ray photoemission spectroscopy (XPS) in order to explore their bonding to the rutile TiO_2(110) surface. NEXAFS and DFT are used to study the energetic and spatial distributions of orbitals relevant to the charge transfer process. The core-hole clock implementation of RPES is used to calculate upper limits on the timescale of electron injection from the adsorbed molecules to the TiO_2 substrate. These results should help to determine if dipyrrin-based dye complexes are suitable for use in DSC devices.

7.2 Method

Experiments were carried out at the bending magnet beamline D1011 and undulator beamline I311 at MAX-lab, Sweden. The end stations are both equipped with a Scienta SES-200 electron analyser. The sample was orientated at normal emission to the analyser corresponding to 40 ° at D1011 and 54 ° from normal incidence at I311.

The dye complexes studied in this investigation were synthesised using a modified literature method. The experiments were performed using a single crystal rutile TiO_2(110) substrate (Pi-Kem, UK), the samples were annealed using an electron beam heater at D1011 and a pyrolytic boro nitride heater at I311. The sample was prepared by sputtering and annealing as described in Section 6.2. The surface was determined clean when there were negligible C 1*s* and K 2*p* core-level signals and a single Ti^{4+} oxidation state in the Ti 2*p* spectrum.

The dye molecules were deposited using an *in situ* UHV electrospray deposition source (MolecularSpray, UK), from a solution of $\sim$ 5 mg of dye in 200 ml of a pure methanol solution for both dye complexes. The deposition method was previously described in Section 6.2. The principles underlying electrospray deposition were discussed in Chapter 5. A UHV gate valve was used to seal off the analysis chamber from the electrospray apparatus between depositions. With the valve open but the needle voltage turned off and thus no electrospray process occurring, the pressure in the preparation chamber was $\sim 5 \times 10^{-8}$ mbar. With the voltage turned on, the preparation chamber pressure rose to $\sim 4 \times 10^{-7}$ mbar, the additional pressure being due to residual solvent molecules in the beam.

For the electron spectroscopy data, the total instrument resolution ranges from 65-195 meV. XPS spectra of the molecules on the TiO_2 crystal have been calibrated to the substrate O 1*s* peak at 530.05 eV,[105] and a Shirley background removed before curve fitting using Voigt functions.

NEXAFS and RPES spectra were taken over the N 1*s* absorption edge and were measured using the electron analyzer. For NEXAFS spectra the nitrogen Auger yield was used whilst for RPES spectra the valence band photoemission was monitored. In this experiment beam damage was monitored by taking NEXAFS spectra before and after an RPES spectrum and comparing the appearance of the peaks above the LUMO. These spectra revealed limited beam damage occurred over the duration of an RPES spectrum. Multiple RPES spectra were taken for each coverage in different positions and combined to produce the RPES spectra shown in this paper.

Density functional theory simulations (DFT) calculations were carried out as an aid to

interpreting the experimental data. Geometry optimizations were performed on free molecules of each dye complex using Dmol^3 at the DFT-generalized gradient approximation level (DFT-GGA) with the Perdew-Burke-Enzerhof (PBE) functional.[63, 64, 106] The optimized structures were then used to calculate the molecular orbitals for each molecule.

7.3 Results and Discussion

7.3.1 Bonding geometry

The samples used for the following spectra are classed as either *monolayer* or *multilayer*. Here a monolayer is defined as a sample having the vast majority of molecules directly adsorbed to the surface and a multilayer as having a film of molecules thick enough that the majority of photoelectrons in XPS come from molecules above the first adsorbed layer. The method for determining the surface coverage was described in Chapter 6. Using the O 1*s* XPS spectra the multilayer is estimated to be about two to three layers thick for each dye complex. The binding energies (BEs) of the peaks discussed are summarised in Table 7.1.

Figure 7.2 and Figure 7.3 show the O 1*s* monolayer and multilayer spectra of the PY1 and PY2 dye complexes on rutile TiO_2(110) respectively. For both of the dye molecules the monolayer spectra are dominated by the TiO_2 substrate oxygen peak. The two peaks at higher binding energy are due to the oxygen atoms in the carboxylic acid groups on the dipyrrin-based ligands of each molecule.

Previous studies of bi-isonicotinic acid and N3 have shown deprotonation of the carboxylic acid groups on adsorption to TiO_2 to form a 2M-bidentate structure.[7, 14] This is a common bonding arrangement for pyridine based molecules with carboxylic acid groups on the TiO_2 surface.[109–111] The carboxylic acid group in the dipyrrin-based ligands studied here has a similar chemical environment to a carboxylic acid group in a pyridine-based ligand. This most likely means that the mechanics of adsorption to the surface will be similar for these two types of ligand. After deprotonation of a carboxylic acid group the two oxygen atoms share an electron and are chemically equivalent. The BE of this oxygen species is similar to that of the carbonyl oxygen atom in isolated molecules so the two species are unresolvable from each other in the XPS spectra.[14] In Figures 7.2 and 7.3 there is little evidence of a hydroxyl oxygen peak in the monolayer spectra for either molecule. This suggests that each molecule bonds to the surface using both of the two available carboxylic acid groups on both of the dipyrrin ligands

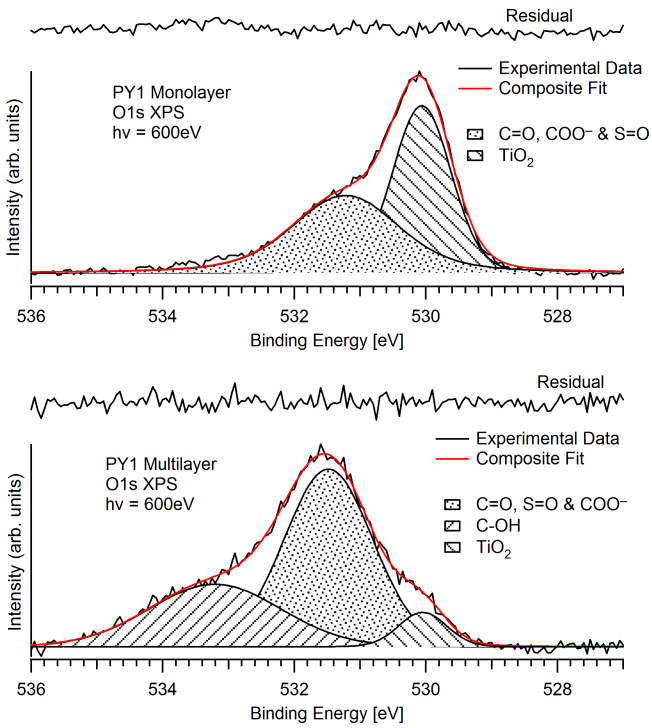

Figure 7.2: O 1*s* core-level photoemission spectra of a monolayer of PY1 (top) and a multilayer of PY1 (bottom) on rutile TiO_2(110), measured using hν = 600 eV.

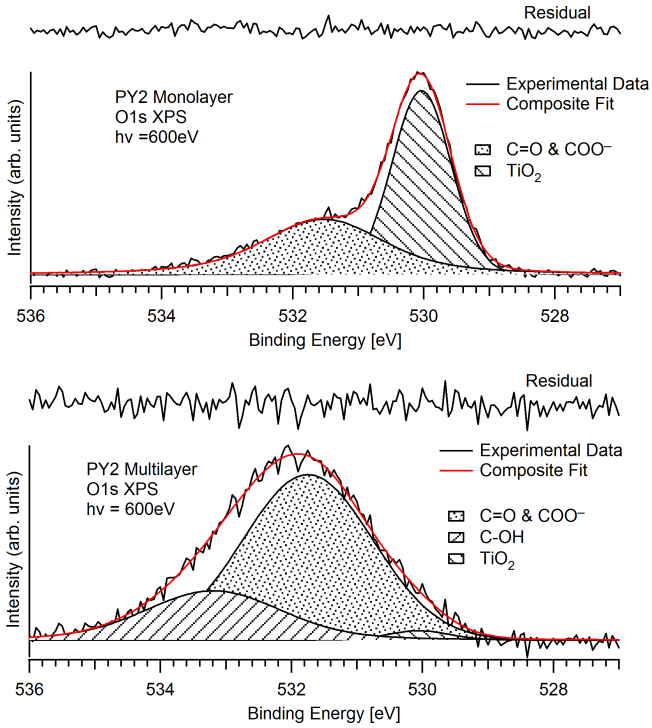

Figure 7.3: O 1*s* core-level photoemission spectra of a monolayer of PY2 (top) and a multilayer of PY2 (bottom) on rutile TiO_2(110), measured using hν = 600 eV.

Table 7.1: Photoelectron BEs (eV) for each molecule, the peaks are calibrated to the substrate O 1*s* peak at 530.05 eV.

		PY1	PY2
O 1*s*	TiO_2	530.05	530.05
	Monolayer C=O and COO^-	531.3	531.5
	Multilayer C=O and COO^-	531.5	531.7
	Multilayer C-OH	533.3	533.2
C 1*s*	Dipyrrin	284.7	285.4
	Bipyridine	...	285.4
	Dimethylsulfoxide	283.7	...
	Carboxyl	287.9	287.7
Ru 3*d*		281.1	281.0
N 1*s*	Negative Pyrolle	398.7	398.8
	Neutral Pyrolle/Bipyridine	400.0	400.1
	Shake-up	401.5	401.4
S 2*p*	Monolayer Dimethylsulfoxide	166.7	...
	Multilayer Dimethylsulfoxide	166.7	...
Valence band	HOMO	2.0	1.4
N 1*s* NEXAFS			
Unshifted	Dipyrrin LUMO	0.4	0.9
	Bipyridine LUMO		0.4
Aligned to optical data	Dipyrrin LUMO	-0.4	-0.4
	Bipyridine LUMO		-0.55

simultaneously.

The bottom spectra in Figures 7.2 and 7.3 show O 1*s* XPS spectra of multilayers of each dye complex. Both molecules contain two carboxylic acid groups which are expected to have an equal number of deprotonated and protonated oxygen atoms. The PY1 dye complex also has an oxygen atom within each of its dimethylsulfoxide (DMSO) groups, which has a similar chemical environment to the deprotonated oxygen atoms in the carboxylic acid groups and therefore the two environments cannot be resolved in the XPS data. Therefore a 2:1 and a 1:1 intensity ratio of deprotonated to protonated oxygen peaks is expected for the PY1 and PY2 dye complexes respectively. The experimental deprotonated:protonated intensity ratio for the multilayer oxygen peaks is 2:1 for PY1 and 3:1 for PY2. Previously deprotonation of carboxylic acid groups in dye complexes based on bi-isonicotinic acid ligands was observed using the same experi-

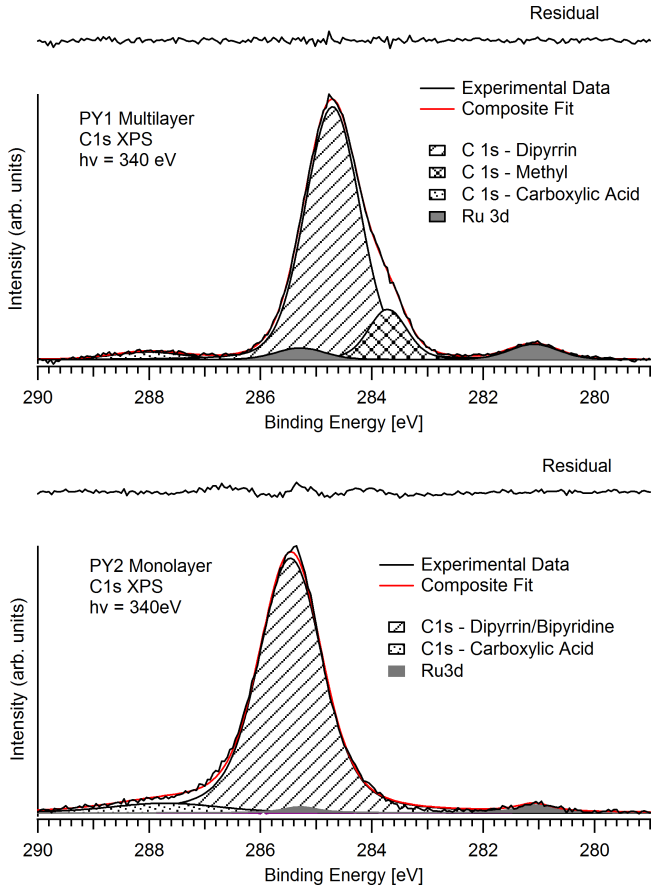

Figure 7.4: C 1*s* and Ru 3*d* core-level photoemission spectra of monolayers of PY1 (top) and PY2 (bottom) adsorbed on rutile TiO_2(110), measured using hν = 340 eV.

mental method in Chapter 6. This effect has been attributed to charge balance effects due to the positively charged ruthenium core.

Figure 7.4 shows the C 1*s* and Ru 3*d* XPS spectra of monolayers of each dye complex. Both spectra are dominated by a peak due to the carbon atoms in the dipyrrin ligands and both spectra have a peak at higher BE corresponding to the carbon atoms in the carboxylic acid groups. The spectrum for PY1 also contains a peak corresponding to the carbon atoms in its dimethylsulfoxide groups and the spectrum for PY2 shows only a single major peak for the aromatic rings. This suggests that the chemical environments of carbon atoms in the dipyrrin and bipyridine ligands are indistinguishable in the XPS spectra. There are also two peaks due to the central ruthenium ion as the Ru 3*d* state is a doublet state with a spin orbit splitting of 4.2 eV.[112] The lower BE Ru $3d_{5/2}$ peak is present in both spectra at ~281 eV. This BE is approximately 1 eV higher than metallic ruthenium,[112] which is consistent with the Ru^{2+} oxidation state of the metal centre as previously seen in other ruthenium based dye complexes.[7]

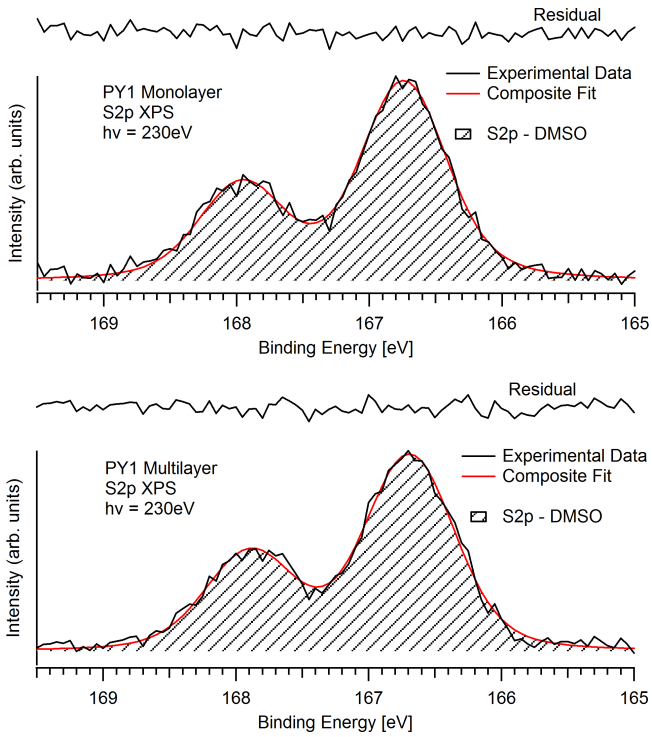

Figure 7.5: S 2*p* core-level photoemission spectra of a monolayer of PY1 (top) and a multilayer of PY1 (bottom) adsorbed on rutile TiO_2(110), measured using hν = 230 eV.

The PY1 dye complex also contains a sulphur atom in its dimethylsulfoxide groups, S 2*p* XPS spectra show a single spin-orbit doublet at both monolayer and multilayer coverages of the PY1 complex. This means that the sulphur atoms are present only in a single chemical environment. This makes it unlikely that any sulphur atoms are bonded to the TiO_2 surface in monolayer coverages. This is in contrast to the sulphur atoms in the isothiocyanate groups of the N3 dye complex.[7] In the isothiocyanate groups of N3 the sulphur atoms are not fully coordinated, allowing them the possibility of bonding to the TiO_2 surface. In PY1 however, the sulphur atoms have methyl groups which would have to be detached to allow the sulphur atoms to attach to the surface.

Figure 7.6 shows the N 1*s* XPS spectra of monolayers of each dipyrrin complex, the multilayer spectra are not shown as they appear similar to the monolayer spectra. The largest peak for both dye complexes is located at the lowest binding energy, this corresponds to negatively charged nitrogen atoms in the dipyrrin ligands. The next most intense peak corresponds to neutral nitrogen atoms in the dipyrrin and bipyridine ligands and the least intense peak at highest binding energy could potentially be a shake-up feature as seen in previous experiments on related molecules.[105] The structure of the dipyrrin ligands can be seen in Figure 7.1, the diagram shows that the nitrogen

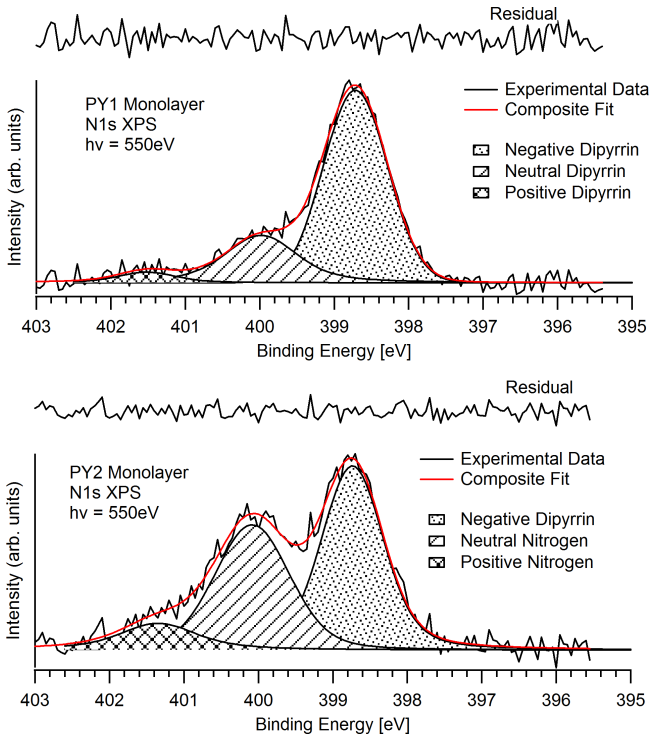

Figure 7.6: N 1*s* core-level photoemission spectra of a monolayer of PY1 (top) and a monolayer of PY2 (bottom) adsorbed on rutile TiO_2(110), measured using hν = 550 eV.

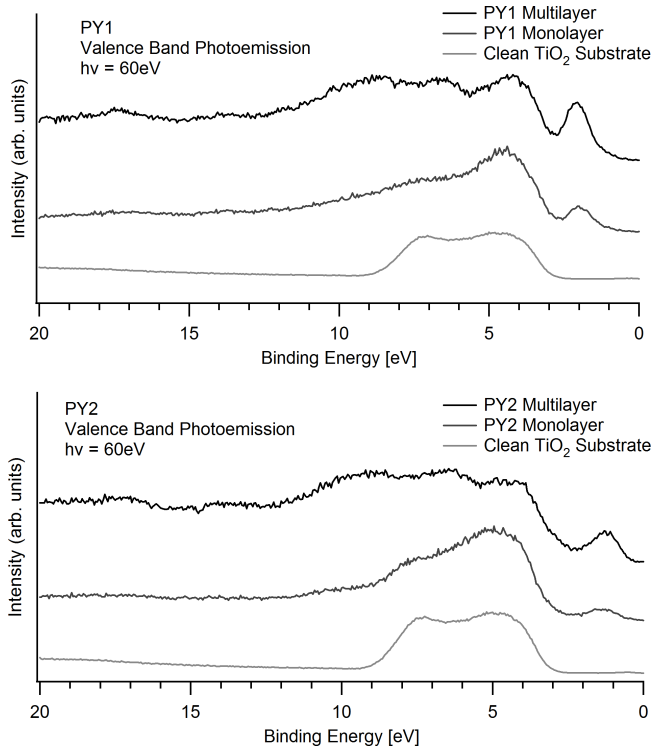

Figure 7.7: Valence band photoemission spectra on different coverages of PY1 (top) and PY2 (bottom) adsorbed on rutile TiO_2(110), measured using hν = 60 eV.

atoms in the dipyrrin ligands have two possible environments. The first is where the nitrogen has two single chemical bonds and is negatively charged and the second is where the nitrogen atom has a double and a single chemical bond and is neutral. From the chemical structure of the dipyrrin ligands a 1:1 ratio of neutral:negatively charged nitrogen atoms is expected and resonance would make their BEs equivalent, however the intensity ratio is 1:5 for the PY1 dye complex. The PY2 dye complex also has nitrogen atoms within the bipyridine ligand which remain neutral. The expected intensity ratio of neutral:negatively charged nitrogen atoms is 2:1 for this dye complex, however experimental data gives the intensity ratio as 2:3. The proximity of the nitrogen atoms to the positively charged ruthenium core might increase the local electron density on the nitrogen atoms and prevent resonance. This could manifest itself in the photoemission spectra as the separation of the neutral and negatively charged nitrogen peaks and the higher intensity of the negatively charged nitrogen peak as seen in the experimental data.

Figure 7.7 shows valence band photoemission spectra of monolayer and multilayer coverages of each dye complex as well as a valence band spectrum of the clean TiO_2 substrate for comparison. At higher coverages the valence band peaks due to the sub-

strate are obscured by peaks from the molecules adsorbed to the surface, this gives the multilayer valence band spectra a different appearance. The lowest BE peak in the valence band spectra of the monolayer covered surfaces corresponds to the HOMO of the adsorbed molecules, there is another peak at lower BE but this has been assigned to defects in the TiO_2 surface. The HOMO of the dipyrrin molecules appear to have a greater intensity compared to peaks from the substrate in the valence band than for bipyridine based dye complexes as seen in Chapter 6.[7] The extra intensity means that more electrons may be capable of being optically excited from the HOMO to the LUMO if the complex is used in a solar cell device.

In order to determine the most energetically favourable bonding geometry of the molecules to the surface DFT calculations were carried out on a range of different bonding geometries. Using the O 1*s* XPS spectra from the previous section the molecules were attached to the surface using both of the available carboxylic acid groups on the dipyrrin ligands. The molecules were geometry optimised on the surface and then the lowest energy geometry.

Figure 7.8 shows several possible bonding geometries of the PY2 dye complex on the rutile TiO_2(110) surface. The lowest energy bonding geometry is shown in Figure 7.8a). In this structure the oxygen atoms in the carboxylic acid groups are attached to titanium atoms in rows separated by a row of titanium atoms which are not involved in bonding to the molecule. Calculations where the molecules were bonded to adjacent titanium rows or where the bonded rows were separated by additional non-bonded titanium rows showed a significant increase in energy, the optimized geometries of these structures are shown in Figures 7.8b) and 7.8c) respectively. It is likely that the PY1 complex will adopt the same bonding geometry on the rutile TiO_2(110) surface, as the complex contains the same anchor ligands and the photoemission data shows that the DMSO groups do not bond to the TiO_2 surface.

7.3.2 Energy level alignment

An example of a PY2 NEXAFS spectrum is shown in Figure 7.9 to show how the PY2 peaks were labelled. Peaks A, C and D are attributed to the dipyrrin-based LUMO, LUMO+2 and LUMO+3 orbitals respectively, peak B is assigned to the bipyridine based LUMO with a small contribution from the dipyrrin-based LUMO+1. The PY1 NEXAFS peaks were assigned in a similar fashion but without the bipyridine-based LUMO. Spectra representing the occupied and unoccupied states of monolayers of each dye complex have here been placed on a common BE scale as shown in Figures 7.10 and 7.11, following the procedure outlined in Section 4.2. This procedure has previously

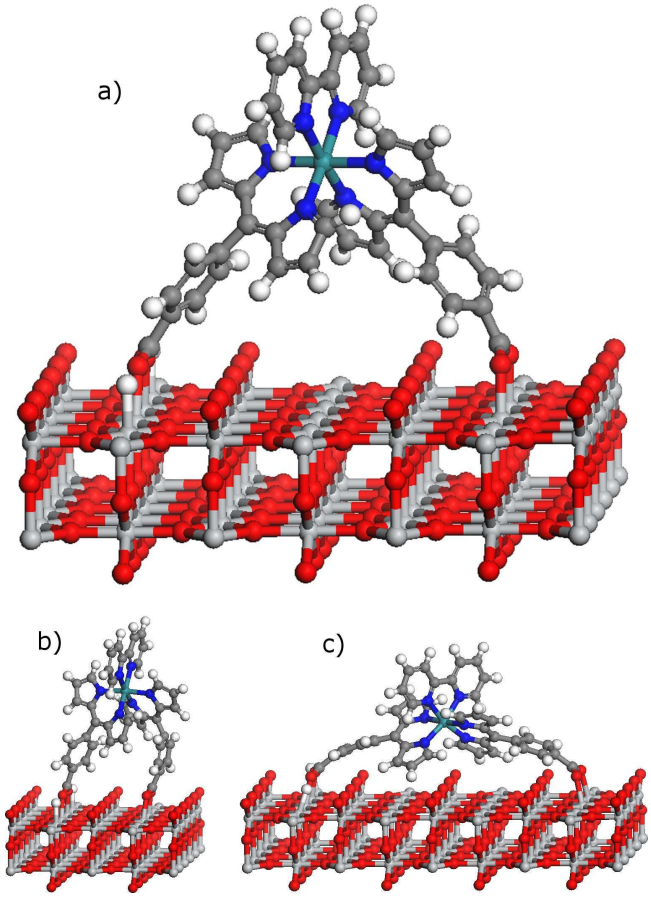

Figure 7.8: Different possible bonding geometries of a PY2 molecule on a rutile TiO_2(110) surface. These structures were geometry optimised using DFT. Structure a) is the lowest energy bonding geometry and has the dipyrrin ligands attached to rows of titanium atoms separated by an additional non-bonded row. Structure b) has adjacent rows of titanium atoms bonded to the molecule and structure c) has two rows of non-bonding titanium rows separating the rows of bonding titanium atoms. The atoms in the diagram are oxygen (red), titanium (light grey), carbon (dark grey), hydrogen (white), nitrogen (blue) and ruthenium (turquoise)

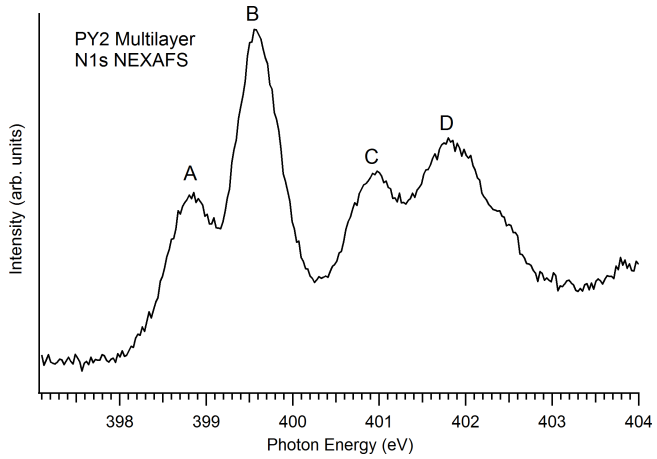

Figure 7.9: N 1*s* NEXAFS spectrum of a multilayer of PY2 with the peaks labelled A-D, peak A is the dipyrrin-based LUMO, B is the bipyridine-based LUMO, C is the dipyrrin-based LUMO+2 and D is the dipyrrin-based LUMO+3. The NEXAFS spectrum were taken over the photon energy range hν = 397.3-404.3 eV.

been performed on monolayers of N3.[7] The resulting energy level alignment diagrams can be used to identify the potential charge transfer processes that can occur in the dye complexes.[113–116]

Figures 7.10 and 7.11 show the N 1*s* NEXAFS and valence photoemission spectra for a monolayer of each dye complex along with the clean substrate valence photoemission spectrum. The N 1*s* core level photoemission spectra showed several nitrogen peaks for both complexes. The largest intensity nitrogen peak for both complexes was attributed to nitrogen atoms in the dipyrrin ligands with an effective negative charge, the next largest peak was located at higher BE and was attributed to neutral nitrogen atoms in the dipyrrin ligands (and the nitrogen atoms in the bipyridine ligand in PY2) and the lowest intensity peak at the highest BE was attributed to a shake-up feature. It is also possible that this is evidence of molecular damage from deposition. The dominant negative dipyrrin peak has been used to place the NEXAFS spectrum onto the BE scale for both complexes. For PY2 an alternative alignment using the bipyridine based nitrogen peak is also shown, using Uv/Vis spectra the HOMO-LUMO transition was assigned to a MLCT transition to the bipyridine ligand.[126] It is thought that the bipyridine and dipyrrin chromophores are uncoupled.

The lowest BE peak in the valence photoemission spectra corresponds to the highest occupied molecular orbital (HOMO). For each dye complex the HOMO is present within the substrate band gap which prevents back transfer of electrons from the substrate to the molecules. The HOMO is located at a BE of 2.0 and 1.4 eV for the PY1 and PY2 dye complexes respectively. Having the HOMO inside the substrate band gap is a useful

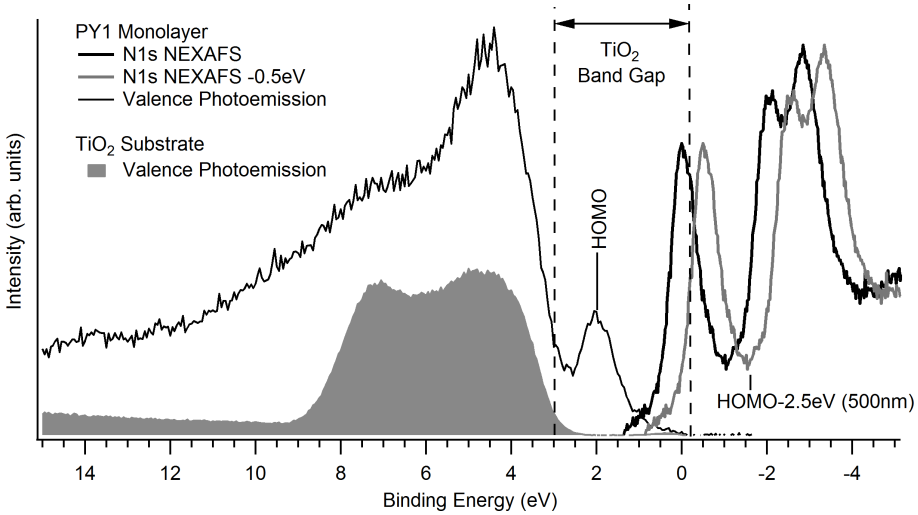

Figure 7.10: Valence band photoemission spectra of the clean substrate and of a monolayer of PY1, adjacent to a N 1*s* NEXAFS spectrum of the monolayer. The NEXAFS spectrum is also shown shifted to align with the optical HOMO-LUMO gap (shown in a lighter shade and labelled with the position of the measured HOMO minus the energy of the optical absorption). The photoemission spectra were measured using hν = 60 eV. The NEXAFS spectra were taken over the photon energy range hν = 397.3-404.3 eV.

feature in a water-splitting DSC as this helps prevents the water-splitting reaction from having to compete with recombination of the hole with an electron.

In the present case where the unoccupied states are probed using N 1*s* NEXAFS a *core* exciton (bound electron-hole pair) is created, whereas in an optically excited system a *valence* exciton is created. The presence of a hole in both NEXAFS and optical absorption shifts the unoccupied states to higher binding energy with respect to the ground state. The BE of the excitons, equivalent to the amount by which the unoccupied levels shift, is attributed to a combination of the Coulomb interaction between the hole and the excited electron and the rehybridization of the molecular states upon core- or valence-hole creation.[66] For transitions involving the dipyrrin ligands comparing the HOMO-LUMO gap for optical excitation involving the dipyrrin-based ligands (2.5 and 2.5 eV for PY1 and PY2 respectively) to the HOMO-LUMO gap for the core-excited system (2.0 and 2.25eV), the difference in energy is 0.5 and 0.25 $\pm$ 0.1 eV for the PY1 and PY2 dye complexes respectively. This is indicative of the difference between the N 1*s* core exciton and valence exciton BEs for the molecules. These values are a lot lower than the difference in BE previously found for pyridine (1.3 eV),[66] and complexes with bipyridine based ligands.[7, 96] This is likely due to a screening effect from the additional electron present on the negatively charged nitrogen atom in the dipyrrin ligand compared to the neutral nitrogen atom in the pyridine-based ligand.

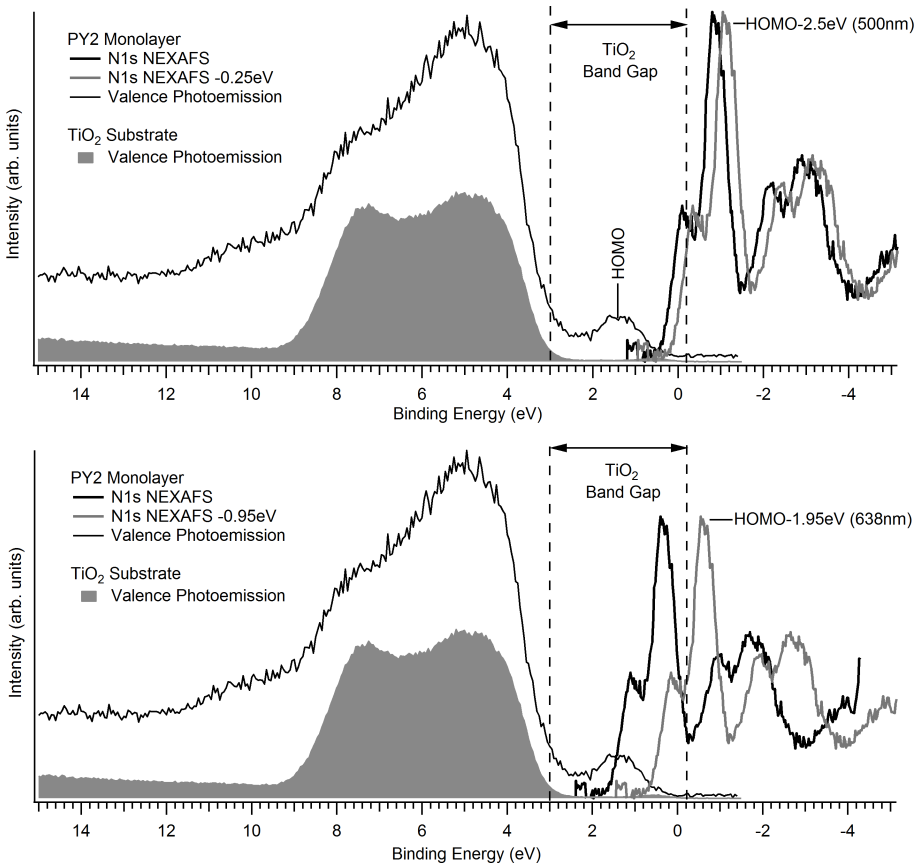

Figure 7.11: Valence band photoemission spectra of the clean substrate and of a monolayer of PY2, adjacent to a N 1*s* NEXAFS spectrum of the monolayer. The NEXAFS spectrum is also shown shifted to align with the optical HOMO-LUMO gap (shown in a lighter shade and labelled with the position of the measured HOMO minus the energy of the optical absorption). The photoemission spectra were measured using hν = 60 eV. The NEXAFS spectra were taken over the photon energy range hν = 397.3-404.3 eV. The top spectrum uses the position of the negative dipyrrin nitrogen peak to place the NEXAFS spectrum onto the BE scale, the bottom spectrum uses the position of the nitrogen bipyridine peak.

The presence of only a single set of NEXAFS peaks but two intense nitrogen XPS peaks could suggest that the molecule has been damaged during the experiment. The NEXAFS spectra were always conducted on a fresh spot of the sample to help prevent beam damage from affecting the spectra. It is possible that the molecule may have been damaged during deposition or adsorption to the surface. If this is the case then the molecule will be less suitable for real world DSC devices than the bipyridine-based complexes more commonly used.

For PY2 the HOMO-LUMO transition was assigned to a MLCT transition to the bipyridine ligand using UV/Vis spectra.[126] Performing the energy level alignment on PY2 using the neutral nitrogen peak as shown in Figure 7.11 causes the LUMO peak corresponding to the bipyridine ligand to lie within the band gap of the TiO_2. The HOMO-LUMO gap for optical excitation (1.95 eV) and the HOMO-LUMO gap for the core-excited system were compared and the difference in energy was found to be 0.95 ± 0.1 eV. Similar results for the difference in exciton BEs have previously been found for bipyridine based dye complexes such as N3.[7]

Shifting the NEXAFS spectra of each dye complex into line with the optical HOMO-LUMO gap as shown in Figures 7.10 and 7.11, causes the LUMO for both dye complexes to lie above the conduction band edge. In a real water-splitting device this energetic overlap permits electron injection from the LUMO into the substrate for both dye complexes. The presence of a core exciton in the NEXAFS causes the LUMO of the core-excited systems to lie within the substrate band gap preventing charge transfer for this orbital. This allows us to use electrons excited to the LUMO as a reference, allowing us to probe electron injection from those remaining unoccupied levels that lie above the conduction band edge.[68, 115]

7.3.3 DFT calculations

DFT simulations have been conducted to help determine which orbitals are capable of charge transfer. Figure 7.12 shows the calculated molecular orbitals of the molecules studied in this investigation. The HOMO of the PY1 complex appears to be mostly absent from the central ruthenium atom with most of the density present on the nitrogen atoms of one of the dipyrrin ligands. There is another orbital in the DFT results with a similar charge distribution to the HOMO present on the other dipyrrin ligand with a similar energy, these orbitals would not be resolvable in NEXAFS spectra. The LUMO of the PY1 dye complex is mostly based on one of the dipyrrin ligands with some density on the central ruthenium atom, this would provide a high degree of overlap with the HOMO which would make help to make the HOMO→LUMO transition efficient.

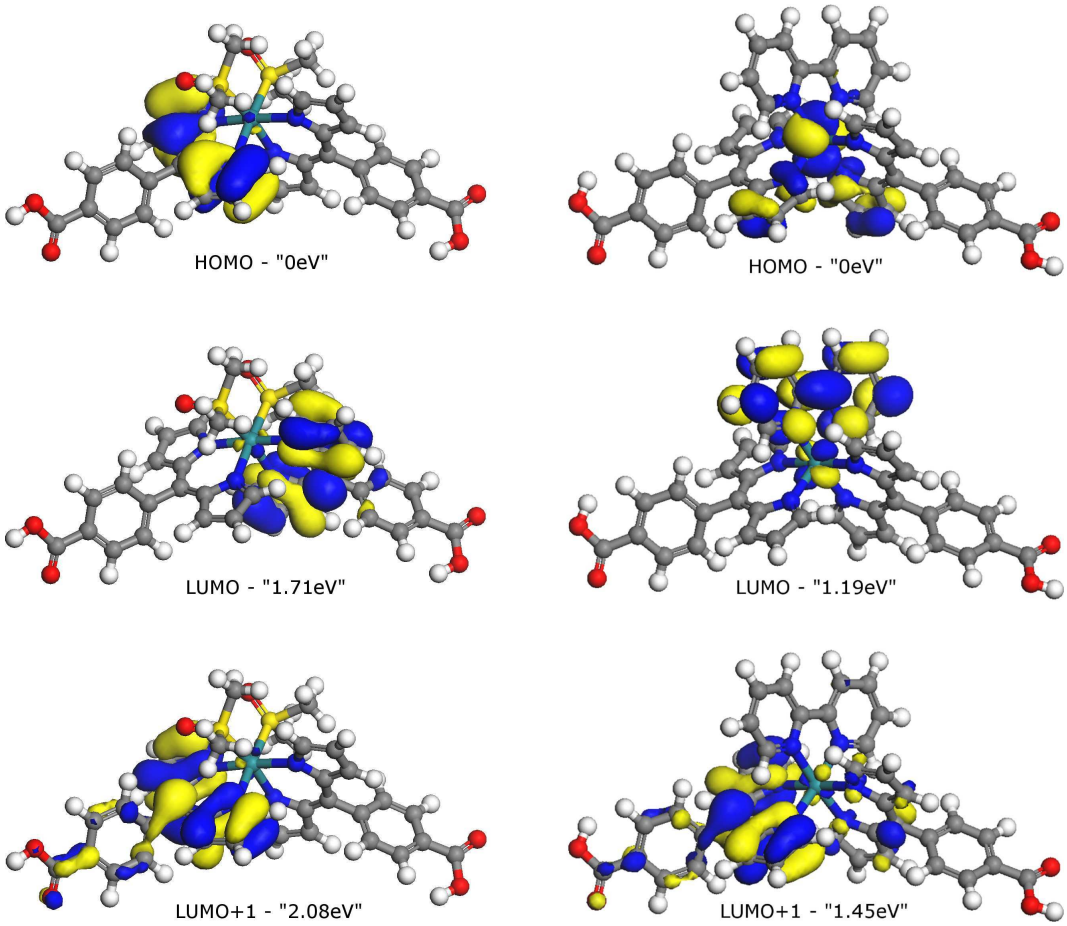

Figure 7.12: DFT calculations showing the electronic orbitals of geometry-optimized free PY1 (left) and PY2 (right) molecules with calculated orbital energies.

The LUMO does not extend to the carboxylic acid groups which would be attached to the substrate, meaning that this orbital may not overlap efficiently with the substrate orbitals. This will probably lead to less efficient charge transfer from excited molecules to the substrate in a real world DSC. The PY1 LUMO+1 is very similar to the molecules LUMO but with a smaller electron density around the pyrrole rings of the dipyrrin.

The HOMO of the PY2 dye complex is mostly present on the central ruthenium atom with some density on the neutral nitrogen atoms. The LUMO of the PY2 complex is primarily located on the bipyridine ligand with some presence on the central ruthenium atom as previously assigned using UV/Vis studies,[126] this orbital would most likely not be capable of charge transfer as the calculated adsorption geometry showed that the bipyridine ring stands away from the surface, also it has previously been shown that the bipyridine and dipyrrin ligands of this complex are largely uncoupled.[126] The PY2 dipyrrin-based LUMO is present on a dipyrrin ligand but shows very little intensity on the benzene ring next to the carboxylic acid groups compared to the unoccupied orbitals of the PY1 complex.

7.3.4 Charge Transfer Dynamics

Electron injection from the excited molecule into the substrate conduction band can be used to generate an electric current in a photovoltaic DSC or a potential capable of oxidising a water molecule in a water-splitting DSC. The electron injection process is in competition with other de-excitation channels including channels that could cause damage to the dye molecules, by decreasing the timescale of electron injection it should be possible to create more efficient DSC devices with longer effective lifespans. The core-hole clock implementation of RPES is used here to measure an upper limit on the timescale for molecule-to-substrate charge transfer for unoccupied orbitals in each molecule. This technique has previously been used on isolated bi-isonicotinic acid ligands and the N3 dye complex as well as related molecules on rutile TiO_2(110),[7, 115] these experiments have shown that charge transfer from the molecule to the substrate can occur on the low-femtosecond timescale.

The core-hole clock implementation of RPES uses the fact that if charge transfer is occurring, it must be competing with the de-excitation of the excited state via resonant photoemission or resonant Auger. The time taken for de-excitation here can also be described as the lifetime of the N 1*s* core hole. Here we calculate the electron injection time from the LUMO+2 and LUMO+3 orbitals of both dye complexes. The electron injection time τ_{EI} for electrons moving from the unoccupied level of the molecule adsorbed to the substrate to unoccupied substrate states is given by Eq. 7.3.1. The derivation of this equation was discussed in Section 4.3.3.

$$\tau_{EI} = \tau_{CH} \frac{I^{mono}_{RPES} / I^{mono}_{NEXAFS}}{I^{multi}_{RPES} / I^{multi}_{NEXAFS} - I^{mono}_{RPES} / I^{mono}_{NEXAFS}} \tag{7.3.1}$$

The variables I^{mono}_{RPES} and I^{multi}_{RPES} represent the intensities of the unoccupied peak being studied in the monolayer and multilayer respectively. These values are each normalized by the total cross sections as provided by the NEXAFS intensities I^{mono}_{NEXAFS} and I^{multi}_{NEXAFS}. The variable τ_{CH} is the average $N1s$ core-hole lifetime which has previously been measured as 6 fs.[119]

For resonant photoemission to occur following core excitation, the occupied and unoccupied orbitals involved must have some interaction. The largest probability for resonant photoemission occurs when both of the electrons involved in the transition are located on the same atom, specifically the site of the core-hole. Resonant photoemission is in essence a special type of Auger decay and whilst interatomic Auger transitions can occur,[123] the rates of these events are negligible in all but the lowest energy Auger processes.

In these experiments resonant photoemission requires some degree of overlap between the HOMO, LUMO and the core-excited atom, however in a real DSC only an overlap between the HOMO and LUMO is required for photoexcitation between the states. The DFT results reported earlier showed that both molecules have the orbital overlaps required for photoexcitation and resonant photoemission.

The energy level alignment experiments have shown the LUMO of each molecule lies substantially within the TiO_2 substrate band gap when a core exciton is present. Charge transfer requires the unoccupied orbital to overlap with the substrate conduction band so in this case the LUMO should be incapable of effective charge transfer to the substrate allowing it to be used as a reference orbital. Electron injection is energetically allowed from higher energy unoccupied molecular orbitals as they do overlap with the conduction band of the substrate. As the LUMO orbitals of both molecules do not lie completely within the band gap of the TiO_2 it is possible that some charge transfer may occur from this orbital, if this occurs then the calculated upper limit on charge transfer timescale of the other molecular orbitals would increase due to the decrease in the reference LUMO peak. The creation of a core-hole in RPES prevents the LUMO from being studied directly due to the LUMO lying within the TiO_2 band gap in the core-excited system. However, if the dipyrrin-based LUMO, LUMO+2 and LUMO+3 orbitals have similar spatial distributions in the dye complexes then it can be assumed that the coupling of these orbitals to the substrate and, therefore, the corresponding charge-transfer dynamics will be similar.

The experimental RPES data includes Auger peaks which need to be excluded from the charge transfer analysis, this is achieved by integrating the RPES spectra over a selected BE window as shown in Figure 7.13 for both the multilayer and monolayer spectra. Any peaks at the energies of the LUMO+2 and LUMO+3 resonances are due solely to resonant photoemission, as normal photoemission contributes a sloping background only.

The RPES and NEXAFS spectra are normalized to the intensity of the LUMO as shown in Figure 7.14. The PY2 spectra are normalised to the intensity of the bipyridine based LUMO, as this peak lies furthest within the substrate band gap. Differences in the intensity of the bipyridine and dipyrrin LUMOs in the PY2 RPES spectra are attributed to matrix element effects. The peaks in the NEXAFS spectra represent the unoccupied levels' full intensities, whereas for RPES spectra the LUMO should have its full intensity but the other unoccupied levels may be depleted by charge transfer.

For the multilayer it can be seen that the LUMO+2 and LUMO+3 peaks have lower intensity in the RPES spectra than in the corresponding NEXAFS spectra. Since no

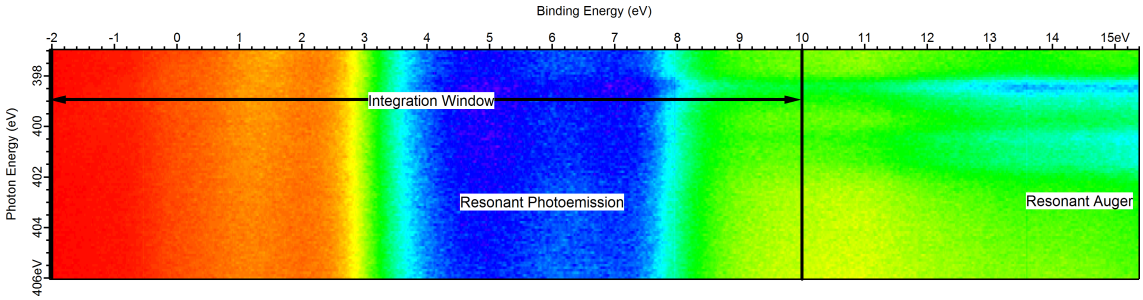

Figure 7.13: N 1*s* RPES spectrum of a monolayer of PY1 on rutile TiO_2(110) showing the BE integration window used to select only the resonant photoemission decay channel.

charge transfer to the substrate can occur in the multilayer this intensity reduction is attributed to matrix element effects due to the different techniques used and also potentially due to ultrafast delocalization of electrons within the molecule.[116, 127] These effects are accounted for in Equation 7.3.1 through the experimentally derived value of $I^{multi}_{RPES}/I^{multi}_{NEXAFS}$. In the monolayer the remaining localized electrons are capable of undergoing charge transfer to the substrate causing further reduction to the intensity of the LUMO+2 and LUMO+3 peaks in the monolayer RPES spectra.

Table 7.2: Table of RPES/NEXAFS ratios for multilayer and monolayer coverages of PY1 and PY2 dye molecules and the calculated upper limit on charge transfer timescale for each orbital studied.

Dye molecule	Orbital	Multilayer RPES/NEXAFS ratio	Monolayer RPES/NEXAFS ratio	Upper limit on charge transfer timescale (fs)
PY1	LUMO+2	0.286	0.106	4 ± 1
PY1	LUMO+3	0.150	0.056	4 ± 1
PY2	LUMO+2	0.415	0.043	1 ± 1
PY2	LUMO+3	0.249	0.041	2 ± 1

For the PY2 monolayer LUMO+2 and LUMO+3 RPES peaks there is no discernable peak at the expected photon energy as the corresponding peak in the NEXAFS spectrum. For these peaks the level of noise is taken as an upper limit for the intensity of any peak that might be present. These values are then used to calculate an upper limit for the charge transfer time according to Eq 7.3.1 for the LUMO+2 and LUMO+3 orbitals of both molecules as shown in Table 7.2. These values were found to lie between 1 and 4 fs which are in agreement with the upper limit on the time scale for charge transfer of both the N3 dye complex and the bi-isonicotinic acid ligand on TiO_2 using this technique, which have previously been found to be 12 fs and 3 fs respectively.[115] The core-hole clock technique has also shown sub-femtosecond timescale charge trans-

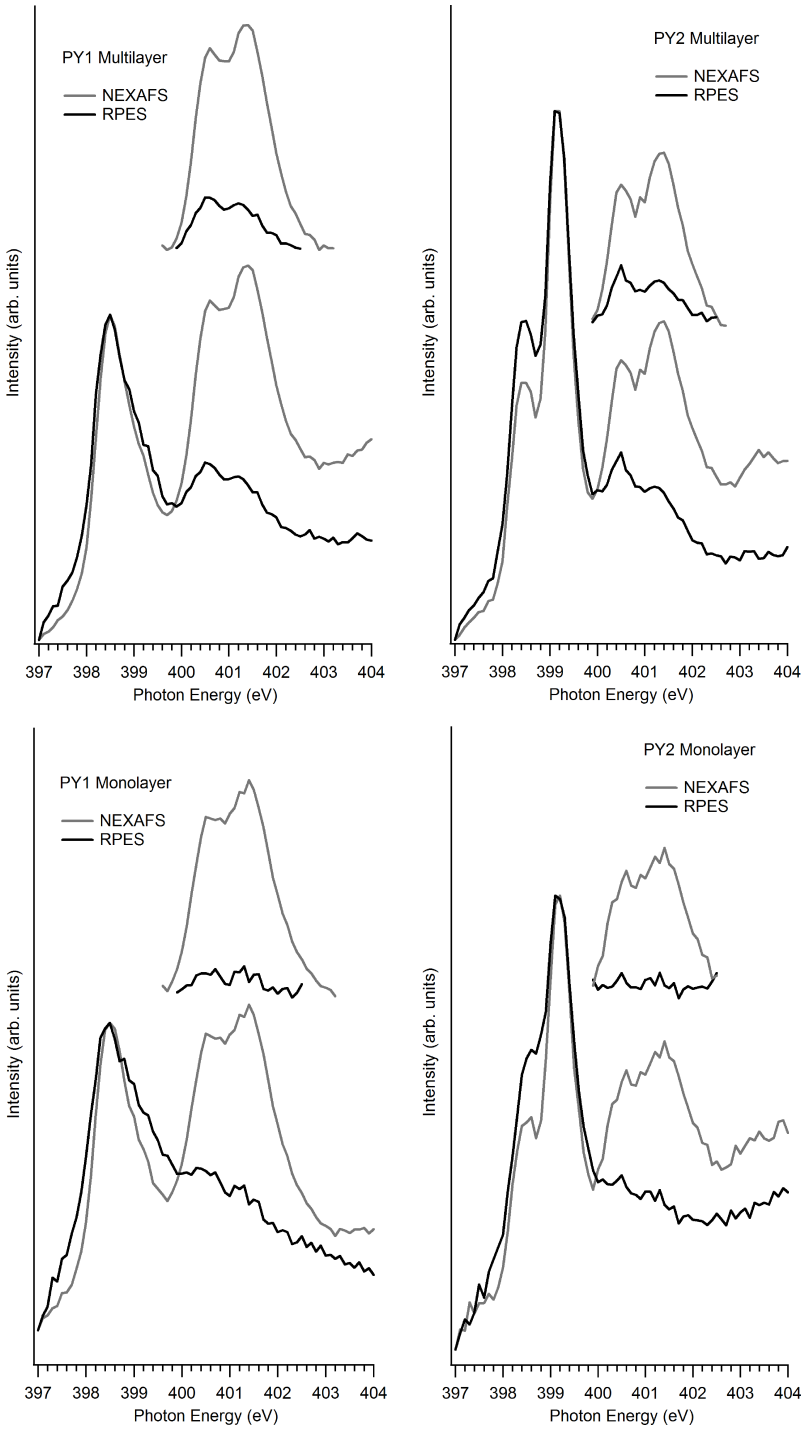

Figure 7.14: N 1*s* RPES and N 1*s* NEXAFS spectra of multilayers (top row) and monolayers (bottom row) of PY1 (left column) and PY2 molecules (right column). The RPES spectra are BE integrations over a range which excludes the Auger peaks. The LUMO+2 and LUMO+3 peaks are also shown after having the sloping background removed.

fer from a sulphur atom attached to a ruthenium surface using the *S*2*s* orbital which has a core-hole lifetime of 0.5 fs.[128] Due to the exponential nature of the decay processes involved, timescales can only realistically be measured within one order of magnitude of the core-hole lifetime. In this work the core-hole lifetime was 6 fs and the sub-femtosecond result is due to an excellent signal to noise ratio in the RPES spectra and the large intensity of the LUMO+2 and LUMO+3 peaks in the NEXAFS spectra.

7.4 Summary

UHV electrospray deposition has been used to deposit both monolayers and multilayers of the PY1 and PY2 dye complexes on the rutile TiO_2(110) surface *in situ*. Photoemission spectroscopy has been used to characterize the core and valence levels of the system, which were used to deduce the bonding geometry of each dye complex on the rutile TiO_2(110) surface. We find that for both dye complexes both carboxylic acid groups deprotonate so that their oxygen atoms bond to titanium atoms on the substrate surface. DFT calculations suggest that the molecules bond to the surface in a 2M-bidentate bonding geometry using rows of titanium atoms separated by a non-bonding row of titanium atoms.

The valence band photoemission spectra show that the HOMO of the PY1 dye complexes occurs at a high BE similar to molecules containing three bipyridine-based ligands, whilst the PY2 dye complex has a HOMO at a similar BE to N3.[7, 96] The difference between the BEs of the dipyrrin complexes is attributed to the difference in electron densities on the central ruthenium ion, which is caused by the difference in electronegativity of the attached ligands. In a water-splitting dye complex the potential to remove electrons from a water molecule is created by a hole in the HOMO. The HOMO becomes an electron acceptor after losing an electron and having a higher binding energy makes the HOMO a better electron acceptor. A HOMO with a higher binding energy could therefore be better at removing electrons from a water molecule, which will aid the water-splitting reaction. This could be investigated further in the future using both single and multi-centre water-splitting dye complexes based upon dipyrrin ligands.

The energetic alignments of the systems were determined by placing the valence photoemission and N 1*s* NEXAFS of a monolayer of each dye complex onto a common BE scale. The bandgap of TiO_2(110) was aligned using the valence photoemission of the clean substrate. The energetics for photoexcitation from the valence band (as occurs in working DSCs) were compared with those found for photoexcitation from the N 1*s*

core level, for which the unoccupied levels appear at higher BE. This comparison allowed quantification of the difference in BE of a core and valence excitation for each dye complex, found to be 0.5 and 0.25 $\pm$ 0.1 eV. for the PY1 and PY2 dye complexes respectively. For PY2 an alternative alignment was performed using the bipyridine-based LUMO showing a difference in BE between the core and valence excitations of 0.95 $\pm$ 0.1 eV which is similar to other pyridine based complexes. The energetic alignments reveal that the LUMO of each dye complex is incapable of charge transfer to the substrate when a core exciton is created, this allows us to use this level as a reference to calculate charge transfer timescales from higher unoccupied orbitals. The energetic alignment diagrams also show that the dye complexes are capable of charge transfer from their LUMO after optical excitation whilst adsorbed on the rutile TiO_2(110) surface and the HOMO lies within the substrate band gap helping prevent back transfer of electrons. This shows that rutile TiO_2(110) is likely to be a suitable substrate for a water-splitting DSC based on these molecules.

According to the DFT simulations the PY1 complex has both its LUMO and LUMO+1 orbitals located on the dipyrrin ligands with a significant overlap with the HOMO, suggesting that this molecule could have both an efficient HOMO$\rightarrow$LUMO transition. The PY2 complex has its LUMO on the bipyridine ligand which will most likely prevent charge transfer from occuring from this orbital. The LUMO+1 of the PY2 complex has a low intensity on the end of the dipyrrin ligand attached to the substrate which might lead to less efficient charge transfer than for the PY1 complex.

The core-hole clock implementation of RPES was used to find that the upper time limit of electron injection from the LUMO+2 and LUMO+3 orbitals of each dye complex to the substrate occur in the range of 1-4 fs. In agreement with previous studies of N3, bi-isonicotinic acid and related molecules on TiO_2, which found charge transfer to occur on the low and sub-femtosecond timescales. It is thought that the LUMOs of each dye complex are all located on the dipyrrin ligands except the bipyridine based LUMO of PY2 at 399.2 eV, so electron injection in valence excited systems is expected to occur on a similar time scale.

CHAPTER 8

Single-centre water-splitting complex on TiO_2(110)

8.1 Introduction

Chapters 6 and 7 focused on photovoltaic dye complexes, which had no space for water molecule attachment as their metal centres were fully coordinated. In order to attach a water molecule we need to change the ligands on the sensitizer so that there is space for the water molecule. Once we have a water molecule attached to the metal centre it is possible that charge transfer could be used to catalyse the breakdown of the water molecule into its component atoms. In a real photocatalytic dye cell the dye complex would be surrounded by additional water molecules so that the catalytic cycle can continue. In these experiments the surface is under ultra high vacuum so the process would stop after the hydrogen atoms are removed from the water molecule.

A single centre water-splitting dye complex can be made by simply adapting an existing photovoltaic dye sensitizer such as N3. The anchor ligand bi-isonicotinic acid was used to allow the dye molecules to bond to the TiO_2 surface, as previously seen in Chapter 6. A terpyridine ligand is also part of the complex, as this ligand has a conjugated structure it is also capable of absorbing incident light. The metal centre has only a single remaining ligand bonding site to form an octahedral structure, this site can be used to bind a monodentate ligand such as a water molecule. After successful electron injection from a photoexcited adsorbed complex into the substrate the metal centre will have a higher oxidation state, this creates a potential which can remove H^+ ions from the attached water molecule. By optimising the structure of the complex the water-splitting reaction could be made more efficient leading to beneficial factors such as an increased reaction rate or greater complex stability.

The single centre water-splitting complex studied here can also be used as a model of the reaction centre of a multi-centre water-splitting dye complex. The information obtained from studying these molecules should prove to be helpful when interpreting the data on a multi-centre water-splitting dye complex. Whilst a single centre water-splitting dye sensitizer could be used in a real water-splitting DSC device, a previous study has shown that multi-centre dye complexes are more effective in catalysing this reaction and do not require additional catalysts in the electrolyte solution.[31] However single centre dye complexes will likely prove easier to manufacture.

As described in Section 1.2 dye-sensitized solar cells (DSCs) consist of efficient light harvesting molecules adsorbed onto the surface of a substrate with a wide band gap such as TiO_2.[5, 22, 124] After the molecule absorbs a photon of visible light an electron is promoted from the highest occupied molecular orbital (HOMO) to the lowest unoccupied molecular orbital (LUMO), if this orbital overlaps energetically with the conduction band of the substrate then charge transfer from the molecule to the substrate can occur. After charge transfer has occurred the adsorbed molecule is left in a state which can accept electrons from another source. In a photovoltaic DSC the lost electron is normally replaced using a liquid electrolyte to allow for subsequent excitations.[129] In a water-splitting DSC the loss of electrons creates a potential that causes the oxidation of a water molecule attached to the metal centre of the adsorbed dye molecule, leading to the production of H^+ ions. The process takes several steps and produces H^+ ions which travel to the cathode where they recombine with the electrons initially transferred to the substrate producing hydrogen molecules. A more detailed description on the mechanism underlying water splitting is given in Section 1.3.

The molecules studied in this work each contain a single bi-isonicotinic acid ligand (2,2'-bipyridyl-4,4'-dicarboxylic acid), these ligands have carboxylic acid groups which are capable of bonding to the TiO_2 surface. Bi-isonicotinic acid has previously been shown to adopt a 2M-bidentate structure when adsorbed to the rutile TiO_2(110) surface,[14] on adsorption the carboxylic acid groups deprotonate to allow the molecule to bond covalently to the surface. N3 is currently one of the most efficient dye complexes used in photovoltaic DSCs and contains two bi-isonicotinic acid ligands which allow it to bond to the TiO_2 surface.[9] Previous studies of N3 and related molecules on rutile TiO_2(110) in Chapter 6 using photoemission spectroscopy have shown that each molecule shows evidence of deprotonation of two carboxylic acid groups on adsorption to the TiO_2 surface.[7, 100] This bonding geometry provides a strong chemical coupling which allows for the efficient transfer of excited electrons from the adsorbed dye molecules to the substrate.

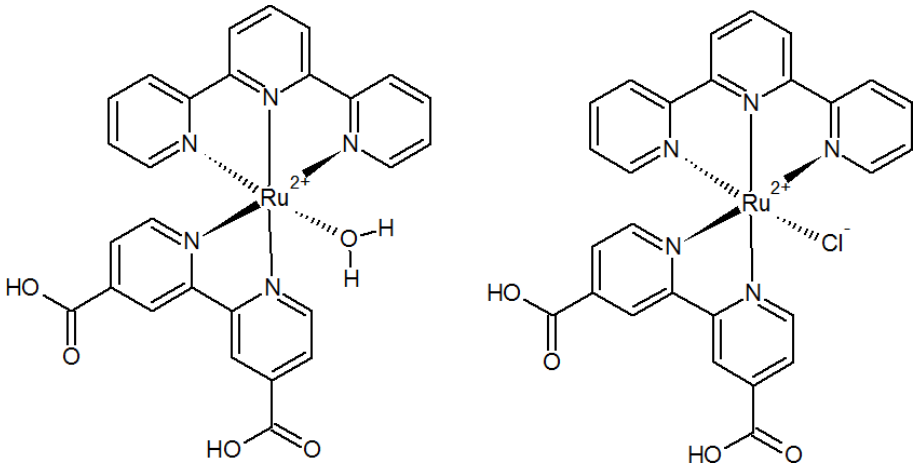

Figure 8.1: Chemical structures of the single centre water-splitting complex (WSC) studied in this investigation (left) and its chlorine containing analog (ClSC) (right).

The main dye complex investigated in this study is a single centre water-splitting complex (labelled water single-centre complex or WSC) (aqua(2,2′-bipyridyl-4,4′-dicarboxylic acid)-(2,2′:6′,6″-terpyridine)Ruthenium(II)), a second complex was also investigated containing a chloride ion instead of a water molecule (labelled chloride single-centre complex or ClSC) ((2,2′-bipyridyl-4,4′-dicarboxylic acid)-(2,2′:6′,6″-terpyridine)chloride Ruthenium(II)). The chemical structures of the two dye complexes are shown in Figure 8.1. The ClSC complex was studied to help identify any additional interactions caused by the water molecule or its oxidaton products as the only difference between the complexes is the identity of the monodentate ligand.

Dye complexes were deposited onto a rutile TiO_2 substrate at both monolayer and multilayer coverages using *in situ* ultra high vacuum electrospray deposition. The adsorbed dye molecules were studied using X-ray photoemission spectroscopy (XPS) to study the bonding of the molecules to the surface. Near-edge X-ray absorption fine structure (NEXAFS) spectroscopy and density functional theory (DFT) are used to examine the electronic structure of the molecules. The core-hole clock implementation of resonant photoemission spectroscopy (RPES) is used to calculate upper limits on the timescale of electron injection from the adsorbed molecules to the substrate.

8.2 Method

Experiments were carried out at the surface science undulator beamlines I511-1 and I311 at MAX-lab, Sweden.[54, 55] The I511-1 end station is equipped with a Scienta R4000 electron analyser, which can be rotated orthogonally about the beam axis. The

I311 end station is equipped with a Scienta SES-200 electron analyzer.

The experiments were performed using a single crystal rutile TiO_2(110) substrate (Pi-Kem, UK). At I511-1 the substrate was clamped to a silicon crystal and at I311 the substrate was mounted on a pyrolytic boro nitride heater, this allowed us to anneal the samples to prepare the surfaces for deposition. The sample was prepared by sputtering and annealing as described in Section 6.2. The surface was determined clean when there were negligible C 1*s* and K 2*p* core-level signals and a single Ti^{4+} oxidation state in the Ti 2*p* spectrum.

The two dye complexes were prepared using literature methods.[32] The dye molecules were deposited using an *in situ* UHV electrospray deposition source (MolecularSpray, UK), from a solution of $\sim$ 5 mg of dye in 200 ml of a 1(methanol):1(water) mixture and a pure methanol solution for the WSC and ClSC complexes respectively. The deposition method is described in detail in Section 6.2. A UHV gate valve was used to separate the preparation chamber from the electrospray apparatus between depositions. With the valve open but the needle voltage turned off and thus no electrospray process occurring, the pressure in the preparation chamber was $\sim 2 \times 10^{-8}$ mbar. With the voltage turned on, the preparation chamber pressure rose to $\sim 5 \times 10^{-7}$ mbar, the additional pressure being due to residual solvent molecules in the beam.

For the electron spectroscopy data, the total instrument resolution ranges from 65-195 meV. All XPS spectra have been calibrated to the substrate O 1*s* peak at 530.05 eV,[105] and a Shirley background removed before curve fitting using Voigt functions.

NEXAFS and RPES spectra were taken over the N 1*s* absorption edge and were measured using the electron analyzer. For NEXAFS spectra the nitrogen Auger yield was used whilst for RPES spectra the valence band photoemission was monitored. In this experiment beam damage was monitored by taking NEXAFS spectra before and after an RPES spectrum and comparing the appearance of the peaks above the LUMO. These spectra revealed limited beam damage occurred over the duration of an RPES spectrum. Multiple RPES spectra were taken for each coverage in different positions and combined to produce the RPES spectra shown here.

Density functional theory simulations (DFT) calculations were carried out as an aid to interpreting the experimental data. Geometry optimizations were performed on free molecules of each dye complex using $Dmol^3$ at the DFT-generalized gradient approximation level (DFT-GGA) with the Perdew-Burke-Enzerhof (PBE) functional.[63, 64, 106] The optimized structures were then used to calculate the molecular orbitals for each molecule.

8.3 Results and Discussion

8.3.1 Adsorption

The samples used for the following spectra are classed as either *monolayer* or *multilayer*. Here a monolayer is defined as a sample having the vast majority of molecules directly adsorbed to the surface and a multilayer as having a film of molecules thick enough that the majority of photoelectrons in XPS come from molecules above the first adsorbed layer. From the attenuation of the substrate O 1*s* XPS signal the multilayer is estimated to be at least two to three layers thick for each dye complex. The binding energies (BEs) of the peaks discussed are summarised in Table 8.1.

Table 8.1: BEs (eV) for each molecule, the monolayer spectra are calibrated to the substrate O 1*s* peak at 530.05 eV and the multilayer spectra are calibrated using the Fermi level in the valence band.

		WSC	ClSC
PES			
O 1*s*	TiO_2	530.05	530.05
	Monolayer C=O and COO^-	531.3	531.3
	Multilayer C=O and COO^-	531.6	531.1
	Multilayer C-OH	533.4	533.0
C 1*s*	Terpyridine	285.3	285.3
	Bi-isonicotinic acid	286.2	286.1
	Carboxyl	288.1	288.2
Ru 3*d*		281.2	281.1
N 1*s*	Pyridine	400.3	400.5
Valence band	HOMO	2.1	2.05
N 1*s* NEXAFS			
Unshifted	LUMO	0.8	1.05
Aligned to optical data	LUMO	-0.4	-0.4

Figure 8.2 and Figure 8.3 show the O 1*s* monolayer and multilayer spectra of the WSC and ClSC dye complexes on rutile TiO_2(110) respectively. For both of the dye molecules the monolayer spectra are dominated by the TiO_2 substrate oxygen peak. The two peaks at higher binding energy are due to the oxygen atoms in the carboxylic acid groups of the bi-isonicotinic acid ligands of each molecule. For isolated dye molecules in the multilayer the intensity of these two peaks should be equal due to the equivalent number of carbonyl (C=O) and hydroxyl (C-OH) oxygen atoms.

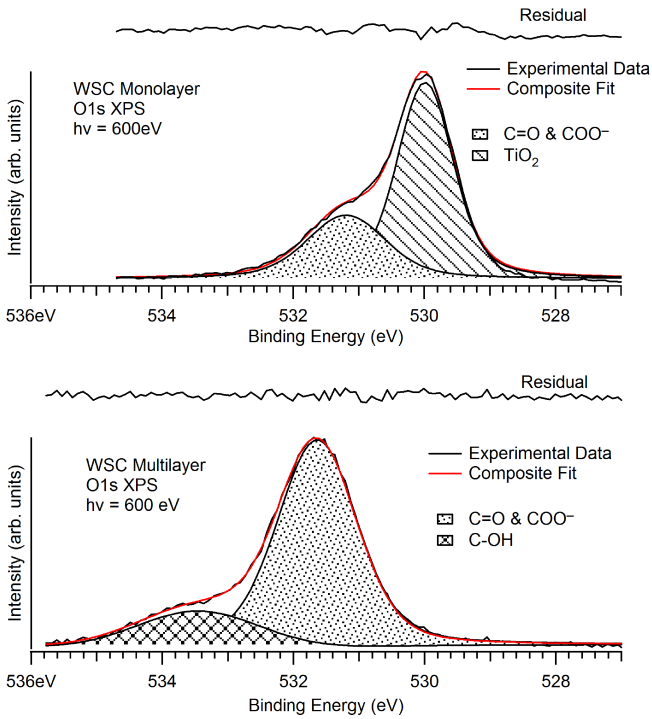

Figure 8.2: O 1*s* core-level photoemission spectra of a monolayer of ClSC (top) and a multilayer of ClSC (bottom) on rutile TiO_2(110), measured using hν = 600 eV.

Previous studies of bi-isonicotinic acid and N3 have shown deprotonation of the hydroxyl groups on adsorption to TiO_2 to form a 2M-bidentate structure,[7, 14] as has also been shown in Chapters 6 and 7. This is a common bonding arrangement for pyridine based molecules with carboxylic acid groups on the TiO_2 surface.[109–111] After deprotonation the two oxygen atoms share an electron and are chemically equivalent. The BE of this oxygen species is similar to that of the carbonyl oxygen atom in isolated molecules and the two groups are unresolvable in the XPS spectra.[14] In Figures 8.2 and 8.3 there is no evidence of a hydroxyl oxygen peak in the WSC or ClSC monolayer spectra. This suggests that each molecule bonds to the surface using both of the two available carboxylic acid groups on the bi-isonicotinic acid ligand leading to a 2M-bidentate bonding geometry on the rutile TiO_2(110) surface, in the same way as an uncomplexed bi-isonicotinic acid molecule.[14]

O 1*s* XPS spectra of multilayers of each dye complex are shown in Figures 8.2 and 8.3. A 1:1 intensity ratio of deprotonated to protonated oxygen peaks is expected on the basis of the molecule structures shown in Figure 8.1. The spectra show evidence of deprotonation already in the multilayer from the reduced intensity of the C-OH signal for both complexes. This is likely due to charge balance through deprotonation of the carboxylic acid groups. In Chapter 6 Ru 455 also showed proton loss when the dye

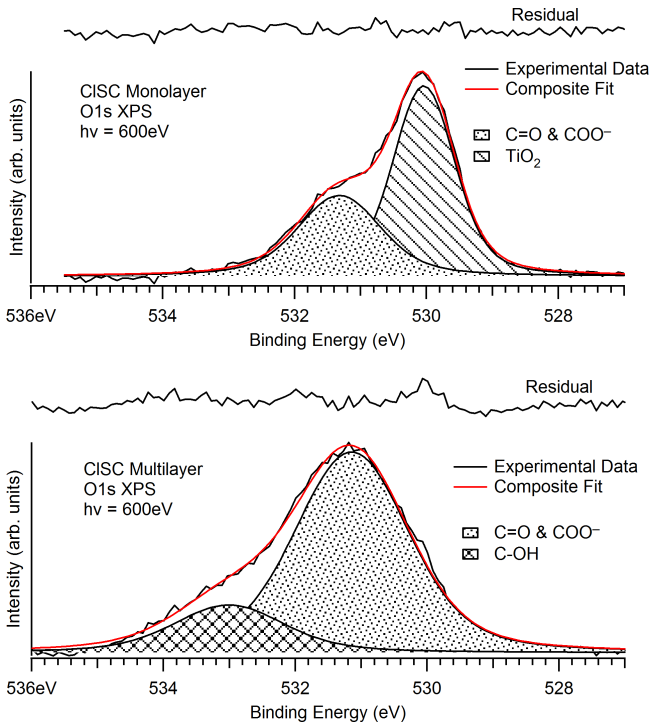

Figure 8.3: O 1*s* core-level photoemission spectra of a monolayer of ClSC (top) and a multilayer of ClSC (bottom) on rutile TiO_2(110), measured using hν = 600 eV.

was deposited under similar conditions. In both the monolayer and multilayer spectra there is no observable peak due to the oxygen atom in the water molecule. This may be because the water molecule has detached during the deposition or on adsorption to the surface. It is also possible that the chemical environment of the oxygen in the water molecule may be indistiguishable from the other chemical environments of the oxygen atoms.

Figure 8.4 shows the C 1*s* and Ru 3*d* XPS spectra of monolayers of each dye complex. The spectra appear similar to each other and the peaks have similar BEs (as shown in Table 8.1) for the carbon atoms in the terpyridine and bi-isonicotinic acid ligands. Each spectrum is dominated by a peak due to the carbon atoms in the pyridine groups. Also present at higher BE is the peak due to the carbon atom in the carboxylic acid groups. There are also two peaks due to the central ruthenium ion as the Ru 3*d* state is a doublet state with a spin orbit splitting of 4.2 eV.[112] The lower BE Ru $3d_{5/2}$ peak is present at ~281 eV. This is approximately 1 eV higher than metallic ruthenium,[112] consistent with the Ru^{2+} oxidation state of the metal centre.

Figure 8.5 shows the N 1*s* XPS spectra of monolayers of each dye complex. Both dye complexes show only a single nitrogen peak as expected from their chemical structure

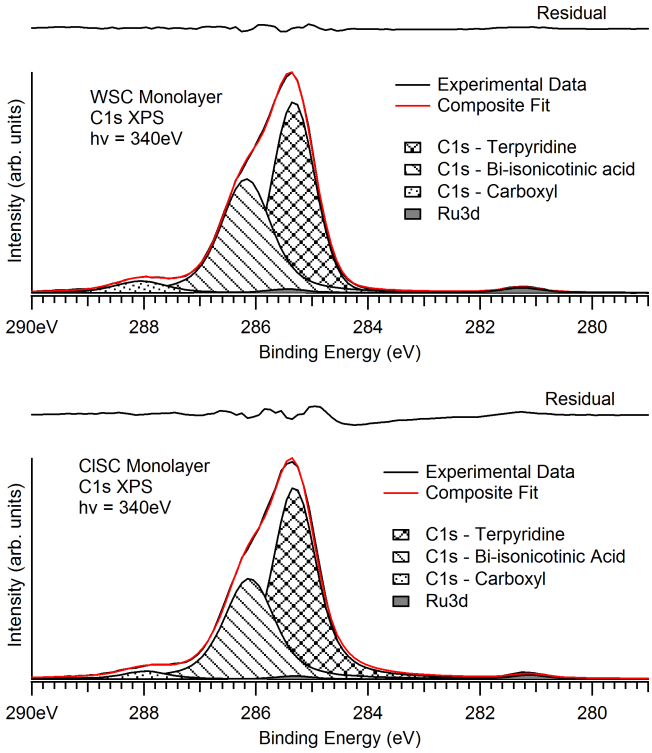

Figure 8.4: C 1*s* and Ru 3*d* core-level photoemission spectra of monolayers of WSC (top) and ClSC (bottom) on rutile TiO_2(110), measured using hν = 340 eV.

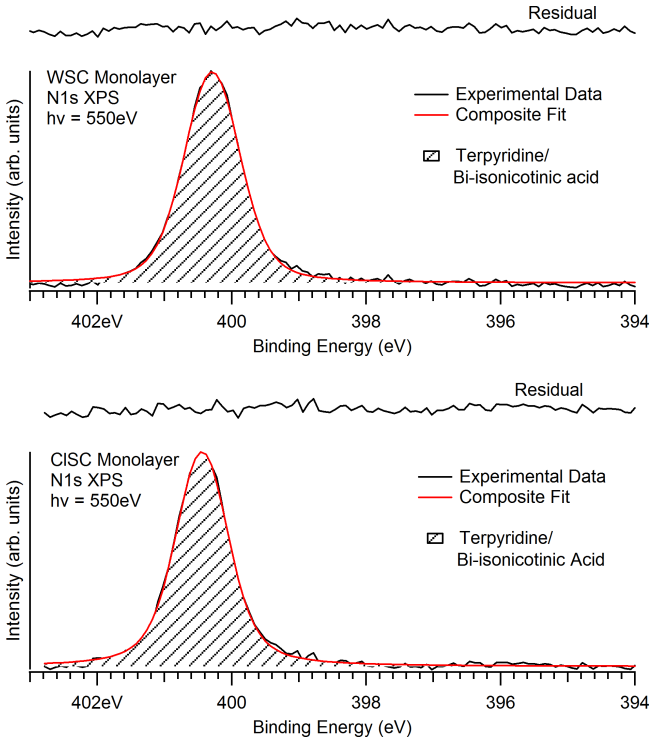

Figure 8.5: N 1*s* core-level photoemission spectra of monolayers of WSC (top) and ClSC (bottom) on rutile TiO_2(110), measured using hν = 550 eV.

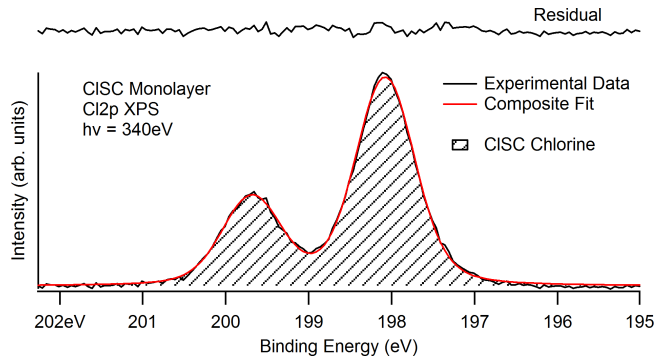

Figure 8.6: Cl 2*p* core-level photoemission spectra of a monolayer ClSC on rutile TiO_2(110), measured using hν = 340 eV.

corresponding to the nitrogen atoms in the pyridine rings. This supports the other photoemission data discussed indicating that the molecules have retained their molecular integrity during deposition. Multilayer C 1*s* and N 1*s* spectra have not been shown as they appear similar to the equivalent monolayer spectra for both dye complexes.

Figure 8.6 sbows the Cl 2*p* XPS spectrum of a monolayer of the ClSC dye complex, the multilayer spectrum is not shown as it has a similar appearance to the monolayer spectrum. The spectrum consists of two peaks which are due to Cl 2*p* being a doublet state. The state has a spin-orbit splitting of approximately 1.65 eV. The lower BE peak is present at ∼198 eV.

From the XPS data it appears that both dye complexes form a 2M-bidentate bonding geometry when adsorbed onto the rutile TiO_2(110) surface as illustrated in Figure 8.7, both complexes bonding to the surface via the deprotonation of the carboxylic acid groups on the bi-isonicotinic acid ligand. This bonding geometry is common for dye complexes containing bi-isonicotinic acid anchor ligands as seen previously in Chapter 6.

8.3.2 Electronic Structure

In a DSC, electrons are photoexcited from high-lying occupied molecular orbitals to previously unoccupied molecular orbitals. For subsequent electron injection into the substrate, the unoccupied level in question must overlap with available states in the substrate conduction band. UV/visible light spectra of the WSC and ClSC dye complexes in solution are shown in Figure 8.8. A real solar cell device will operate using optical excitation producing valence-holes in the molecules, this is in contrast to the core-holes created by the X-rays used for the photoemission and NEXAFS measurements. The lowest energy maximum in each spectrum is attributed to the HOMO→LUMO

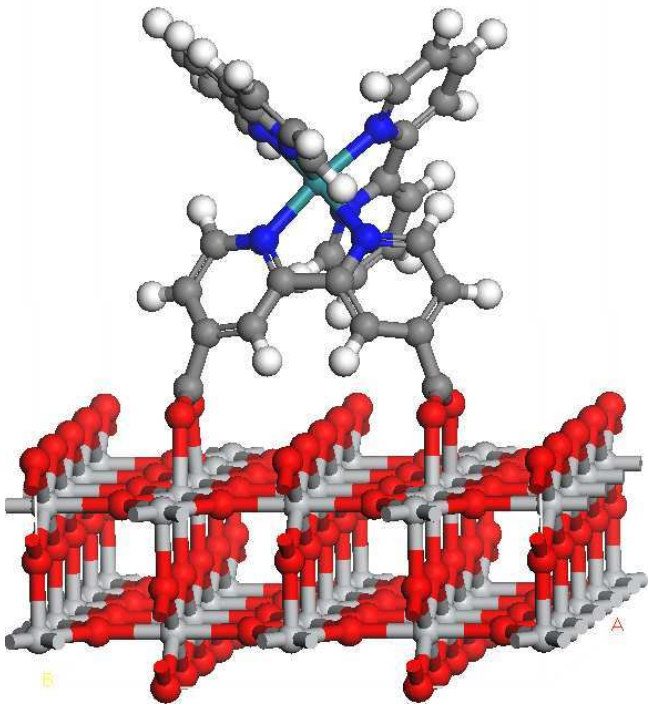

Figure 8.7: DFT optimised structure of a WSC molecule adsorbed onto the rutile TiO_2(110) surface in a 2M-bidentate bonding geometry.

transition corresponding to a metal-to-ligand charge transfer (MLCT) Ru(4d)→bpy(π*)COOH transition. The energy of this excitation is lower for the ClSC dye than the WSC dye.

Spectra representing the occupied and unoccupied states of monolayers of each dye complex have here been placed on a common BE scale as shown in Figure 8.9, following a procedure outlined earlier in Section 4.2. This procedure has previously been performed on monolayers of N3 and related molecules.[7] The resulting energy level alignment diagrams can be used to identify the potential charge transfer processes that can occur in the dye complexes.[113–116]

Figure 8.9 shows the N 1*s* (Auger yield) NEXAFS and valence photoemission spectra for a monolayer of each dye complex, along with the clean substrate valence photoemission spectrum (measured at hν=110 eV). The N 1*s* core level XPS spectra showed only a single pyridine based nitrogen peak for both complexes, this peak was used to place the NEXAFS on the common BE axis. Previous studies on the bi-isonicotinic acid ligand and on the N3 dye complex have shown that the N 1*s* NEXAFS is dominated by pyridine-like π* orbitals.[7, 117, 118]

The valence band spectra for monolayers of WSC and ClSC molecules appear similar to those previously obtained for monolayers of N3 and related molecules as seen

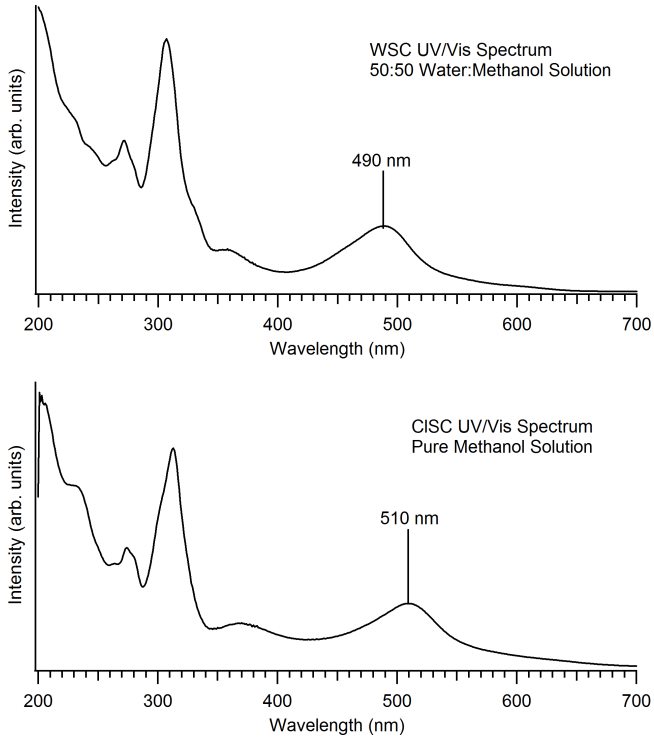

Figure 8.8: Optical absorption spectra of the WSC and ClSC complexes in a 1:1 water:methanol solution and pure methanol respectively. The spectra were taken over the visible light and ultraviolet wavelength range, the wavelengths corresponding to the lowest energy absorption maxima are shown labelled on the spectra.

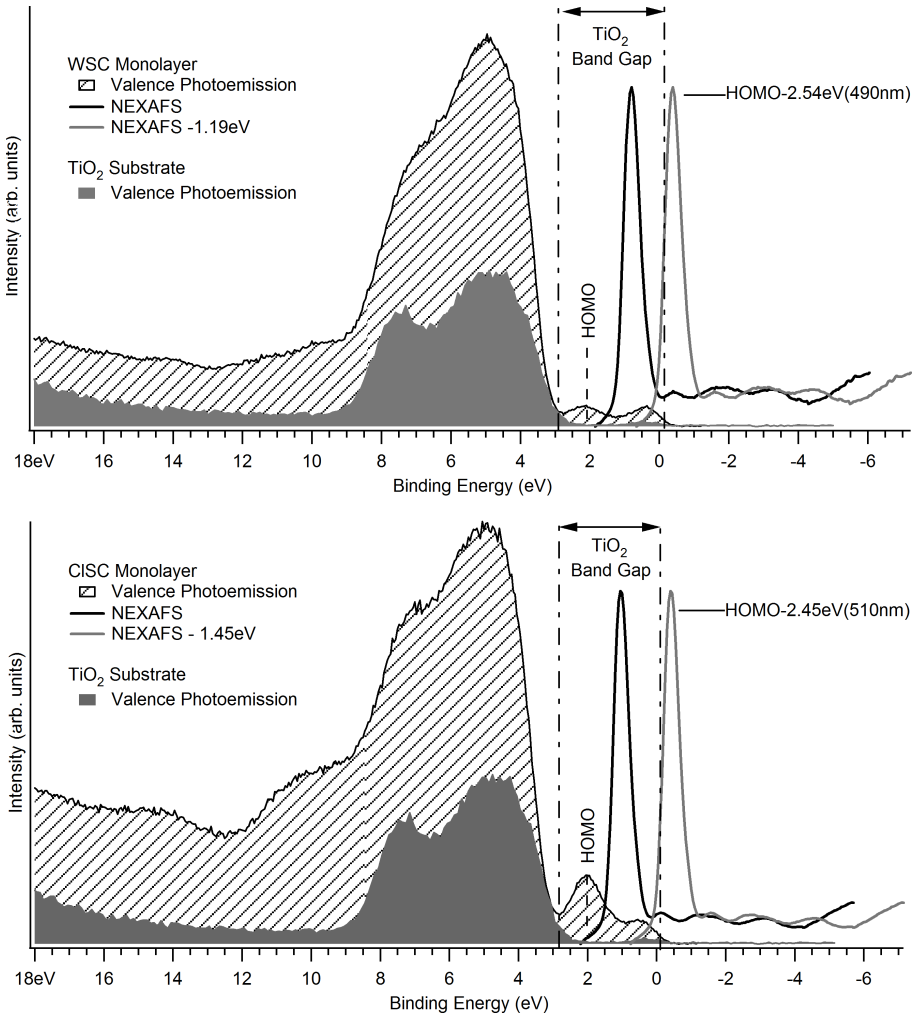

Figure 8.9: Valence band photoemission spectra of the clean substrate and of a monolayer of dye molecule, adjacent to a N 1*s* NEXAFS spectrum of the monolayer. The NEXAFS spectra are also shown shifted to align with the relevant optical HOMO-LUMO gap (shown in a lighter shade and labelled with the position of the measured HOMO minus the energy of the optical absorption). The photoemission spectra were measured using hν = 60 eV. The NEXAFS spectra were taken over the photon energy range hν = 398-406 eV.

in Chapter 6.[7] The lowest binding energy molecular peak in the valence photoemission spectra corresponds to the highest occupied molecular orbital (HOMO). The peak at lower binding energy is due to the substrate defect gap state, which is introduced when turning the substrate into a semiconductor as described in the method section previously. For each dye complex the HOMO is present within the substrate band gap which prevents back transfer of electrons from the substrate. The HOMO is located at a BE of 2.1 and 2.05 eV for the WSC and ClSC dye complexes respectively. The HOMO of each of these dye complexes is located at higher BE than the molecules studied earlier in Chapter 6. After charge transfer from the molecules to the substrate has occurred this could create a large potential to remove electrons from an attached water molecule.

In the present case where the unoccupied states are probed using N 1*s* NEXAFS a *core* exciton (bound electron-hole pair) is created, whereas in an optically excited system a *valence* exciton is created. The presence of a hole shifts the unoccupied states to higher binding energy with respect to the ground state. The BE of the excitons, equivalent to the amount by which the unoccupied levels shift, is attributed to a combination of the Coulomb interaction between the hole and the excited electron and the rehybridization of the molecular states upon core- or valence-hole creation.[66] Comparing the HOMO-LUMO gap for optical excitation (2.54 and 2.45 eV) to the HOMO-LUMO gap for the core-excited system (1.3 and 1 eV), the difference in energy is 1.2 and 1.45 $\pm$ 0.1 eV for the WSC and ClSC dye complexes respectively. This is indicative of the difference between the N 1*s* core exciton and valence exciton BEs for the molecules. These values are consistent with the difference in BE found for pyridine,[66] a molecule closely related to the bi-isonicotinic acid ligands of the dye complexes, especially concerning the chemical environment of the nitrogen atoms being probed here. Similar results for the difference in exciton BEs have previously been found for bipyridine based dye complexes such as N3.[7]

Shifting the NEXAFS spectra of each dye complex into line with the optical HOMO-LUMO gap as shown in Figure 8.9, causes the LUMO to lie above the conduction band edge. In a real water-splitting device this energetic overlap permits electron injection from the LUMO into the substrate for both dye complexes. The presence of a core exciton in the NEXAFS causes the LUMO of the core-excited systems to lie within the substrate band gap preventing charge transfer for this orbital.

8.3.3 Charge Transfer Dynamics

In water-splitting DSCs the initial step of the reaction is electron injection from the excited molecule into the substrate conduction band. RPES is used here to investigate

molecule-to-substrate charge transfer. This technique enables us to quantify the delocalization of charge from unoccupied molecular orbitals to the substrate on the low femtosecond time scale, previously demonstrated for the bi-isonicotinic acid ligand and the N3 dye complex as well as related molecules on TiO_2(110).[7, 115]

The core-hole clock implementation of RPES uses the fact that if charge transfer is occurring, it must be competing with the de-excitation of the excited state via resonant photoemission or resonant Auger. The time taken for de-excitation here can also be described as the lifetime of the N 1*s* core hole. Here we calculate the electron injection time from the LUMO+2 and LUMO+3 orbitals of both dye complexes. The electron injection time τ_{EI} for electrons moving from the unoccupied level of the molecule adsorbed to the substrate to unoccupied substrate states is given by Equation 8.3.1. The derivation of this equation was previously discussed in Section 4.3.3.

$$\tau_{EI} = \tau_{CH} \frac{I^{mono}_{RPES} / I^{mono}_{NEXAFS}}{I^{multi}_{RPES} / I^{multi}_{NEXAFS} - I^{mono}_{RPES} / I^{mono}_{NEXAFS}} \tag{8.3.1}$$

The variables I^{mono}_{RPES} and I^{multi}_{RPES} represent the intensities of the unoccupied peak being studied in the monolayer and multilayer respectively. These values are each normalized by the total cross sections as provided by the NEXAFS intensities I^{mono}_{NEXAFS} and I^{multi}_{NEXAFS}. The variable τ_{CH} is the average $N1s$ core-hole lifetime which has been measured as 6 fs.[119]

In the previous section it was shown that the LUMO of each molecule lies energetically within the substrate band gap when a core exciton is present, so the injection of an electron from this level into the substrate conduction band is energetically forbidden. Electron injection is however energetically allowed from higher unoccupied molecular orbitals that overlap with the conduction band of the substrate. As the LUMO, LUMO+2 and LUMO+3 of each dye complex are all thought to be located on the bi-isonicotinic acid ligands, it can be assumed that the coupling of these orbitals to the substrate and, therefore, the corresponding charge-transfer dynamics will be similar.

The experimental RPES data includes Auger peaks which need to be excluded from the charge transfer analysis, this is achieved by integrating over a selected BE window for both the monolayer and multilayer as shown in Figure 8.10. Any peaks at the energies of the LUMO+2 and LUMO+3 resonances are due solely to resonant photoemission, as normal photoemission contributes a sloping background only. The LUMO+1 is not considered for these dye complexes as it cannot be separated from the LUMO.

The RPES spectra are normalized to the intensity of the LUMO, as are the corresponding NEXAFS spectra which are also shown in Figure 8.11. In the NEXAFS spectra, the

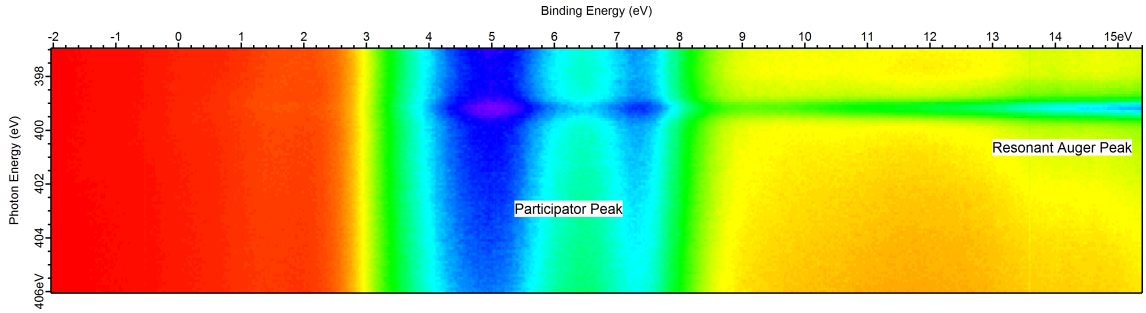

Figure 8.10: N 1*s* RPES spectrum of a monolayer of WSC molecules on rutile TiO_2(110) showing the BE integration window.

peaks represent the unoccupied levels' full intensities, whereas for RPES the LUMO has its full intensity but the other unoccupied levels may be depleted by charge transfer. For the multilayer it can be seen that the LUMO+2 and LUMO+3 peaks are smaller in the RPES than in the NEXAFS. Since no charge transfer to the substrate can occur in the multilayer this intensity reduction is attributed purely to matrix element effects due to the different techniques used.[116] The WSC LUMO+2 and LUMO+3 orbitals appear to have greater intensity in the NEXAFS spectra than the corresponding ClSC orbitals, this is likely due to greater overlap of the unoccupied orbitals with the HOMO in the WSC complex compared to the ClSC complex.

For several of the the WSC and ClSC monolayer RPES peaks there is no discernible peak at the same photon energy as the corresponding peak in the NEXAFS spectrum. For these peaks the level of noise is taken as an upper limit for the intensity of any peak that might be present. This is then used to calculate an upper limit for the charge transfer time according to Equation 8.3.1, the results are shown for each molecular orbital studied in Table 8.2. These values are in agreement with the upper limit on the time scale for charge transfer of both Ru 535 and the bi-isonicotinic acid ligand on TiO_2, which have previously been found to be 16 fs and 3 fs respectively.[7, 115] The LUMO+2 and LUMO+3 of both dye complexes appear to have greater intensity in the NEXAFS spectra than previously seen for the N3 based complexes seen in Chapter 6. The additional intensity of these orbitals allowed us to measure charge transfer on a faster timescale in this experiment. Previously attosecond timescale charge transfer has been observed using this technique on sulphur atoms on a Ruthenium surface,[128] this has also been observed in certain orbitals of the dipyrrin molecules studied in Chapter 7.

For resonant photoemission to occur following core excitation, the occupied and unoccupied orbitals involved must have some interaction. The largest probability for resonant photoemission occurs when both of the electrons involved in the transition are

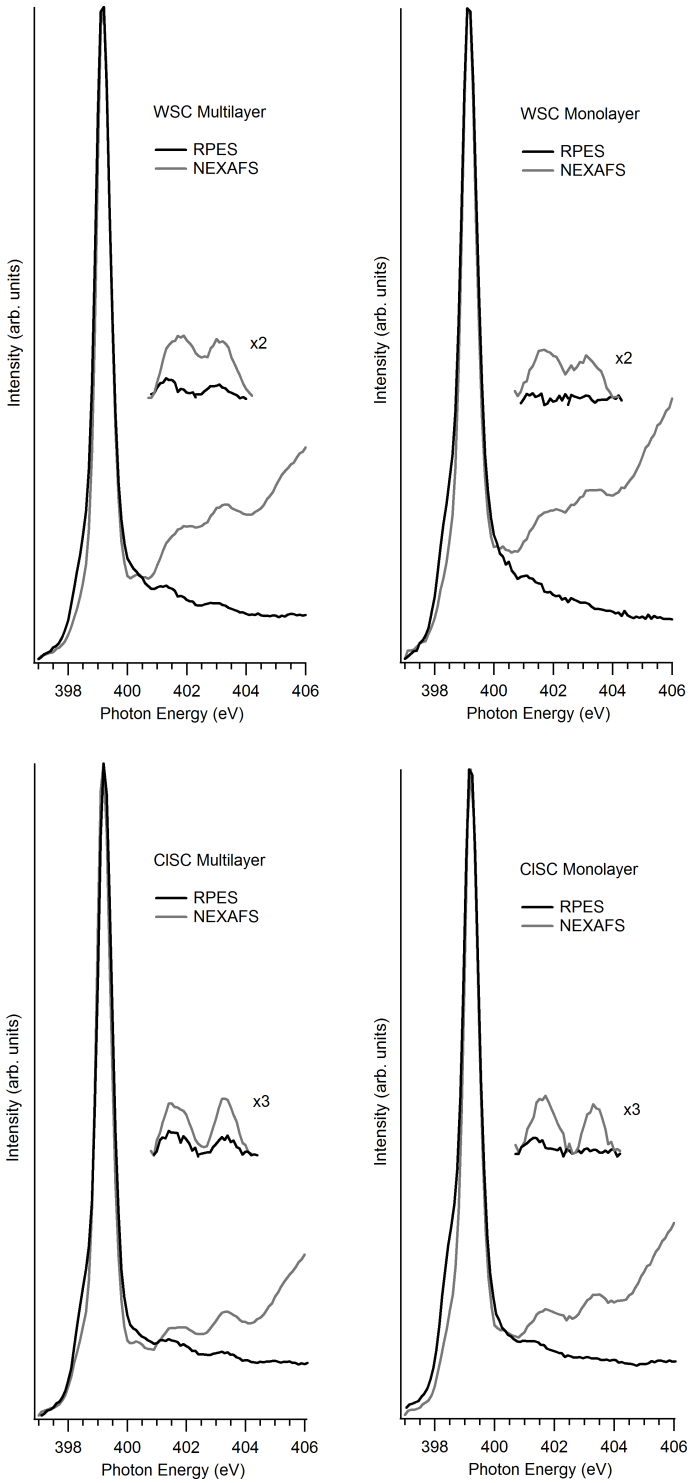

Figure 8.11: N 1*s* RPES and N 1*s* NEXAFS spectra of multilayers (left) and monolayers (right) of WSC (top row) and ClSC molecules (bottom row). The RPES spectra are BE integrations over a range which excludes the Auger peaks. Also shown are magnifications of the LUMO+2 and LUMO+3 region.

Table 8.2: Table of RPES/NEXAFS ratios for multilayer and monolayer coverages of WSC and ClSC dye molecules and the calculated upper limit on charge transfer timescale for each orbital studied.

Dye molecule	Orbital	Multilayer RPES/NEXAFS ratio	Monolayer RPES/NEXAFS ratio	Upper limit on charge transfer timescale (fs)
WSC	LUMO+2	0.458	0.066	2 ± 1
WSC	LUMO+3	0.440	0.055	1 ± 1
ClSC	LUMO+2	0.452	0.193	5 ± 1
ClSC	LUMO+3	0.466	0.050	1 ± 1

located on the same atom, specifically the site of the core-hole. Resonant photoemission is in essence a special type of Auger decay and whilst interatomic Auger transitions can occur,[123] the rates of these events are negligible in all but the lowest energy Auger processes.

In these experiments resonant photoemission requires some degree of overlap between the HOMO, LUMO and the core-excited atom, however in a real DSC only an overlap between the HOMO and LUMO is required for photoexcitation between the states. Figure 8.12 shows both complexes have a significant amount of overlap between their calculated HOMO and LUMO orbitals on the central ruthenium atom of the complex. This overlap should mean that photoexcitation with visible light is relatively favourable in these molecules.

8.4 Summary

UHV electrospray deposition has been used to deposit monolayers and multilayers of the WSC and ClSC dye complexes on the rutile TiO_2(110) surface *in situ*. Photoemission spectroscopy has been used to characterize the core and valence levels of the system, which were used to deduce the bonding geometry of each dye complex on the rutile TiO_2(110) surface. We find that for both dye complexes carboxylic acid groups deprotonate so that their oxygen atoms bond to titanium atoms on the substrate surface, this would suggest that the complexes adopt a 2M-bidentate bonding geometry on the rutile TiO_2(110) surface.

The energetic alignment of the system was determined by placing the valence photoemission and N 1*s* NEXAFS of a monolayer of each dye complex onto a common BE scale. The bandgap of TiO_2(110) was aligned using the valence photoemission of the

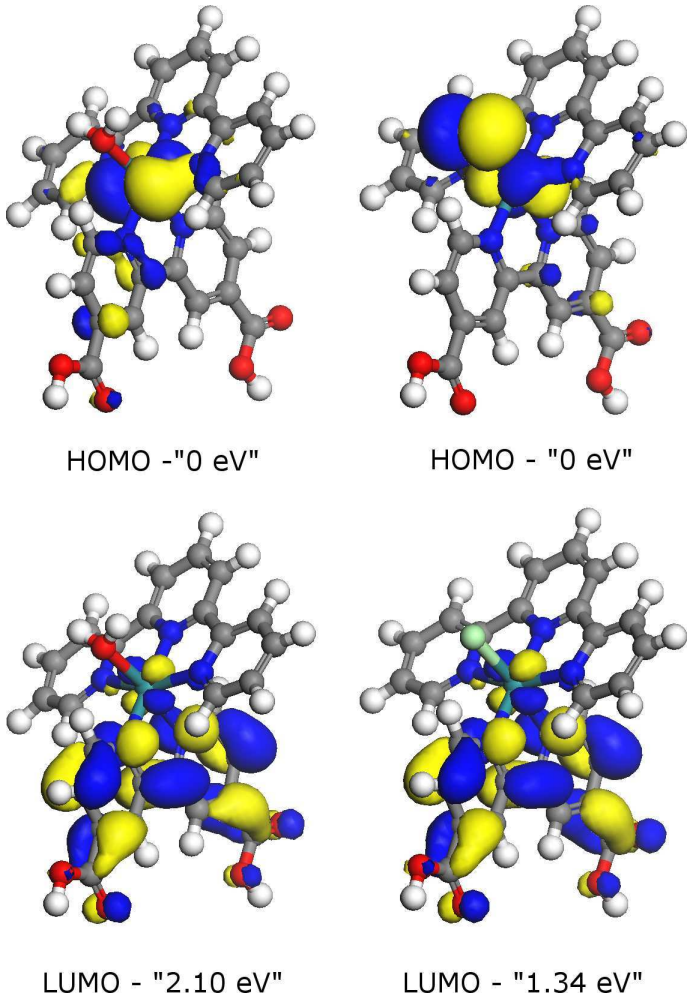

Figure 8.12: DFT calculations showing several molecular orbitals of a geometry-optimized free WSC molecule (top) and ClSC molecule (bottom) together with calculated orbital energies.

clean substrate. The optical absorption maximum for each dye complex was attributed to the HOMO→LUMO transition in a working solar cell. This was used to compare the energetics as they would appear for photoexcitation from the valence band (as occurs in working DSCs) with those found for photoexcitation from the N 1*s* core level, for which the unoccupied levels appear at higher BE. This comparison allowed quantification of the difference in BE of a core and valence excitation for each dye complex system, found to be 1.2 and 1.45 $\pm$ 0.1 eV. for the WSC and ClSC dye complexes respectively. The energetic alignments reveal that the LUMO of each dye complex is incapable of charge transfer to the substrate when a core exciton is created, this means the LUMO can be used as a reference to calculate charge transfer timescale of the WSC. The energetic alignment diagrams also show that the dye complexes are capable of charge transfer from their LUMO when optically excited whilst adsorbed on the rutile TiO_2(110) surface. This shows that rutile TiO_2(110) could be an appropriate substrate for a single centre water-splitting DSC.

The valence band photoemission spectra show that the HOMO of the WSC and ClSC dye complexes occur at far higher BE than those previously seen for the N3 dye complex and related molecules each of which contains two or more bipyridine like ligands.[7, 96] The difference between the BEs is attributed to the difference in electron densities on the central ruthenium ion, which is caused by the difference in electronegativity of the attached ligands. In a water-splitting dye complex the potential to remove electrons from a water molecule is created by a hole in the HOMO. The HOMO becomes an electron acceptor after losing an electron and having a higher binding energy will make the HOMO a better electron acceptor. The HOMO would therefore be better at removing electrons from water molecules which will aid the water-splitting reaction.

The core-hole clock implementation of RPES was used to find that electron injection from the LUMO+2 and LUMO+3 of each dye complex to the substrate can occur on the sub-femtosecond timescale. Previous experiments on N3 and related molecules as seen in Chapter 6 have shown femtosecond charge transfer. As with the dipyrrin molecules in Chapter 7 the improvement is likely down to the increased intensity of the LUMO+2 and LUMO+3 orbitals for the WSC and ClSC complexes leading to a reduction in the uncertainty of the measurements. It is thought that the studied orbitals and the LUMO of each dye complex are all located on the bi-isonicotinic acid ligands, so electron injection in valence excited systems is expected to occur in a similar time scale. This information can be used to design better single and multi-centre dye complexes to catalyse the water-splitting process.

CHAPTER 9

Summary

The transfer of an excited electron to a substrate is a key process in both photovoltaic and photocatalytic dye-sensitized solar cell devices. To help determine what factors affect the efficiency of charge transfer we studied different groups of molecules with slightly different chemical structures adsorbed onto a TiO_2(110) surface. The bipyridine-based dye complexes included the N3 molecule which is currently one of the most efficient dye sensitizers for photovoltaic DSCs as well as two molecules with three bipyridine-based ligands. Another group of dye complexes had carboxylic acid groups on dipyrrin-based ligands which would cause the complexes to adopt a different bonding geometry than the bipyridine complexes on the TiO_2 surface. A single centre water-splitting complex was also studied which has a similar structure to N3 but with a terpyridine-based ligand instead of bipyridine and a water molecule attached to the metal centre. The importance of both photovoltaic and photocatalytic DSC devices is discussed in Chapter 1.

All of the molecules studied were organic and would not remain intact using standard ultra-high vacuum (UHV) deposition techniques. Electrospray deposition was used to deposit the molecules onto a surface held under high vacuum conditions. This deposition method allows us to prepare in situ samples onto a surface cleaned in UHV conditions. The number of layers of molecules on the surface can be controlled by altering the deposition time or pressure and the coverage can be increased by translating the substrate during deposition. Electrospray deposition is described in detail in Chapter 5.

Samples were studied using synchrotron light which causes the emission of electrons from the surface allowing us to use several different types of electron spectroscopy to examine the samples. The production of useable synchrotron radiation is described in Chapter 2. Density functional theory (DFT) calculations were also performed to

help interpret experimental results. The data collected was used to examine how the molecules adsorb to the surface as described in Chapter 3 and charge transfer from the molecule to the surface as described in Chapter 4.

The results for the bipyrdine-based dye complexes adsorbed on rutile TiO_2(110) are presented in Chapter 6. The photoemission data reveals that all of the molecules are most likely to bond to the surface using two carboxylic acid groups. The DFT calculations revealed that Ru 470 bonds to the surface using carboxylic acid groups from two different bi-isonicotinic acid ligands unlike the other two molecules studied, this is most likely due to interactions with other Ru 470 molecules on the surface. Valence band photoemission revealed that Ru 455 and Ru 470 had their highest occupied molecular orbital (HOMO) at a higher binding energy than the N3 dye complex most likely due to changes in electron density on the central ruthenium atom. The HOMO is important to the water-splitting process so the change in binding energy may significantly affect the efficiency of water-splitting or other photocatalytic reactions.

Energetic alignments were performed on each molecule by combining valence photoemission spectra and nitrogen near-edge x-ray absorption fine structure (NEXAFS) spectra on a common binding energy scale. The lowest energy transition in the optical absorption spectra was assigned to a HOMO to lowest unoccupied molecular orbital (LUMO) transition, this allows us to determine how far the NEXAFS spectra would shift in binding energy for a valence hole instead of the core hole created during experiments. The alignments revealed the LUMO of each molecule would be capable of charge transfer to a TiO_2 substrate when optically excited as would occur in a working solar cell.

Charge transfer timescales calculated using the core-hole clock implementation of resonant photoemission (RPES) revealed that the Ru 470 molecule was substantially less efficient than the other two complexes at charge transfer to the TiO_2(110) surface. The Ru 470 molecule still had significant intensity on the LUMO+2 and LUMO+3 peaks in the monolayer RPES spectra, whilst the orbitals of the other two molecules were reduced to the level of noise. This suggests that either the bonding geometry adopted by Ru 470 or the stronger intermolecular interactions could make this complex less efficient at charge transfer. Charge transfer was found to occur in the range of 12-21 femtoseconds for all three molecules in agreement with previous studies of N3 and related molecules.

Dipyrrin-based complexes adsorbed onto rutile TiO_2(110) were studied in Chapter 7. Photoemission spectra revealed that both dye complexes bonded to the TiO_2 surface using both of the available carboxylic acid groups on the dipyrrin ligands. DFT simula-

tions were used to determine the lowest energy bonding geometry which revealed the most likely bonding geometry had bonding rows of oxygen atoms in the surface separated by a non-bonding row of oxygen atoms. Energetic alignments were performed for both molecules using the dipyrrin nitrogen peak and the bipyridine nitrogen peak for the PY2 complex. The different alignments were performed as the PY2 complex has unoccupied from the different ligands and the orbitals are not thought to mix. The alignments showed that each LUMO is capable of charge transfer when optically excited as in a real DSC device.

Charge transfer timescales were measured for the dipyrrin molecules and were discovered to be in the low to sub-femtosecond region. The very low charge transfer timescales measured are likely due to excellent signal-to-noise ratio due to the combination of RPES spectra and the very high intensity of the LUMO peaks studied compared to the bipyridine-based dye complexes of Chapter 6. The orbitals studied here and the orbitals used in a working solar cell are thought to exist on the same region of the molecule, meaning that charge transfer in a working solar cell should occur in approximately the same timescale.

The single-centre water-splitting complex adsorbed on rutile TiO_2(110) was studied in Chapter 8. The photoemission and DFT data suggested that the molecule adsorbs to the TiO_2 surface in the same 2M-bidentate bonding geometry as N3. Energetic alignments performed on this molecule revealed that the LUMO would be capable of charge transfer in a real DSC when optically excited.

The core-hole clock implementation of RPES revealed that these molecules are capable of electron injection to the TiO_2 substrate with upper limits in the range of 0.8 to 4.5 femtoseconds. These timescales are lower compared with the bipyridine-based complexes studied in Chapter 6, the reduction is attributed to the increased intensity of the LUMO+2 and LUMO+3 features in these molecules and better signal to noise ratio in the experiments. As the LUMO, LUMO+2 and LUMO+3 orbitals are all thought to be located on the same part of the complex it is expected that charge transfer in a working solar cell will occur on a similar timescale.

The charge transfer results for the water-splitting complex and the dipyrrin-based complexes include some of the first measurements of sub-femtosecond electron injection for an organic molecule adsorbed onto a surface. This study has provided valuable insights into the electronic and geometric structures of molecules that could potentially be used as either photovoltaic or photocatalytic dye sensitizers for DSC devices. This information could help to improve the design of future dye sensitizers making DSCs more efficient at producing sustainable electricity and fuel.

In future experiments it would be interesting to study working solar cells based on these dye sensitizers to determine how closely these experimental results are related to performance in a real solar cell. Using the techniques described in this thesis it would be interesting to study the N3 dye complex co-adsorbed onto a TiO_2 surface with guanidinium thiocyanate as this has been previously shown to increase the efficiency of a photovoltaic DSC. It would also be interesting to study charge transfer to a nanostructured semiconductor that helps to prevent charge recombination after the molecule transfers an electron to the surface. This may be especially important when studying photocatalytic systems where recombination could severely impact the reaction.

Studying charge transfer between the metal centres of a multi-centre dye complex could be useful as this factor is likely to be crucial to the efficiency of a multi-centre photocatalytic dye complex. This may be possible using RPES by using two different elements for the metal centres allowing us to study charge transfer for each centre in a single dye complex. DFT studies of multi-centre dye complexes could be used to calculate and optimise the molecular orbitals needed for charge transfer to the surface and between the metal centres. Calculations could also be performed on intermediate states of the dye complex during the reaction to optimise each step of the water-splitting process. Experiments using ultrafast time-resolved spectroscopy could allow us to examine the intermediate states in the water-splitting cycle once water is introduced to the sensitized surface.

9.1 List of publications

- **Charge transfer from adsorbed ruthenium-based photosensitiser through an ultra-thin aluminium oxide layer and into a metallic substrate**
  Andrew J. Gibson, Robert H. Temperton, Karsten Handrup, Matthew Weston, Louise C. Mayor and James N. O'Shea
  Submitted to J. Chem. Phys. (2014)

- **Single molecule magnets with protective ligand shells on gold and titanium dioxide surfaces: In situ electrospray deposition and x-ray absorption spectroscopy**
  Karsten Handrup, Victoria J. Richards, Matthew Weston, Neil R. Champness and James N. O'Shea
  J. Chem. Phys, **139**, 154708 (2013)

- **Experimental observation of sub-femtosecond charge transfer in a model water-splitting dye-sensitized solar cell**
  Matthew Weston, Karsten Handup, Thomas J. Reade, Neil R. Champness and James N. O'Shea.
  J. Chem. Phys, **137**, 224706 (2012)

- **Adsorption of dipyrrin-based dye complexes on a rutile TiO2(110) surface**
  Matthew Weston, Thomas J. Reade, Karsten Handup, Neil R. Champness and James N. O'Shea
  J. Phys. Chem. C, **116**, 18184 (2012)

- **Charge transfer from an aromatic adsorbate to a semiconductor TiO_2 surface probed on the femtosecond time scale with resonant inelastic x-ray scattering**
  Andrew J. Britton, Matthew Weston and James N. O'Shea
  Phys. Rev. Lett, **109** 017401 (2012)

- **Charge transfer interactions of a Ru(II) dye complex and related ligand molecules adsorbed on Au(111)**
  Andrew J. Britton, Matthew Weston, J. Ben Taylor, Anna Rienzo, Louise C. Mayor and James N. O'Shea
  J. Chem. Phys. **135** 164702 (2011)

- **A single centre water-splitting dye complex adsorbed on rutile TiO_2(110): Photoemission, x-ray absorption and optical spectroscopy**
  Matthew Weston, Thomas J. Reade, Andrew J. Britton, Karsten Handrup, Neil R.

Champness and James N. O'Shea
J. Chem. Phys, **135**, 114703 (2011)

- **Charge transfer dynamics of model charge transfer centres of a multi-centre water-splitting dye complex on rutile TiO_2(110)**
  Matthew Weston, Andrew J. Britton and James N. O'Shea
  J. Chem. Phys. **134**, 054705 (2011)

9.2 List of acronyms

BE - Binding energy

ClSC - (2,2′-bipyridyl-4,4′-dicarboxylic acid)-(2,2′:6′,6″-terpyridine)chloride Ruthenium(II)

DMSO - dimethylsulfoxide

DSC - dye-sensitized solar cell

DFT - Density functional theory

ESD - Electrospray deposition

GGA - Generalised gradient approximation

HOMO - Highest occupied molecular orbital

KE - kinetic energy

LUMO - Lowest unoccupied molecular orbital

NEXAFS - Near-edge X-ray absorption fine structure

PEEK - polyetheretherketone

PES - Photoemission spectroscopy

PY1 - bis(5-(4-carboxyphenyl)-4,6-dipyrrin)bis(dimethylsulfoxide)Ruthenium(II)

RPES - Resonant photoemission spectroscopy

PY2 - bis(5-(4-carboxyphenyl)-4,6-dipyrrin)(2,2′-bipyridine)Ruthenium(II)

Ru 455 - cis-bis(2,2′-bipyridyl)-(2,2′-bipyridyl-4,4′-dicarboxylic acid) ruthenium(II)

Ru 470 - tris(2,2′-bipyridyl-4,4′-dicarboxylic acid) ruthenium(II)

Ru 535/N3 - cis-bis(isothiocyanato)bis(2,2′-bipyridyl-4,4′-dicarboxylato)-ruthenium(II)

UHV - Ultra-high vacuum

UV - Ultraviolet

WSC - aqua(2,2′-bipyridyl-4,4′-dicarboxylic acid)-(2,2′:6′,6″-terpyridine) Ruthenium(II)

XPS - X-ray photoemission spectroscopy

List of Figures

References

[1] 'U.S. energy information administration'. Historical energy consumption, 2011. URL .

[2] P. Forster, V. Ramaswamy, P. Artaxo, T. Berntsen, R. Betts, D. W. Fahey, J. Haywood, J. Lean, D. C. Lowe, G. Myrhe, J. Nganga, R. Prinn, G. Raga, M. Schulz, and R. Van Dorland. *Changes in atmospheric constituents and radiatiove forcing. In: climate change 2007: The physical science basis. Contribution of working group I to the fourth assessment report to the fourth assessment report of the intergovernmental panel on climate change*. Cambridge University Press, Cambridge ,UK and New York NY, USA, 2007.

[3] S. H. Schneider, S. Semenov, A. Patwardhan, I. Burton, C. H. D. Magadza, M. Oppenheimer, A. B. Pittock, A. Rahman, J. B. Smith, A. Suarez, and F. Yamin. *Assessing key vulnerabilities and the risk from climate change. Climate Change 2007: Impacts, Adaptation and Vulnerability. Contribution of Working Group II to the Fourth Assessment Report of the Intergovernmental Panel on Climate Change*. Cambridge University Press, Cambridge ,UK and New York NY, USA, 2007.

[4] M. Grätzel. Photovoltaic and photoelectrochemical conversion of solar energy. *Phil. Trans. R. Soc. A*, 365:993, 2007.

[5] M. Grätzel. Photoelectrochemical cells. *Nature*, 414:338, 2001.

[6] B. O'Regan and M. Grätzel. A low-cost, high-efficiency solar cell based on dye-sensitized colloidal tio2 films. *Nature*, 353:737, 1991.

[7] L. C. Mayor, J. B. Taylor, G. Magnano, A. Rienzo, C. J. Satterley, J N. OŠShea, and J. Schnadt. Photoemission, resonant photoemission, and x-ray absorption of a ru(ii) complex adsorbed on rutile tio_2(110) prepared by in situ electrospray deposition. *J. Chem. Phys.*, 129:114701, 2008.

[8] M. K. Nazeeruddin, A. Kay, I. Rodicio, R. Humphry-Baker, E. Müller, P. Liska, N. Vlachopoulos, and M. Gratzel. Conversion of light to electricity by cis-

x2bis(2,2′-bipyridyl-4,4′-dicarboxylate)ruthenium(ii) charge transfer sensitizers (x = cl-, br-, i-, cn- and scn-) on nanocrystalline tio2 electrodes. *J. Am. Chem. Soc.*, 115:6382, 1993.

[9] M. Grätzel. Conversion of sunlight to electric power by nanocrystalline dye-sensitized solar cells. *J. Photochem. Photobiol. A*, 164:3, 2004.

[10] M. K. Nazeeruddin, P. Pechy, T. Renouard, S. M. Zakeeruddin, R. Humphry-Baker, P. Comte, P. Liska, L. Cevey, E. Costa, V. Shklover, L. Spiccia, G. B. Deacon, C. A. Bignozzi, and M. Gratzel. Engineering of efficient panchromatic sensitizers for nanocrystalline tio2-based solar cells. *J. Am. Chem. Soc.*, 123:1613, 2001.

[11] M. Grätzel. Solar energy conversion by dye-sensitized solar cells. *Inorg. Chem.*, 44:6841, 2005.

[12] H. Tsubomura, M. Matsumura, Y. Noyamaura, and T. Amamiya. Dye sensitized zinc oxide: aqueous electrolyte: platinum photocell. *Nature*, 261:402, 1976.

[13] M. Matsumura. Phd thesis. *Osaka University*, page Japan, 1979.

[14] L. Patthey, H. Rensmo, P. Persson, K. Westermark, L. Vayssieres, A. Stashans, Å. Petersson, P. A. Brühwiler, H. Siegbahn, S. Lunell, and N. Mårtensson. Adsorption of bi-isonicotinic acid on rutile tio2(110). *J. Chem. Phys.*, 110:5913, 1999.

[15] A. Thomas, W. Flavell, C. Chatwin, S. Rayner, D. Tsoutson, A. Kumarasinghe, D. Brete, T. Johal, S. Patel, and J. Purton. Adsorption of bi-isonicotinic acid on anatase tio2(101) and (001) studied by photoemission amd nexafs spectroscopy. *Surf. Sci.*, 592:159, 2005.

[16] D. C. Cronemeyer. Electrical and optical properties of rutile single crystals. *Phys. Rev.*, 87:876, 1952.

[17] P. Wang, B. Wenger, R. Humphry-Baker, J. E. Moser, J. Teuscher, W. Kantlehner, J. Mezger, E. V. Stoyanov, S. M. Zakeeruddin, and M. Grätzel. Charge separation and efficient light energy conversion in sensitized mesoscopic photoelectrochemical cells based on binary ionic liquids. *J. Am. Chem. Soc.*, 127:6850, 2005.

[18] S. A. Haque, E. Palomeras, H. M. Upadhyaya, L. Otley, R. J. Potter, A. B. Holmes, and J. R. Durrant. Flexible dye sensitised nanocrystalline semiconductor solar cells. *Chem. Comm.*, 24:3008, 2003.

[19] U. Bach, D. Lupo, P. Comte, J. E. Moser, F. Weissörtel, J. Salbeck, H. Spreitzer, and M. Grätzel. Solid state dye sensitized mesoporous tio2 solar cells with high photon-to-current conversion efficiencies. *Nature*, 395:583, 1998.

[20] B. O'Regan and D. T. Schwartz. Solid state photoelectrochemical cells based on dye sensitization. *AIP Conf. Proc.*, 404:129, 1997.

[21] V. P. S. Perera, P. K. D. D. P. Pitigala, P. V. V. Jayaweera, K. M. P. Bandaranayake, and K. Tennakone. Dye-sensitized solid-state photovoltaic cells based on dye multilayersemiconductor nanostructures. *J. Phys. Chem. B*, 107:13758, 2003.

[22] M. Grätzel. Dye-sensitized solar cells. *J. Photochem. Photobiol. C*, 4:145, 2003.

[23] A. C. Dillon, K. M. Jones, T. A. Bekkedahl, C. H. Kiang, D. S. Bethune, and M. J. Heben. Storage of hydrogen in single-walled carbon nanotubes. *Nature*, 386:377, 1997.

[24] C. Liu, Y. Y. Fan, M. Liu, H. T. Cong, H. M. Cheng, and M. S. Desselhaus. Hydrogen storage in single-walled carbon nanotubes at room temperature. *Science*, 286:1127, 1999.

[25] L. Schlapbach and A. Zttel. Hydrogen-storage materials for mobile applications. *Nature*, 414:353, 2001.

[26] N. L. Rosi, J. Eckert, M. Eddaoudi, D. T. Vodak, J. Kim, M. O'Keefe, and O. M. Yaghi. Hydrogen storage in microporous metal-organic frameworks. *Science*, 300:1127, 2003.

[27] S. H. Yang, X. Lin, A. J. Blake, G. S. Walker, P. Hubberstey, N. R. Champness, and M. Schröder. Cation induced kinetic trapping and enhanced hydrogen adsorption in a modulated anionic metal-organic framework. *Nature Chem.*, 1:487, 2009.

[28] X. Lin, I. Telepeni, A. J. Blake, A. Dailly, C. M. Brown, J. M. Simmons, M. Zoppi, G. S. Walker, K. M. Thomas, T. J. Mays, P. Hubberstey, N. R. Champness, and M. Schröder. High capacity hydrogen adsorption in cu(ii) tetracarboxylate framework materials: The role of pore size, ligand functionalization, and exposed metal sites. *J. Am. Chem. Soc.*, 131:2159, 2009.

[29] J.J. Concepcion, J. W. Jurss, M. R. Norris, Z. F. Chen, J. L. Templeton, and T. J. Meyer. Catalytic water oxidation by single-site ruthenium catalysts. *Inor. Chem.*, 49:1277, 2010.

[30] J.J. Concepcion, J. W. Jurss, J. L. Templeton, and T. J. Meyer. One site is enough. catalytic water oxidation by [ru(tpy)(bpm)(oh2)](2+) and [ru(tpy)(bpz)(oh2)](2+). *J. Am. Chem. Soc.*, 49:16462, 2008.

[31] J.J. Concepcion, J. W. Jurss, M. K. Brennaman, P. G. Hoertz, A. O. T. Patrocinio, N. Y. M. Iha, J. L. Templeton, and T. J. Meyer. Making oxygen with ruthenium complexes. *Acc. Chem. Res.*, 42:1954, 2009.

[32] D. J. Wasylenko, C. Ganesamoorthy, B. D. Kolvisto, M. A. Henderson, and C. P. Berlinguette. Insight into water oxidation by mononuclear polypyridyl ru catalysts. *Inorg. Chem.*, 49:2202, 2010.

[33] D. J. Wasylenko, C. Ganesamoorthy, M. A. Henderson, B. D. Kolvisto, H. D. Osthoff, and C. P. Berlinguette. Electronic modification of the [ruii(tpy)(bpy)(oh2)]2+ scaffold: Effects on catalytic water oxidation. *J. Am. Chem. Soc.*, 132:16094, 2010.

[34] S. Masaoka and K. Sakai. Clear evidence showing the robustness of a highly active oxygen-evolving mononuclear ruthenium complex with an aqua ligand. *Chem. Lett.*, 38:182, 2009.

[35] W. C. Ellis, N. D. McDaniel, S. Bernhard, and T. J. Collins. Fast water oxidation using iron. *J. Am. Chem. Soc.*, 132:10990, 2010.

[36] N. D. McDaniel, F. J. Coughlin, L. J. Tinker, and S. Bernhard. Cyclometalated iridium(iii) aquo complexes: Efficient and tunable catalysts for the homogeneous oxidation of water. *J. Am. Chem. Soc.*, 130:210, 2008.

[37] A. Savini, G. Bellachioma, G. Ciancaleoni, C. Zuccaccia, D. Zuccaccia, and A. Macchioni. Iridium(iii) molecular catalysts for water oxidation: the simpler the faster. *Chem. Commun.*, 46:9218, 2010.

[38] E. D. Cline, S. E. Adamson, and S. Bernhard. Homogeneous catalytic system for photoinduced hydrogen production utilizing iridium and rhodium complexes. *Inorg. Chem.*, 47:10378, 2008.

[39] D. J. Wasylenko, C. Ganesamoorthy, J. Borau-Garcia, and C. P. Berlinguette. Electrochemical evidence for catalytic water oxidation mediated by a high-valent cobalt complex. *Chem. Commun.*, 47:4249, 2011.

[40] A. H. Rendondo, E. C. Constable, and C. E. Housecroft. Towards sustainable dyes for dye-sensitized solar cells. *Chimia*, 63:205, 2009.

[41] E. C. Constable, A. H. Rendondo, C. E. Housecroft, M. Neuburger, and S. Schaffner. Copper(ii) complexes of 6,6'-disubstituted 2,2'-bipyridine dicarboxylic acids: new complexes for incorporation into copper-based dye sensitized solar cells (dscs). *Dalt. Trans.*, 33:6634, 2009.

[42] E. C. Kwok, M. Chan, K. M. Wong, W. H. Lam, and V. W. Yam. Functionalized alkynylplatinum(ii) polypyridyl complexes for use as sensitizers in dye-sensitized solar cells. *Chem. Eur. J.*, 16:12244, 2010.

[43] C. L. Linfoot, P. Richardson, K. L. McCall, J. R. Durrant, A. Morandeira, and N. Robertson. A nickel-complex sensitiser for dye-sensitised solar cells. *Solar Energy*, 85:1195, 2011.

[44] E. I. Mayo, K. Kilså, T. Tirrell, P. I. Djurovich, A. Tamayo, M. E. Thompson, N. S. Lewis, and H. B. Gray. Cyclometalated iridium(iii)-sensitized titanium dioxide solar cells. *Photochem. Photobiol. Sci.*, 5:871, 2006.

[45] M. Hahlin, E. M. J. Johansson, S. Plogmaker, M. Odelius, D. P. Hagberg, L. Sun, H. Siegbahn, and H. Rensmo. Electronic and molecular structures of organic dye/tio2 interfaces for solar cell applications: a core level photoelectron spectroscopy study. *Phys. Chem. Chem. Phys.*, 12:1507, 2010.

[46] T. Marinado, M. Hahlin, X. Jiang, M. Quintana, E. M. J. Johansson, E. Gabrielsson, S. Plogmaker, D. P. Hagberg, G. Boschloo, S. M. Zakeeruddin, M. Grätzel, H. Siegbahn, L. Sun, A. Hagfeldt, and H. Rensmo. Surface molecular quantification and photoelectrochemical characterization of mixed organic dye and coadsorbent layers on tio2 for dye-sensitized solar cells. *J. Phys. Chem. C*, 114:11903, 2010.

[47] R. D. Schaller and V. I. Klimov. High efficiency carrier multiplication in pbse nanocrystals: implications for solar energy. *Phys. Rev. Lett*, 92:186601, 2004.

[48] A. H. Ip, S. M. Thon, S. Hoogland, O. Voznyy, D. Zhitomirsky, R. Debnath, L. Levina, L. R. Rollny, G. H. Carey, A. Fischer, K. W. Kemp, I. J. Kramer, Z. Ning, A. J. Labelle, K. W. Chou, A. Amassian, and E. H. Sargent. Hybrid passivated colloidal quantum dot solids. *Nature Nano.*, 7:577, 2012.

[49] J. Burschka, N. Pellet, S. Moon, R. Humphry-Baker, P. Gao, M. K. Nazeeruddin, and M. Grätzel. Sequential deposition as a route to high-performance perovskite-sensitized solar cells. *Nature*, 499:316, 2013.

[50] The MAGIC collaboration. Observation of pulsed γ-rays above 25 gev from the crab pulsar with magic. *Science*, 321:1183, 2008.

[51] NASA, ESA, J. Hester, and A. Loll. Hubble space telescope image of the crab galaxy, March 2011. URL .

[52] 'Synchrotron'. Wikipedia, March 2011. URL .

[53] Hasylab. Undulator schematic, March 2009. URL .

[54] R. Nyholm, J. N. Andersen, U. Johansson, B. N. Jensen, and I. Lindau. Beamline i311 at max-lab: a vuv/soft x-ray undulator beamline for high resolution electron spectroscopy. *J. Elec. Spec. Rel. Phen.*, 467-468:520, 2001.

[55] R. Denecke, P. Vaterlein, M. Bassler, N Wassdahl, S. Butorin, A. Nilsson, J. E. Rubensson, J. Nordgren, N. Martensson, and R. Nyholm. Beamline i511 at max ii: capabilities and performance. *J. Elec. Spec. Rel. Phen.*, 103:971, 1999.

[56] R. Nyholm, S. Svensson, J. Nordgren, and A. Flodstrom. A soft x-ray monochromator for the max synchrotron radiation facility. *Nucl. Instr. and Meth. A*, 246:267, 1986.

[57] 'Maxlab'. D1011 schematic, March 2013. URL .

[58] A. Tiwari and M. Snure. Synthesis and characterization of zno nano-plant-like electrodes. *Journal of nanoscience and nanotechnology*, 8:3981, 2008.

[59] E. Bequerel. Recherches sur les effets de la radiation chimique de la lumiere solaire, au moyen des courants electriques. *C. R. Acad. Sci.*, 9:145, 1839.

[60] D. Richfield. http://en.wikipedia.org/wiki/file:auger$_{y}ield.svg.Wikimedia$ *Commons*, *January*200

[61] D. A. Shirley. High-resolution x-ray photoemission spectrum of valence bands of gold. *Phys. Rev. B*, 5:4709–4714, 1972.

[62] M. P. Seah and W. A. Dench. Quantitative electron spectroscopy of surfaces: A standard data base for electron inelastic mean free paths in solids. *Surf. Interface Anal.*, 1:2, 1979.

[63] B. Delley. An all-electron numerical method for solving the local density functional for polyatomic molecules. *J. Chem. Phys.*, 92:508, 1990.

[64] B. Delley. From molecules to solids with the dmol3 approach. *J. Chem. Phys.*, 113:7756, 2000.

[65] K. Capelle. A bird's eye view of density-functional theory (version 5). *cond-mat*, page 0211443, 2006.

[66] J. Schnadt, J. Schiessling, and P. A. Brühwiler. Comparison of the size of excitonic effects in molecular pi systems as measured by core and valence spectroscopies. *Chem. Phys.*, 312:39, 2005.

[67] J. Schnadt, J. N. O'Shea, L. Patthey, J. Krempaský, N. Mårtensson, and P. A. Brühwiler. Alignment of valence photoemission, x-ray absorption, and substrate density of states for an adsorbate on a semiconductor surface. *Phys. Rev. B*, 67:235420, 2003.

[68] P. A. Brühwiler, O. Karis, and N. Mårtensson. Charge-transfer dynamics studied using resonant core spectroscopies. *Rev. Mod. Phys.*, 74:703, 2002.

[69] W. Wurth and D. Menzel. Ultrafast electron dynamics at surfaces probed by resonant auger spectroscopy. *Chem. Phys.*, 251:141, 2000.

[70] B. B. Smith and A. J. Nozik. A wave packet model for electron transfer and its implications for the semiconductor-liquid interface. *J. Phys. Chem. B*, 103:9915, 1999.

[71] C. O Almbladh. Effects of incomplete phonon relaxation on x-ray emission edges in simple metals. *Phys. Rev. B*, 16:4343, 1977.

[72] G. D. Mahan. Emission spectra and phonon relaxation. *Phys. Rev. B*, 15:4587, 1977.

[73] C. O Almbladh, A. L. Morales, and G. Grossman. Theory of auger core-valence-valence processes in simple metals. i. total yields and core-level lifetime widths. *Phys. Rev. B*, 39:3489, 1989.

[74] C. M. Whitehouse, R. N. Dreyer, M. Yamashita, and J. B. Fenn. Electrospray interface for liquid chromatographs and mass spectrometers. *Anal. Chem.*, 57:675, 1985.

[75] J. B. Fenn, M. Mann, C. K. Meng, S. F. Wong, and C. M. Whitehouse. Electrospray ionization for mass spectrometry of large biomolecules. *Science*, 246:64, 1989.

[76] 'The Nobel Foundation'. Nobelprize.org, May 2011. URL .

[77] S. Rauschenbach, F. L. Stadler, E. Lunedei, N. Malinowski, S. Koltsov, G. Costantini, and K. Kern. Electrospray ion beam deposition of clusters and biomolecules. *Small*, 2: 540, 2006.

[78] S. Koike and K. Tatsumi. Preparation and performances of highly porous layered licoo2 films for lithium batteries. *J. Power Sources*, 174:976, 2007.

[79] S. Koike and K. Tatsumi. Thin-film fabrication method for organic light-emitting diodes using electrospray deposition. *Adv. Mater.*, 21:1, 2009.

[80] C. M. Ghimbeu, M. Lumbreras, M. Siadat, and J. Schoonman. Detection of pollutant gases using electrostatic sprayed indium oxide and tin-doped indium oxide. *Mat. Chem. Phys.*, 114:933, 2009.

[81] C. M. Ghimbeu, J. Schoonman, M. Lumbreras, and M. Siadat. Electrostatic spray deposited zinc oxide films for gas sensor applications. *Appl. Surf. Sci.*, 253:7483, 2009.

[82] B. H. Kim, J. H. Jeong, Y. S. Jeon, K. O. Jeon, and K. S. Hwang. Hydroxyapatite layers prepared by solŰgel assisted electrostatic spray deposition. *Ceramics Intl.*, 33:119, 2007.

[83] L. T. de Jonge, S. C. G. Leeuwenburgh, J. J. J. P. van den Beucken, J. G. C. Wolke, and J. A. Jansen. Electrosprayed enzyme coatings as bioinspired alternatives to bioceramic coatings for orthopedic and oral implants. *Adv. Funct. Mater.*, 19:755, 2009.

[84] L. T. de Jonge, J. J. J. P. van den Beucken, S. C. G. Leeuwenburgh, A. A. J. Hamers, J. G. C. Wolke, and J. A. Jansen. In vitro responses to electrosprayed alkaline phosphatase/calcium phosphate composite coatings. *Acta Bio.*, 5:2773, 2009.

[85] J. Xie, J. C. Tan, and C. H. Wang. Biodegradable films developed by electrospray deposition for sustained drug delivery. *J. Pharm. Sci.*, 97:3109, 2008.

[86] M. Knudsen. Die gesetze der molekularströmung und der inneren reibungsströmung der gase durch röhren. *Annalen der Physik*, 333:75, 1908.

[87] M. Knudsen. Experimentelle bestimmung der druckes gesättigter quecksilberdämpfe bei 0,° C und höheren temperaturen. *Annalen der Physik*, 334:179, 1909.

[88] J N. O'Shea, J. B. Taylor, J. C. Swarbrick, G. Magnano, L. C. Mayor, and K. Schulte. Electrospray deposition of carbon nanotubes in vacuum. *Nanotechnology*, 18:035707, 2007.

[89] A. Saywell, G. Magnano, C. J. Satterley, L. M. A. Perdigao, N. R. Champness, P. H. Beton, and J N. O'Shea. Electrospray deposition of c60 on a hydrogen-bonded supramolecular network. *J. Phys. Chem.*, 112:7706, 2008.

[90] C. J. Satterley, L. M. A. Perdigao, A. Saywell, G. Magnano, A. Rienzo, L. C. Mayor, V. R. Dhanak, P. H. Beton, and J N. O'Shea. Electrospray deposition of fullerenes in ultra-high vacuum: in situ scanning tunneling microscopy and photoemission spectroscopy. *Nanotechnology*, 18:455304, 2007.

[91] A. J. Britton, A. Rienzo, K. Schulte, and J. N. O'Shea. Charge transfer between the au(111) surface and adsorbed c60: Resonant photoemission and new core-hole decay channels. *J. Chem. Phys*, 113:094705, 2010.

[92] A. Rienzo, L. C. Mayor, G. Magnano, C. J. Satterley, E. Ataman, J. Schnadt, and J. N. O'Shea. X-ray absorption and photoemission spectroscopy of zinc protoporphyrin adsorbed on rutile tio2(110) prepared by in situ electrospray deposition. *J. Chem. Phys.*, 132:084703, 2010.

[93] J. E. Lyon, A. J. Cascio, M. M. Beerborn, R. Schlaf, Y. Zhu, and S. A. Jenekhe. Photoemission study of the poly(3-hexylthiophene)/au interface. *Appl. Phys. Letts.*, 88:222109, 2006.

[94] N. Thontasen, G. Levita, N. Malinowski, Z. Deng, S. Rauschenbach, and K. Kern. Grafting crown ether alkali host-guest complexes at surfaces by electrospray ion beam deposition. *J. Phys. Chem. C*, 114:17768, 2010.

[95] L. C. Mayor, A. Saywell, G. Magnano, C. J. Satterley, J. Schnadt, and J N. OŠShea. Adsorption of a ru(ii) dye complex on the au(111) surface: Photoemission and scanning tunneling microscopy. *J. Chem. Phys.*, 130:164704, 2009.

[96] M. Weston, A. J. Britton, and J. N. O'Shea. Charge transfer dynamics of model charge transfer centres of a multi-centre water splitting dye complex on rutile tio2(110). *J. Chem. Phys*, 134:In Press, 2011.

[97] A. M. Gañàn-Calvo. Cone-jet analytical extension of taylor's electrostatic solution and the asymptotic universal scaling laws in electrospraying. *Phys. Rev. Lett.*, 79:217, 1997.

[98] H. Rensmo, S. Södergren, L. Patthey, K. Westermark, L. Vayssieres, O. Kohle, P. A. Brühwiler, A. Hagfeldt, and H. Siegbahn. The electronic structure of the cis-bis(4-4'-dicrboxy-2,2'-bipyridine) -bis(isothiocyanato) ruthenium(ii) complex and its ligand 2,2'-bipyridyl-4,4'-dicarboxylic acid studied with electron spectroscopy. *Chem. Phys. Lett.*, 274:51, 1997.

[99] H. Rensmo, K. Westermark, S. Södergren, O. Kohle, P. Persson, S. Lunell, and H. Siegbahn. Xps studies of ru-polypyridine complexes for solar cell applications. *J. Chem. Phys.*, 111:2744, 1999.

[100] E. M. J̃. Johansson, M. Hedlund, H. Siegbahn, and H. Rensmo. Electronic and molecular surface structure of ru(tcterpy)(ncs)(3) and ru(dcbpy)(2)(ncs)(2) adsorbed from solution onto nanostructured tio2: A photoelectron spectroscopy study. *J. Phys. Chem. B*, 109: 22256, 2005.

[101] R. J. Ellingson, J. B. Asbury, S. Ferrere, H. N. Ghosh, J. R. Sprague, T. Q. Lian, and A. J. Nozik. Dynamics of electron injection in nanocrystalline titanium dioxide films

sensitized with [ru(4,4 '-dicarboxy-2,2 '-bipyridine)(2)(ncs)(2)] by infrared transient absorption. *J. Phys. Chem. B.*, 102:34, 1998.

[102] P. Myllperkiö, G. Benkö, J. Korppi-Tommola, A. P. Yartsev, and V. Sundström. A study of electron transfer in ru(dcbpy)2(ncs)2 sensitized nanocrystalline tio2 and sno2 films induced by red-wing excitation. *Phys. Chem. Chem. Phys.*, 10:996, 2008.

[103] S. Wendt, R. Schaub, J. Matthiesen, E.K. Vestergaard, E. Wahlström, M.D. Rasmussen, P. Thostrup, L.M. Molina, E. Laegsgaard, I. Stensgaard, B. Hammer, and F. Besenbacher. Oxygen vacancies on tio2(110) and their interaction with h20 and o2: A combined high-resolution stm and dft study. *Surf. Sci.*, 598:226, 2005.

[104] U. Diebold. The surface science of titanium dioxide. *Surf. Sci.*, 48:53, 2003.

[105] J. Schnadt, J. N. O'Shea, L. Patthey, J. Schiessling, J. Krempaský, M. Shi, J. Schiessling, N. Mårtensson, and P. A. Brühwiler. Structural study of adsorption of isonicotinic acid and related molecules on rutile tio_2(110) ii: Xps. *Surf. Sci.*, 544:74, 2003.

[106] J. P. Perdew, K. Burke, and M. Enzerhof. Generalized gradient approximation made simple. *Phys. Rev. Lett.*, 77:3865, 1996.

[107] S. Tanuma, C. J. Powell, and D. R. Penn. Calculation of electron inelastic mean free paths (imfps) vii. reliability of the tpp-2m imfp predictive equation. *Surf. Interface Anal.*, 35:268, 2003.

[108] A. F. Carley and M. W. Roberts. An x-ray photoelectron spectroscopic study of the interaction of oxygen and nitric oxide with aluminium. *Proc. R. Soc. A.*, 363:403, 1978.

[109] J. N. O'Shea, Y. Luo, J. Schnadt, L. Patthey, H. Hillesheimer, J. Krempaský, D. Nordlund, M. Nagasono, and N. Mårtensson. Hydrogen-bond induced surface core-level shift in pyridinecarboxylic acids. *Surf. Sci.*, 486:157, 2001.

[110] J. N. O'Shea, J. Schnadt, P. A. Brühwiler, and H. Hillesheimer N. Mårtensson. Hydrogen-bond induced surface core-level shift in isonicotinic acid. *J. Phys. Chem. B*, 105:1917, 2001.

[111] J. N. O'Shea, J. C. Swarbrick, K. Nilson, C. Puglia, B. Brena, Y. Luo, and V. Dhanak. Molecular ordering in isonicotinic acid on rutile tio2(110) investigated with valence band photoemission. *J. Chem. Phys.*, 121:10203, 2004.

[112] J. C. Fuggle and N. Mårtensson. Core-level binding energies in metals. *J. Elec. Spec. Rel. Phen.*, 21:275, 1980.

[113] J. B. Taylor, L. C. Mayor, J. C. Swarbrick, J. N. O'Shea, C. Isvoranu, and J. Schnadt. Adsorption and charge transfer dynamics of bi-isonicotinic acid on au(111). *J. Chem. Phys.*, 127:134707, 2007.

[114] J. B. Taylor, L. C. Mayor, J. C. Swarbrick, J. N. O'Shea, and J. Schnadt. Charge-transfer dynamics at model metal-organic solar cell surfaces. *J. Phys. Chem. C*, 111:16646, 2007.

[115] J. Schnadt, P. A. Brühwiler, L. Patthey, J. N. O'Shea, S. Södergren, M. Odelius, R. Ahuja, O. Karis, M. Bässler, P. Persson, H. Siegbahn, S. Lunell, and N. Mårtensson. Experimental evidence for sub-3-fs charge transfer from an aromatic adsorbate to a semiconductor. *Nature*, 418:620, 2002.

[116] J. Schnadt, J. N. O'Shea, L. Patthey, L. Kjeldgaard, J. Åhlund, K. Nilson, J. Schiessling, J. Krempaský, M. Shi, O. Karis, C. Glover, H. Siegbahn, N. Mårtensson, and P. A. Brühwiler. Excited-state charge transfer dynamics in systems of aromatic adsorbates on tio_2 studied with resonant core techniques. *J. Chem. Phys.*, 119:12462, 2003.

[117] P. Persson, S. Lunell, P. A. Brühwiler, J. Schnadt, S. Södergren, J. N. O'Shea, O. Karis, H. Siegbahn, N. Mårtensson, M. Bässler, and L. Patthey. N1s x-ray absorption study of the bonding interaction of bi-isonicotinic acid adsorbed on rutile tio2(110). *J. Chem. Phys.*, 112:3945, 2000.

[118] J N. O'Shea, J. B. Taylor, L. C. Mayor, J. C. Swarbrick, and J. Schnadt. Molecular damage in bi-isonicotinic acid adsorbed on rutile tio2(110). *Surf. Sci.*, 602:1693, 2008.

[119] B. Kempgens, A. Kivimaki, M. Neeb, H. M. Koppe, A. M. Bradshaw, and J. Feldhaus. A high-resolution n 1s photoionization study of the n-2 molecule in the near-threshold region. *J. Phys. B.*, 29:5389, 1996.

[120] M. Coville and T. D. Thomas. Molecular effects on inner-shell lifetimes: Possible test of the one-center model of auger decay. *Phys. Rev. A*, 43:6053, 1991.

[121] J. B. Asbury, R. J. Ellingson, H. N. Ghosh, S. Ferrere, A. J. Nozik, and T. Q. Lian. Femtosecond ir study of excited-state relaxation and electron-injection dynamics of ru(dbbpy)2(ncs)2 in solution and on nanocrystalline tio2 and al2o3 thin films. *J. Phys. Chem. B.*, 103:3110, 1999.

[122] P. Persson and M. J. Lundqvist. Calculated structural and electronic interactions of the ruthenium dye n3 with a titanium dioxide nanocrystal. *J. Phys. Chem. B.*, 109:11918, 2005.

[123] J. A. D. Matthew and Y. Komninos. Transition rates for interatomic auger processes. *Surf. Sci.*, 53:716, 1975.

[124] M. Grätzel and A. Hagfeldt. Molecular photovoltaics. *Acc. Chem. Res.*, 33:269, 2000.

[125] J. D. Hall, T. M. McLean, S. J. Smalley, M. R. Waterland, and S. G. Telfer. Chromophoric dipyrrin complexes capable of binding to tio2: Synthesis, structure and spectroscopy. *Dalt. Trans.*, 39:437, 2009.

[126] S. J. Smalley, M. R. Waterland, and S. J. Telfor. Heteroleptic dipyrrin/bipyridine complexes of ruthenium (ii). *Inor. Chem.*, 48:13, 2008.

[127] K. Westermark, H. Rensmo, J. Schnadt, P. Persson, S. Södergren, P. A. Brühwiler, S. Lunell, and H. Siegbahn. Electron dynamics within ru-2,2 '-bipyridine complexes - an n1s core level excitation study. *Chem. Phys.*, 285:167, 2002.

[128] A. Föhlisch, P. Feulner, F. Hennies, A. Fink, D. Menzel, D. Sanchez-Portal, P. M. Echenique, and W. Wurth. Direct observation of electron dynamics in the attosecond domain. *Nature*, 436:373, 2005.

[129] M. Grätzel. Applied physics: Solar cells to dye for. *Nature*, 421:586, 2003.